ABSTRACT

Title of Thesis: PRESSURELESS SINTERING OF POWDER PROCESSED GRADED METAL-CERAMIC COMPOSITES USING A NANOPARTICLE SINTERING AID AND BULK MOLDING TECHNOLOGY

Jonathan G. Kruft Jr.
Master of Science, 2007

Directed By: Associate Professor Hugh Bruck
Department of Mechanical Engineering

The need exists to fabricate graded metal-ceramic composites in bulk manufacturing processes for commercial applications. To address this need, a three-fold approach is employed: (1) control of the evolution of shrinkage strain and mechanical properties through the use of a nanoparticle sintering aid, (2) modeling of shrinkage-induced stresses to determine gradient architectures where cracking does not occur, and (3) fabrication of graded metal-ceramic composites using pressureless sintering and bulk molding technology. A new nanopowder TiO_2 sintering aid was introduced to control the evolution of shrinkage and mechanical properties of graded Nickel-Alumina composites. The evolution of shrinkage strain and mechanical properties were then used in a recently developed two-dimensional microthermomechanical finite element analysis to determine the effects on shrinkage-induced stresses and develop gradient

architectures where cracking would not occur. Finally, a laboratory-scale processing system based on a commercial bulk molding technology was developed to bulk process geometrically-complex gradient structures.

PRESSURELESS SINTERING OF POWDER PROCESSED GRADED METAL-CERAMIC COMPOSITES USING A NANOPARTICLE SINTERING AID AND BULK MOLDING TECHNOLOGY

By

Jonathan G. Kruft Jr.

Thesis submitted to the Faculty of the Graduate School of the
University of Maryland, College Park, in partial fulfillment
of the requirements for the degree of
Master of Science
2007

Advisory Committee:
Associate Professor Hugh Bruck, Chair
Associate Professor Satyandra Gupta
Associate Professor F. Patrick McCluskey

Acknowledgements

First, I would like to thank my advisor, Dr. Hugh Bruck, for his support and guidance throughout my education and research. He has been instrumental in my professional growth in the time I have known him.

I would also like to thank the members of my committee, Dr. Satyandra Gupta and Dr. Patrick McCluskey, for their assistance in my education and taking the time to take part in my thesis defense.

I also owe special thanks to Dr. Yasser Shabana, whose input, advice, and hard work has been invaluable. I also would like to thank my current and former lab-mates Mike Pines, Dan Cole, Arun Kota, Alan Gershon, J.R. Gyger, and Brent Spraklin for their willing assistance whenever I needed it. Finally, I would like to thank Melanie Patrick and Shea Brown for their help in the compilation of this thesis.

I owe a lot to those previously mentioned and all others that have helped me reach this point in my education. Without their support, I would have been unable to complete this work.

Table of Contents

List of Tables

List of Figures

CHAPTER 1: Introduction

1.1 Background

Multifunctional multimaterial structures combine material properties to meet multiple functional requirements. These materials are often layered on top of one another and bonded with adhesive. However, this sharp division of materials at the bonding location generates a weak interface that results in stress concentration. For example, an impact-generated stress wave that propagates through the sharp interface creates a tensile force as the wave transmits across and reflects off the interface [1]. The resultant stress can lead to debonding of the joined materials at the weak interface.

One solution is to transition the interface through a material gradient. Functionally graded materials (FGM) spatially vary composite microstructure or composition to optimize resultant material properties. The microstructural distribution of phases within a two-phase material can be identified by three basic types of morphologies: (1) dispersed, (2) aggregated, and (3) percolated [2]. As seen in Figure 1a, a dispersed grain structure occurs when the volume fraction of one phase is low and is discretely and randomly distributed within the dominate matrix phase. As volume fraction of the minor inclusion phase increases, particle agglomerates begin to form an aggregated structure (Figure 1b). With even further increasing volume fraction, the minor phase will reach a critical point called the percolation threshold. At this point, long-range interconnectivity begins to occur between particle agglomerates (Figure 1c).

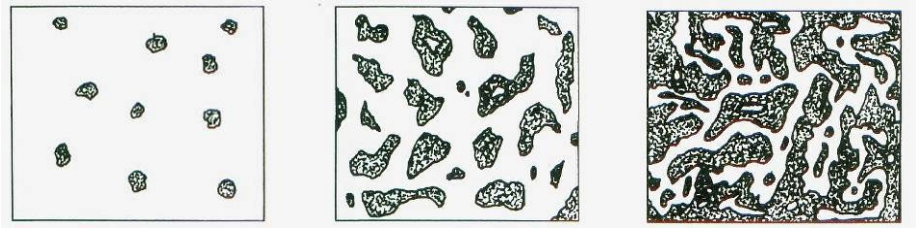

(a) (b) (c)

Figure 1: Basic types of heterogeneous two-phase microstructures: (a) dispersed grain structure, (b) aggregated grain structure, and (c) percolated cluster structure [2].

Compositional gradients take advantage of multiple material properties and avoid the stress-strain concentrations that occur at sharp interfaces of different materials. Dependent on the microstructure, material properties vary with position within the gradient and can be used to tailor composite performance and functionality. For example, a functionally graded plate may be used in applications of high temperature and stress, where a thermal resistant material on the exposed outer surface is graded with an inner material that exhibits better mechanical strength. A two-phase graded structure is shown in Figure 2, consisting of two pure base materials at the ends and a gradient microstructure in between. The gradient can be represented through homogenization as a linearly varying composition, V(x), from x equal 0 to L.

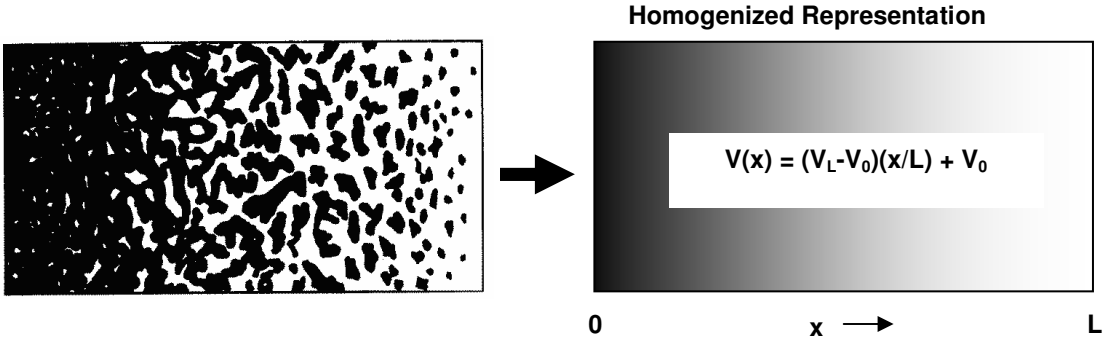

Figure 2: Two-component graded structure, for which the microstructure varies linearly from one pure component to the other [2].

Natural structures, such as bamboo and bone, also exhibit graded material distributions that optimize performance through spatial variations in functionality. Bamboo utilizes a hierarchical microscopic gradient structure of bundle sheath fiber reinforcement to provide radial strength in response to bending loads [3]. Considered a multifunctional material structure, bamboo is capable of providing the mechanical support for the entire natural structure while concurrently delivering nutrients from the roots. Another example is natural bone, primarily made of collagen and calcium phosphate, which is relatively hard. A gradient of pores within the bone is naturally tailored to allow for reduction in mass, increase in ductility, and permission of fluid flow.

The fabrication of functionally graded materials is most often hindered by the variation of elastic, plastic, thermal, chemical, and kinetic properties within the composite. Across a material interface, these discontinuities in material properties lead to the formation of residual stresses [4]. Despite these challenges, compositional gradient structures offer significant benefits. In addition to utilizing the beneficial properties of the pure base materials, the transition of thermal stresses across materials with vast thermal expansion mismatch can be smoothed, the magnitude and critical locations of thermal and mechanical stresses can be tailored with geometry, the onset of plastic yielding and failure can be delayed, and stress concentrations at free edges can be minimized [5,6].

This section will introduce the challenges and methods for fabricating functionally graded metal-ceramic structures. This section will also discuss new

techniques for reducing fabrication costs and increasing fabrication production through bulk processing techniques.

1.1.1 Functionally Graded Metal-Ceramics

The properties of monolithic ceramics or metals depend strongly on their bonding characteristics, such as bonding length and bending strength [7]. Ceramics typically exhibit high hardness, low density and weight, brittleness, and excellent high-temperature fracture, creep, corrosion, radiation, wear, and thermal shock resistance. On the other hand, metals are typically ductile, have high tensile strength, high toughness, and high density.

Many structures exist where desired performance varies with location within the structure. Multifunctional metal-ceramic structures are well suited for applications where both toughness and hardness are required. For example, knives and other cutting tools must be hard on the cutting edge. However, strength and toughness are desired elsewhere. Another example is a gear, which exhibits different requirements for the teeth and body. The teeth of the gear must be hard and wear resistant to surface contact forces, whereas the gear body must be tough to withstand fracture [5]. Similarly, armor applications require a hard outer surface and tough inner surface, as seen in Figure 3. Upon projectile impact, the hard outer surface serves to blunt and to induce a destructive shock wave on the projectile. The tough inner surface absorbs the residual kinetic energy from the projectile remains [8]. However, conventionally bonded metal-ceramic plates exhibit a weak interface that affects stress wave propagation. Thus, a compositional gradient that eliminates the sharp interface between materials is ideal for an armor package or any other energy-

absorbing application. In addition, the graded interface can be optimized to meet desired ballistic performance. The compositional gradient has been shown to introduce a beneficial time delay to the reflection of peak stress wave propagation [9]. By delaying the time to initiate damage in the structure, the FGM has greater dynamic energy absorbing capacity than a non-graded bonded structure.

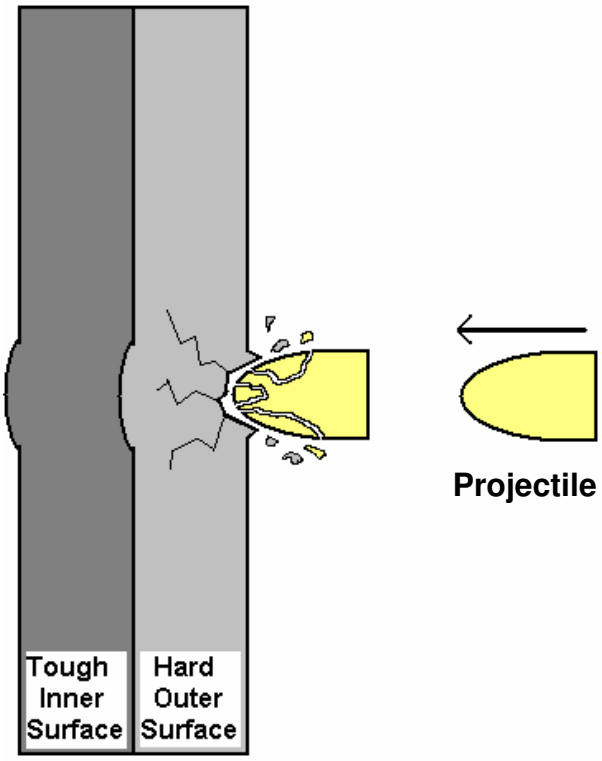

Figure 3: Ceramic-metal armor plating.

Another military application is the development of graded metal-ceramic gun barrels [10]. A ceramic inner barrel liner with a metal-based jacket allows for the use of higher energy propellants to deliver more energy to the target or operate at longer engagement distances. Metal-ceramic FGMs can also be designed to take advantage of the heat and corrosion resistance of ceramics and the mechanical strength of metals in such applications as thermal or chemical barriers [11].

The introduction of a material gradient to replace a sharp interface presents new fabrication challenges. The graded interface can be considered a continuous variation in composite microstructure from one material phase to another. In order to simplify fabrication, this continuous transition in microstructure is often approximated by discrete layers of distinct composite compositions, as seen in Figure 4. Properties of these composite compositions are often modeled by rule-of-mixtures (ROM) or modified ROM formulations [2,6,12]. However, the introduction of the material gradient to replace the sharp interface does not eliminate the formation of stresses due to the mismatch of material properties. In fact, for certain geometries, the use of an arbitrary gradient may result in higher local stress concentrations than in a non-graded joint [13]. As a result, gradients must be carefully tailored to reduce the formation of these stresses, as described in the following section. There are multiple ways to tailor the graded microstructure, a popular one being a power law formula using an exponent, p, to control the variation in volume fraction, f, as a function of the distance, x, along the graded interface normalized by its thickness, t.

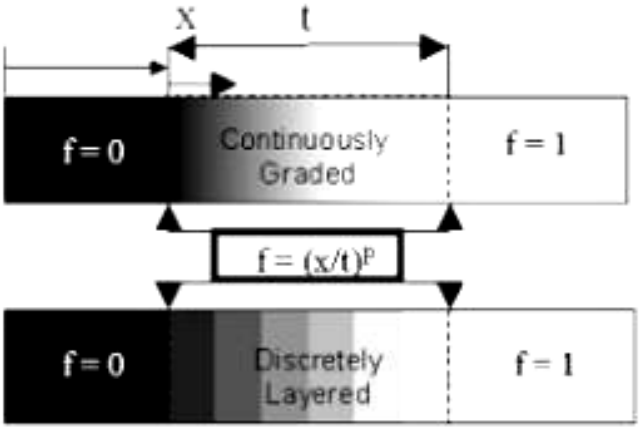

Figure 4: Continuously graded structure and corresponding approximation using discrete layers.

1.1.2 Residual Stresses

Thermal and mechanical loading on a multimaterial structure generates residual interfacial stresses due to the discontinuity in material properties at the interface. The most common failure mode observed in bonded metal-ceramic structural components occurs as tensile edge stresses within the ceramic promote crack propagation parallel and adjacent to the interface [4]. The origin of stresses caused by thermal loading for a bonded metal-ceramic is shown in Figure 5.

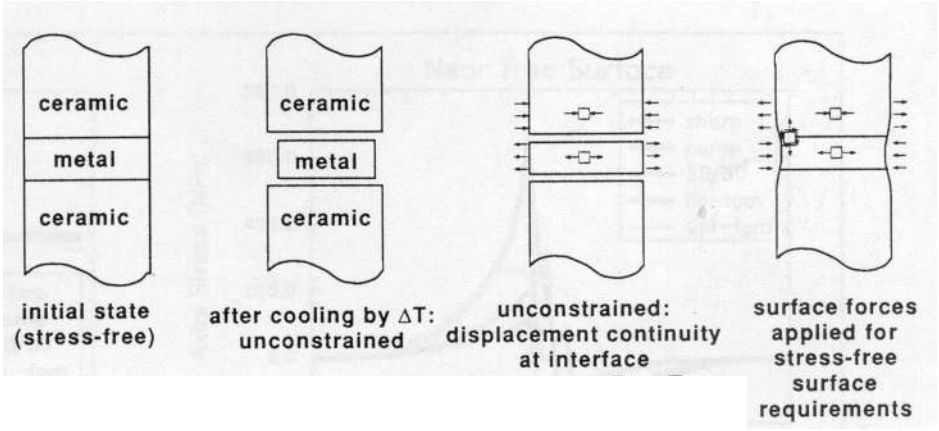

Figure 5: Initial and final states of a bonded metal-ceramic composite when introduced to thermal loading [4].

Removing the sharp interface by the use of an interlayer compositional gradient between the pure base materials is clearly beneficial. However, residual stresses still develop at the new heterogeneous interfaces introduced by the composite compositional gradient. The thermal response and stress generation within the gradient during FGM processing has received significant attention recently [2]. The consolidation process typically introduces significant thermal loads on the FGM structure, particularly during cooling from the processing temperature [14]. The response to thermal loads of each microstructural composition in the structure is unique. As a result, stresses develop in the structure as the gradient consolidates and

cools at different rates. These residual stresses can eventually lead to cracking or debonding of the FGM structure during fabrication. In conclusion, compositional gradients can in fact be used to reduce metal-ceramic interfacial stresses, but the success of this approach requires knowledge of failure mechanisms and microstructural effects to tailor the gradient as required [13].

1.1.3 Fabrication of Functionally Graded Metal-Ceramics

This section will document popular fabrication methods of functionally graded metal-ceramic structures. The creation of compositional gradients has been demonstrated by many fabrication methods. In particular, this research will focus on powder processing techniques and the appropriate consolidation methods.

A number of models exist for the design of the spatial variation of the gradient composition [2]. One popular gradient function is the aforementioned power law distribution, such as Equation (1) used by Drake *et al.* [15]. For this equation, the two constituent phases are defined as materials 0 and 1 where f_0 is the local volume fraction of phase 0, x is the distance from the phase 1 interface, t is the thickness of the gradient region, and p is an arbitrary exponent that controls the curvature of the gradient distribution.

$$f_0 = \left(\frac{x}{t}\right)^p \tag{1}$$

As seen in Figure 6, the curvature of the gradient distribution can be made concave upward or downward by selection of p.

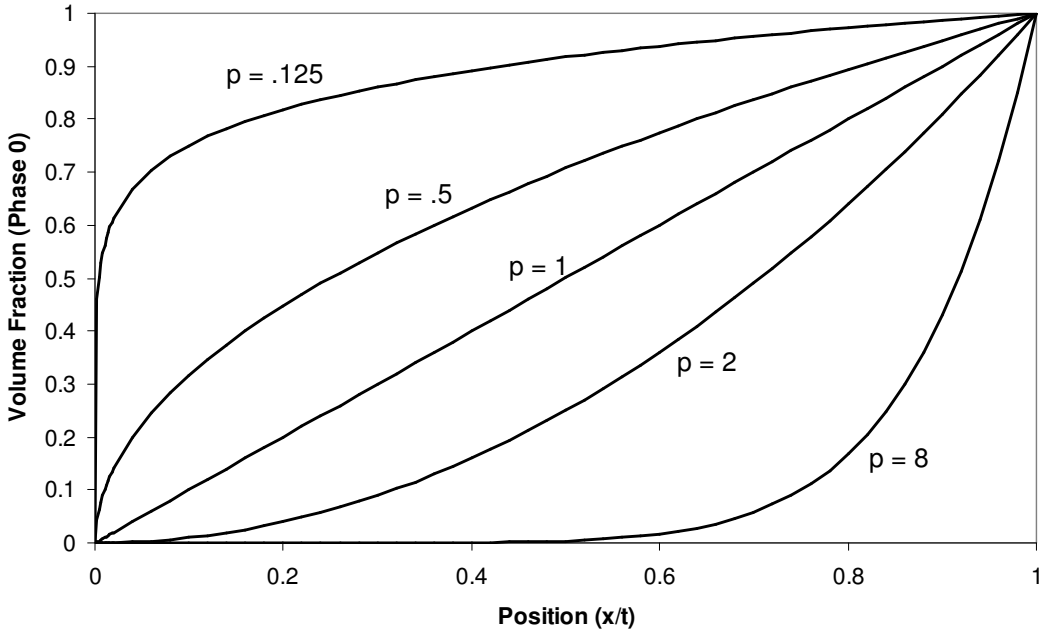

Figure 6: Compositional gradients based on the power law for several values of *p*.

Using the power law distribution, gradients can be tailored to be more sensitive to either base material using either a concave up or concave down function. Additionally, a simple linear distribution can still be achieved by using an exponent of one. Drake *et al.* used the power law distribution to show that significant stress and plastic strain reductions can be achieved by increasing gradient thickness and tailoring the exponent to provide gradual compositional change near phases that exhibit high modulus and little plasticity, such as ceramic materials [15].

Powder Processing

The fluidlike behavior of powdered materials allows for a variety of green (i.e., unconsolidated state) shaping processes, such as die compaction. In addition, there is a great deal of microstructural and compositional control when working with powder constituents. Conventional powder processing produces a green body of powder with the desired gradient of phase volume fractions. This research will focus

on constructive fabrication processes rather than natural transport phenomena processes. These constructive processes vary from simple step-wise layering methods to highly automated continuous distribution operations [5]. The discrete layering method forms the green body by sequentially adding pre-mixed powder compositions to a compaction die. Alternatively, continuous distribution methods attempt to eliminate compositional interfaces all together by gradually increasing phase content in some functional distribution. This is typically accomplished by a highly-controlled spray process. Layering techniques offer the ability to build up the graded region incrementally without the need for sophisticated equipment to continuously monitor the microstructure, which is a critical requirement in continuous grading operations [1]. Accordingly, the discrete layering method is well suited for operations focused on the inexpensive bulk manufacturing of graded products.

Following gradient fabrication, the green body must then be subjected to a solid-state densification process. Densification of FGMs has been achieved by cold pressing and pressureless sintering, by Hot Isostatic Pressing (HIP), or by hot pressing in a closed die [5]. A powder processing fabrication flow chart, based on previous research [14], for gradient structures is shown in Figure 7.

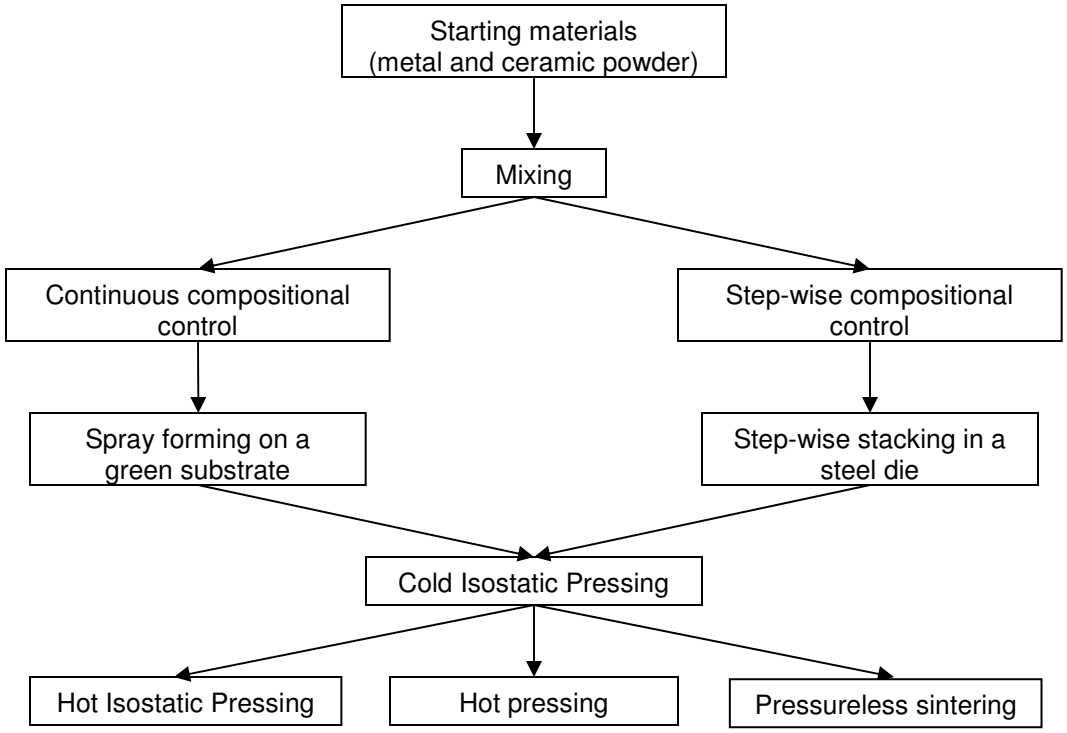

Figure 7: Flow chart for the fabrication of functionally graded materials using powder processing.

Pressureless Sintering

Sintering is defined as a thermal treatment for bonding particles into a coherent, predominantly solid structure via mass transport events on the atomic scale [16]. When no external pressure is applied, the process is known as pressureless sintering. Pressureless sintering is an inexpensive consolidation method that can produce a wide range of sintered geometries. However, without external pressure there is no restriction on the deformation of the specimen during sintering, which can lead to severe differences in differential shrinkage. Despite this challenge, pressureless sintering in a high temperature furnace provides a simple consolidation method well suited for the bulk manufacturing of graded products.

Sinter bonding tends to be temperature sensitive. As the sintering temperature is increased, sintering kinetics generally accelerate. Particle cohesion increases as the porous interfaces between particles are consumed at increasing temperature. As sintering proceeds, grain growth begins to occur until some maximum is reached and the sintering process is complete. Particle size also has a significant role in sintering kinetics. Previous work has demonstrated that high-energy discus milling of Aluminum-TiO_2 powder to produce $Ti_2O(Al)/Al_2O_3$ composites reduces particle size, which in turn accelerates the densification process and increases the hardness of the pressureless sintered composites [17].

The dominate matrix phase typically controls densification at low volume fractions of the inclusion phase. As volume fraction of the inclusion phase increases, the inclusions can begin to resist composite densification and cause discrepancies in the sintering rate. In particular, metals densify much faster than ceramics. As a result, the densification of FGMs typically exhibit uneven shrinkage between composition layers. This differential shrinkage in a FGM structure can lead to the formation of the residual sintering stresses discussed previously.

Sintering kinetics can be modified to match the sintering rate of the two powder phases. Particle size control can be used to control sintering rate by modifying specific surface energy in an attempt to adjust the free-energy gradient [14,18]. Alternatively, small quantities of sintering aids can be added to the ceramic phase to increase the densification rate and the lower sintering temperature [19-21]. By modifying the sintering kinetics and matching the sintering rates of the two

phases, FGM warping and cracking during fabrication can be significantly reduced or fully eliminated.

Sintering Aids

The sintering of Alumina (Al_2O_3), an important material in the field of engineering oxide ceramics, usually takes place at high temperatures between 1550-1600˚C [19]. However, the sintering of metal-ceramic composites is typically limited by the relatively low melting point of the metal. In the case of Nickel-Alumina composite structures, this sintering temperature is limited to 1350-1400˚C. The ceramics industry has long used small amounts of sintering additives, such as TiO_2, MgO, SiO_2, MnO_2, Cr_2O_3, or Fe_2O_3, to influence the ceramic densification process by reducing sintering temperature and increasing grain growth [19]. In particular, the hardness of Alumina composites depends mainly on the microstructural grain size and the final density of the sintered samples [22].

Sintering aids are often applied to ceramics using a doping procedure. Doping processes typically require mixing with dissolved chlorides followed by hydrolization with ammonium hydroxide [23]. These are often complicated and time consuming operations. In this research, the blending of sintering aids through the use of powder ball-mixing will be explored as an alternative.

Previous work using Alumina has found TiO_2 more effective than MnO_2 as a sintering aid at lower sintering temperatures [20]. In this same study, Alumina was sintered to 95% theoretical density at 1350˚C using 3 wt.% TiO_2. Conversely, the pure Alumina sample without sintering additive only reached 77.1% theoretical density at the same temperature. In another study, TiO_2 was added to a 10 wt.%

Nickel-Alumina powder composite [21]. Using 5 wt.% TiO_2, the Nickel-Alumina composite reached 97% theoretical density after pressureless sintering at 1480˚C. The sintered sample without the TiO_2 additive only reached 60% theoretical density.

Thermal-Behavior Matching Process

A spatial variation in porosity is created when loose powders are compacted. Combined with composition surface tension and atomic mobility, the sintering behavior of each powder composition has a unique sintering start temperature, sintering rate, and volumetric shrinkage [18]. Differences in sintering behavior that cause differential shrinkage within the gradient result in the formation of residual stresses that can lead to fracture or debonding at layer interfaces. These residual sintering stresses must be minimized in order to consolidate crack-free FGM structures.

A thermal-behavior matching process attempts to adjust the free-energy gradient to modify sintering behavior. This is influenced by the initial pore fraction and particle size distribution of each phase in each layer. Winter *et al*. has developed a thermal-behavior matching process for Nickel-Alumina composites by setting an appropriate relative green densification target and adjusting sintering rates by utilizing particle-size distributions and binder additives [18]. This processing strategy using discrete layers of Nickel-Alumina composite compositions is described below.

The relative green density of powder layers can be matched using particle-size adjustments or the addition of a binder that can be removed before sintering. This technique eliminates the substantial variation in initial density due to the unique pore fraction in each layer. As seen in Figure 8, the relative green density was well

matched using binder additives, particle-size adjustment, and a compaction pressure of 88 MPa [18].

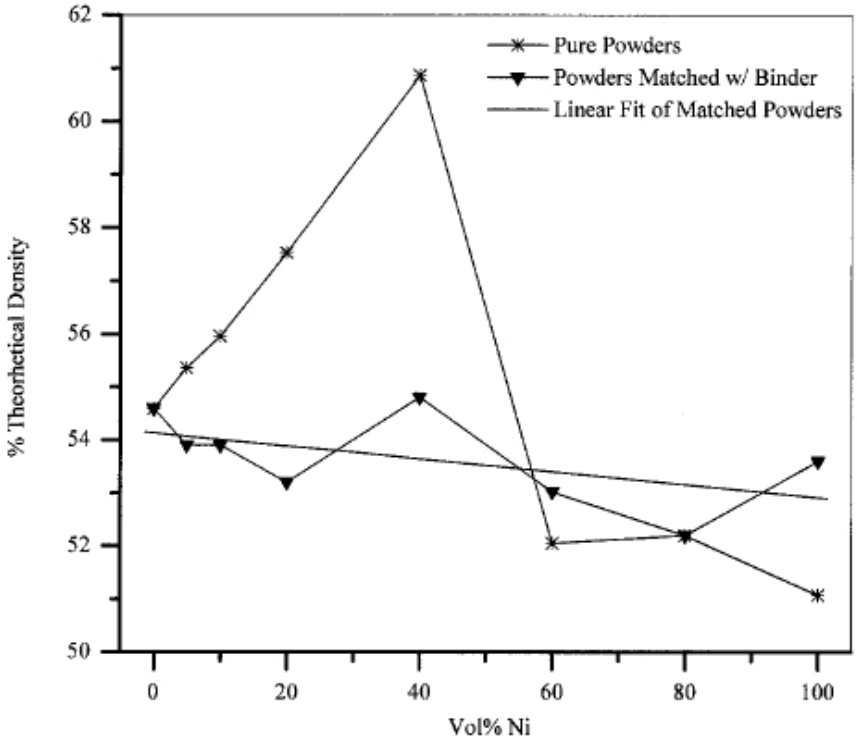

Figure 8: Effect of binder and particle-size adjustment on the relative green density of Nickel-Alumina composites [18].

Bimodal particle distributions can be used to reduce total volumetric shrinkage, slow the sintering rate, and increase the sintering start temperature. This is especially appropriate for the pure Nickel layer, which shrinks sooner, faster, and more completely than any other composite layer. Below 40 vol.% Nickel, sintering is dominated by the low surface energy of Alumina and the Nickel phase behaves similar to porosity in the Alumina matrix. The 40 and 60 vol.% Nickel layers behave similar to very porous compacts where pore removal becomes very difficult. These two layers exhibit a substantial decrease in sintering rate and total volumetric

shrinkage. Above 70 vol.% Nickel, the Nickel matrix dominates densification and substantial volumetric shrinkage is observed.

Thermal-matching can be used to modify sintering start temperature, sintering rate, and volumetric shrinkage to minimize differential shrinkage. As seen in Figure 9, a successful study has utilized particle size control to match the sintering behaviors of SUS304-PSZ composite powders [14]. Minimizing this differential shrinkage will reduce residual stresses that can cause premature cracking or debonding during the sintering process.

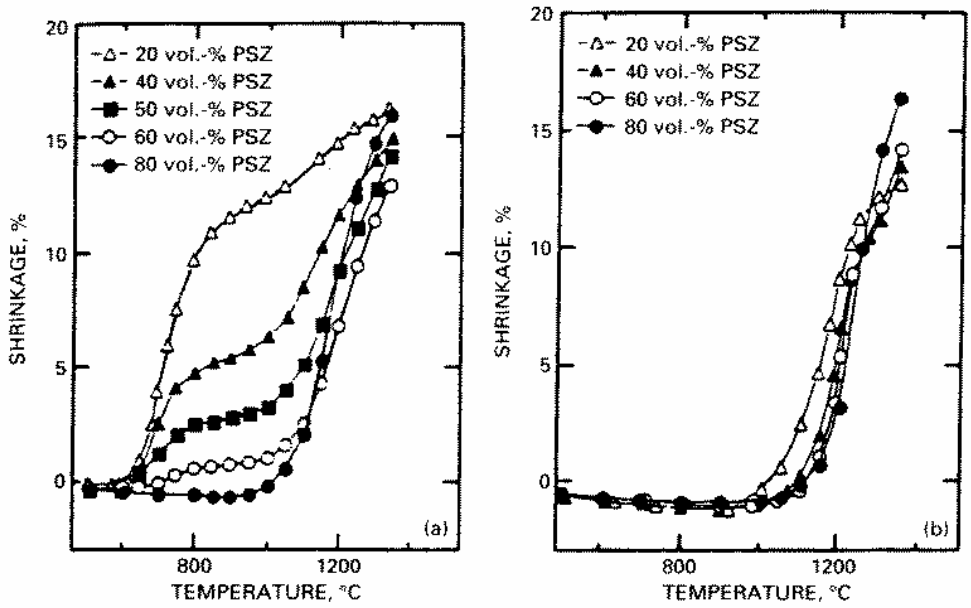

Figure 9: SUS304-PSZ composite shrinkage before (left) and after (right) sintering behavior adjustment by particle size control [14].

1.1.4 Bulk Molding Strategies

Popular bulk processing techniques utilized by commercial powder metallurgy and concrete industries can be adapted to the fabrication of powder processed gradient structures. Combined with the processing techniques presented in the preceding sections, bulk operations can be accomplished by featuring large-scale

powder mills and furnaces. Instead of using individual compaction dies, specimens can be fabricated within large molds, often consisting of tens to hundreds of individual mold cavities. Using step-wise discrete layering methods and pressureless sintering, large numbers of graded products could ultimately be produced quickly, cheaply, and reliably.

1.2 Research Objectives

The objective of this research is to advance the understanding of graded metal-ceramic composite fabrication to enable the commercial bulk processing of products from graded metal-ceramic composites. To meet this challenge, conventional powder processing and pressureless sintering techniques have been employed using nanopowder TiO_2 as a new sintering aid to control the evolution of shrinkage strains and mechanical properties within gradient structures. A systematic effort was undertaken to produce large numbers of composite specimens from Nickel and Alumina powders. These composite specimens were produced over a wide range of phase volume fractions in both homogeneous form to quantify sintering behavior, and as graded structures to investigate cracking from shrinkage-induced stresses during the sintering process. These shrinkage-induced residual stresses developed during the sintering process can be predicted using a recently developed two-dimensional microthermomechanical finite element model. To develop the basis for the bulk processing of graded metal-ceramic products, a prototype commercial bulk molding technology had to be developed and instrumented in order to study the effects of processing conditions on more geometrically-complex gradient structures.

This section outlines the scope of the research and fundamental contributions made to the metal-ceramic scientific community.

1.2.1 Research Goals

First, this research will explore the effects of a nanopowder sintering additive applied to functionally graded specimens. Emphasis will be placed on a simple powder blending method and complicated doping procedures will be avoided. Sintering behavior, microstructural changes, and characteristic properties will be documented. Monitoring the sintering behavior of distinct composite compositions will enable the development of a finite element model to predict the effects of the nanoparticle sintering aid on the evolution of shrinkage strains and mechanical properties in each composition. As a result, this model will predict cracking from shrinkage-induced stresses when the composite compositions are employed in a discrete layered gradient structure. Secondly, commercial bulk processing methods will be investigated. To produce geometrically-complex graded metal-ceramic specimens, the goal is to develop a laboratory-scale bulk molding assembly similar to technology developed for the concrete products industry.

The main focus of this research is to advance bulk metal-ceramic FGM production by developing technologies and procedures to reduce fabrication time, complexity, and cost. For this reason, conventional powder processing and pressureless sintering will be employed. Fully consolidated, crack-free FGMs are desired without resorting to complex procedures, such as chemical doping or Hot Isostatic Pressing.

1.2.2 Scope of Research

This research investigates the fabrication of graded metal-ceramic composites using pressureless sintering with a new nanoparticle sintering aid and commercial bulk molding technology. Chapter 2 focuses on the processing procedures and results of using a nanopowder TiO_2 sintering aid for Nickel-Alumina composites. The basic powder processing fabrication techniques applied were outlined in previous research [23]. The use of nanopowder TiO_2 as a sintering aid for graded composite structures had not previously been investigated. Therefore, it was necessary to quantify the nanoparticle effects on the evolution of shrinkage strains and mechanical properties in order to predict shrinkage-induced stresses in gradient architectures.

For the evolution of shrinkage strains, a previously developed porosity reduction calculation is presented in Chapter 2 that quantifies the evolution of porosity consumption during the sintering process. These calculations are important in understanding and overcoming the differential shrinkage problems encountered using intermediate gradient compositions that were not discretely quantified as well as thermal profiles that deviate from those employed in this investigation. No prior research effort has studied the evolution of porosity reduction when nanoparticle sintering aids are employed.

The modeling of shrinkage-induced stresses in gradient architectures is described in Chapter 3 using a two-dimensional microthermomechanical finite element analysis (FEA). The focus of the modeling is to understand the effects of the nanoparticle TiO_2 sintering aid on the graded Nickel-Alumina composites. A description of the model is given and the assumptions included in the model are discussed. Ultimately, the FEA model provides the ability to predict the stresses that

are produced during sintering for the desired geometry and gradient architecture. This model allows for the development of viable gradient regions that minimize required layer thickness prior to the fabrication of the actual composite.

The fabrication of model graded metal-ceramic cylinders is also discussed in Chapter 3. These model graded cylinders can be qualitatively examined for cracking and the axial variation of the diameter, or the deformed profile, of the specimen quantified in order to compare directly with the FEA predictions. Furthermore, the local mechanical properties of the graded metal-ceramic composite were quantified using microhardness testing and compared with stress-free homogeneous composite specimens to understand the effects of the evolution of local shrinkage-induced residual stresses on the global sintered composite.

In Chapter 4, the focus of the work shifts to the development of commercial bulk molding technology to fabricate geometrically-complex graded plate specimens. In this chapter, the construction of a laboratory-scale processing system based on commercial concrete molding technology is described. A prototype mold was instrumented with strain gages in order to investigate the dynamic response of the mold under different processing conditions. A fast Fourier transform (FFT) is used to quantify critical characteristics of the modal response and the effect of modifying the mold with new nanofiber-reinforced polymers. An initial investigation into the bulk processing of graded metal-ceramic composites was then initiated using a variety of gradient architectures that were qualitatively characterized for cracking. A few processed specimens were then chosen for more rigorous microstructural and microhardness characterization.

1.2.3 Scientific and Technical Contributions

The ceramics community has long established that certain sintering aids, such as TiO_2, can be used to lower sintering temperature and increase densification of fired monolithic ceramics. This research applies nanopowder TiO_2 to functionally graded metal-ceramic structures for the first time. Nanopowder TiO_2 is added using conventional powder mixing and no doping procedure is used. For the first time, the evolution of shrinkage strains and mechanical properties due to the addition of a nanoparticle sintering aid in metal-ceramic composites has been quantified. Additionally, previously developed porosity reduction models have been employed for the prediction of the nanoparticle sintering aid effects on the composites and corresponding shrinkage curves.

The fabrication of crack-free graded cylinders that demonstrate higher hardness and less porosity has also been achieved with the nanoparticle sintering aid. Increasing the hardness of the FGM structure is extremely beneficial to many applications. For example, for most armor packages the hardest outer material possible will provide the best level of ballistic protection [8]. Using the porosity reduction models for predicting the evolution of shrinkage strains and mechanical properties, it was possible for the first time to predict shrinkage-induced stresses when using a nanoparticle sintering aid with a previously developed two-dimensional microthermomechanical finite element analysis and to experimentally verify the model using the deformed profile of the graded cylinders.

This research also investigates for the first time the bulk processing of geometrically-complex graded metal-ceramic plates based on commercial molding technology used in the concrete products industry. A laboratory-scale processing

system has been developed using a prototype mold to fabricate modular hexagonal gradient structures. The successful fabrication of these hexagonal specimens demonstrates the ability to cheaply and effectively mass produce modular metal-ceramic FGMs.

In summary, this research advances the understanding of the processing of graded metal-ceramic composites, a field that has often been limited to expensive and complex manufacturing techniques. The contributions made by this research will open new pathways to the ultimate goal of the commercial bulk processing of products using graded metal-ceramic composites.

CHAPTER 2: Fabrication and Characterization of Metal-Ceramic Composites Including a Nanoparticle Sintering Aid

2.1 Introduction

Traditional powder processing and pressureless sintering techniques have been applied to metal-ceramic gradient structures that include a nanoparticle sintering aid. Steel dies are used to fabricate discrete layered Nickel-Alumina composite gradient structures. This section will describe the fabrication processes and property characterization of the resultant composites. Previously developed porosity and sintering models will also be adapted to characterize the sintering behavior of these composites. Ultimately, characterization of the effects of the nanoparticle sintering aid will allow the development of a model to predict the evolution of stresses in gradient structures containing the sintering aid in Chapter 3.

2.2 Material Selection

The fabrication of functionally graded materials requires careful matching of constituents, in this case metal and ceramic powders. The firing treatment applied to the powders must be kept below the absolute melting points of the materials. As such, melting temperature acts as the limiting factor in the solid-state sintering process. The material with the lower melting temperature limits the achievable maximum sintering temperature for the entire composite. Sintering temperature relative to the melting point of the material is critical to the amount of sinter bonding that occurs. Consequently, the material with the higher melting temperature does not reach the same extent of sinter bonding as the material with the lower melting temperature [13].

Due to the relatively low melting point of most metals, the choice of appropriate ceramic systems is limited. However, a popular metal-ceramic system frequently used to create FGM structures is Nickel-Alumina [1,4,12,13,15,18,21,23-28]. Properties of Nickel and Alumina are presented in Table 1.

Table 1: Standard properties of Alumina and Nickel [16].

Property	Alumina	Nickel
Composition	Al_2O_3	Ni
Density (g/cm^3)	3.96	8.9
Crystal Type	Hexagonal	FCC
Melting Temperature (˚C)	2054	1453
Elastic Modulus (GPa)	405	214
Poisson's Ratio	.26	.31
Yield Strength (MPa)	300	130
Fracture Toughness (MPa√m)	2	–
Hardness (HV)	1500	40

2.2.1 Particle Size

In order to tailor composite microstructure, discrete particle reinforcement is desired. By controlling the particle sizes and size ratio between the matrix and inclusion phases, it is possible to obtain adequate sinter bonding in the ceramic-rich compositions and acceptable mechanical properties in the metal-rich compositions [13]. A small particle was used for the dominant matrix phase and a large particle for the reinforcing inclusion phase. For notation purposes in this thesis, the content of a compositional element will be denoted by volume percent Nickel. Composite elements below 50 vol.% Nickel are ceramic matrix composites (CMC) with large Nickel reinforcing particles. Elements above 50 vol.% Nickel are metal matrix composites (MMC) with large Alumina reinforcing particles. In composite theory, the percolation threshold occurs when discrete particle reinforcement transitions to a microstructure exhibiting long-range interconnectivity. As the percolation threshold

of 50 to 60 vol.% for Nickel-Alumina composites is approached, the phases begin to form interpenetrating networks with less desirable mechanical properties [12,24]. For this reason, the compositional gradient is reversed from a CMC in the Alumina-rich regions to a MMC in the Nickel-rich regions. The particle sizes and suppliers for all materials used in this research are given in Table 2.

Table 2: Base material powders used for this research.

Material	Type	Average Particle Size (μm)	Supplier
Nickel	123	3.9	Novamet, Wyckoff, NJ
	HDNP	12.6	Novamet, Wyckoff, NJ
Alumina	RC-HP	0.4	Baikowski Malakoff, Malakoff, TX
	Gilox-63	14.7	Alcoa World Chemicals
TiO_2	Anatase Nanopowder	0.015	Aldrich

2.2.2 Nanopowder TiO_2

Anatase nanopowder TiO_2 was chosen for use as a sintering additive in part due to its availability and relatively low cost. In addition, previous work has demonstrated small quantities of TiO_2 can promote grain growth at lower temperatures in pure Alumina [19,20]. For this research, 3 wt.% nanopowder TiO_2 was added to the pure Alumina for use in all composite compositions. By this methodology, TiO_2 content is constant in the Alumina at 3 wt.% but the total weight percent in each composite composition decreases with increasing Nickel content and decreasing Alumina content. Consequently, no TiO_2 is added to the 100 vol.% Nickel powder. The blending of powders was achieved by a conventional ball-mixing process. Basic properties of TiO_2 are presented in Table 3.

Table 3: Standard properties of TiO_2 [16].

Property	Titania
Composition	Anatase TiO_2
Density (g/cm^3)	3.9
Crystal Type	Tetragonal
Melting Temperature (˚C)	1830
Elastic Modulus (GPa)	282
Poisson's Ratio	.28
Yield Strength (MPa)	90
Fracture Toughness ($MPa\sqrt{m}$)	–
Hardness (HV)	910

2.2.3 Binder

Binder is typically added to powders in small quantities to facilitate the formation of unconsolidated green compacts. For this research, a low-density organic binder Q-PAC 40 (polypropylene carbonate, $CH_3CH_2CH_2{\cdot}CO_3$, 1.3 g/cm^3) was used in certain powder compositions. Previous work has demonstrated that this particular binder completely burns out during the firing cycle, leaving little or no residual carbon behind [18]. Additionally, this same work successfully used this binder to tailor compaction behavior and sintering performance in a thermal-behavior matching process. As the binder burns out at low temperature, voids are left behind for the powder to consolidate into. This additional porosity speeds up densification early in the sintering process. When combined with the selection of an appropriate critical compaction load (88 MPa) and particle size distribution, binder can be used to control three important sintering parameters: (1) sintering start temperature, (2) sintering rate, and (3) total shrinkage [18].

To apply the binder to the powders, Q-PAC 40 was dissolved in acetone in a controlled weight percentage and added to the powder compositions in predetermined quantities. These quantities are based off of previous work to match the relative

green density and subsequent shrinkage curves for the powder compositions [1,18]. Binder quantities are given in Table 4.

Table 4: Weight percent Q-PAC 40 binder added by powder composition.

Composition (vol.% Ni)	Binder (wt.%)
0	3.5
5	3.9
10	4.1
20	3.5
30	4.1
40	3.5
60	1.1
70	0
80	0
100	0

The binder-acetone solution was added to the pre-mixed powder compositions to form powder slurry. The acetone was then allowed to evaporate from the powder slurry, leaving behind the previously dissolved Q-PAC 40 binder. Once dry, the powder must be reground with a mortar and pestle and sieved through a 60-mesh sieve to 250 μm.

2.3 Powder Processing Technique

Powder processing begins with pure Nickel and Alumina powders and finishes as a composite green compact under cold press. Steel compaction dies are used to create individual graded structures. The creation of a discrete layered graded structure first requires the mixing of the base materials to appropriate composite powder compositions. The FGM structure consists of the two base materials on either end of the specimen, with the desired compositional gradient layered between the two

pure end layers, as seen in Figure 10. Figure 11 documents the entire discrete layering fabrication process.

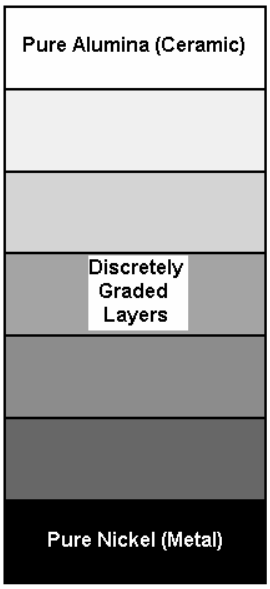

Figure 10: Discrete layered FGM structure.

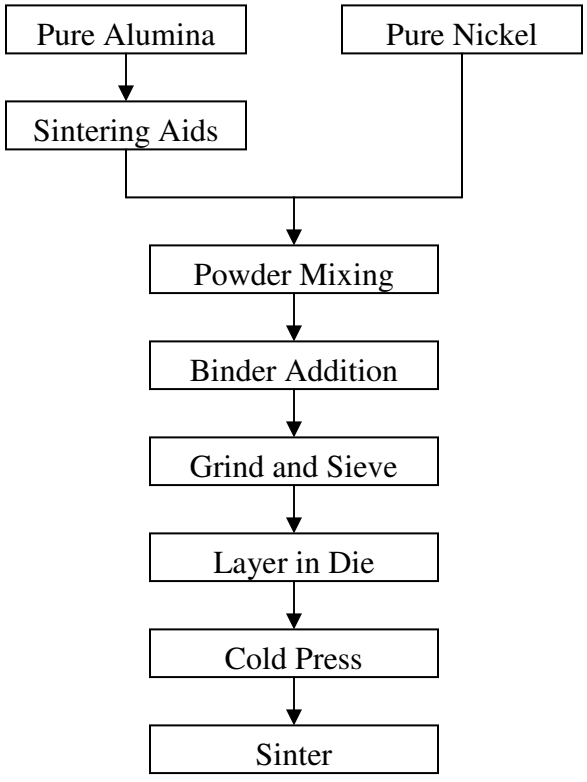

Figure 11: Die-based discrete layered powder processing fabrication technique.

2.3.1 Powder Preparation

Mixing time, methods, and available equipment have been varied in an attempt to improve powder mixing and reduce particle agglomerates. Moderate success has been achieved by ball-mixing appropriate quantities of Nickel, Alumina, and TiO_2 powders for approximately two hours. The pure base material powders are blended in a glass jar with ten to fifteen ½-inch ceramic balls on a rock tumbler to form the desired composite powder composition, as seen in Figure 12.

Figure 12: Ball-mixing assembly for preparing powder compositions.

Powders are mixed to form distinct composite compositions for use as a homogenous sample or within a gradient structure. Powder combinations employed by this research are given in Table 5. These powder combinations, particularly the 5 vol.% Nickel layer, are based on previous work that demonstrated a more gradual change in the gradient near the Alumina surface is more favorable for achieving stress reductions [15]. The pure Alumina (0 vol.% Nickel) has been studied in small

particle form (RC-HP), large particle form (Gilox-63), and a bimodal form (85% RC-HP, 15% Gilox-63). This particular bimodal Alumina has shown reduced sintering characteristics, which may be beneficial for some gradient structures [18,24,25]. Pure Nickel is studied in bimodal form (50% 123, 50% HDNP) only.

Table 5: Nickel-Alumina powder combinations used for this research.

	Alumina		Nickel	
Nickel (vol.%)	**RC-HP (.4µm)**	**Gilox-63 (14.7µm)**	**123 (3.9µm)**	**HDNP (12.6µm)**
0	X			
0		X		
0	X(.85)	X(.15)		
5	X			X
10	X			X
20	X			X
30	X			X
40	X			X
60		X	X	
70		X	X	
80		X	X	
100			X(.5)	X(.5)

2.3.2 Die-Based Discrete Layering

Two steel compaction dies have been machined for sample creation. The first die is a 25.4 mm diameter cylinder. The second die is a 31.75 mm sided square. Both these steel compaction dies can be seen in Figure 13. The first step in the fabrication process is to spray the appropriate die with zinc stearate dry powder mold release. Powders are then added sequentially to the die. To determine the amount of powder to add to the die, the desired sintered layer thickness, *t*, must be multiplied by the cross-sectional area, *A*, of the die cavity to determine the final sintered volume of the layer. This volume is multiplied by the theoretical density of the powder

composition, ρ_{layer}, based on a ROM formulation, to ultimately determine the mass of the powder to add, m_{layer}, as follows:

$$m_{layer} = \rho_{layer} At \tag{2}$$

The appropriate mass of composite powder is then poured into the empty die. The die ram is lowered and allowed to rest on the surface of the powder, but no additional pressure is applied. This procedure levels the powder layer within the die. The sequential discrete layering method employed by this research typically limits the tolerance control of the layer thickness to approximately 0.6 mm between the high and low points of the layer. The die is then removed and the next powder layer is added in similar fashion. Once all required powder compositions have been added to the die, the entire die assembly is transferred to a cold press. Using the cold press, the specimen is pressed to 88 MPa at room temperature and then removed from the die. The finished green sample is then ready for the sintering heat treatment in the furnace.

Figure 13: Steel compaction dies used for the fabrication of powder processed graded structures: 25.4 mm diameter cylinder (left) and 31.75 mm sided square (right).

2.3.3 Sintering Schedule

Previous work has developed a successful pressureless sintering cycle for Nickel-Alumina composites [1,24]. Sintering temperature is first ramped to 150˚C and held for 30 minutes to allow any accumulated moisture within the samples to burn off. The cycle then ramps to 400˚C and is held for two additional hours to burn out the organic binder previously added during powder preparation. From here, the cycle ramps to the full sintering temperature of 1350˚C and is held for four hours. Finally, the cycle cools down to 0˚C at a rate of 100˚C/hr. The entire sintering process was conducted under flowing Argon gas to prevent Nickel oxidation at high temperatures. Figure 14 documents the full furnace cycle.

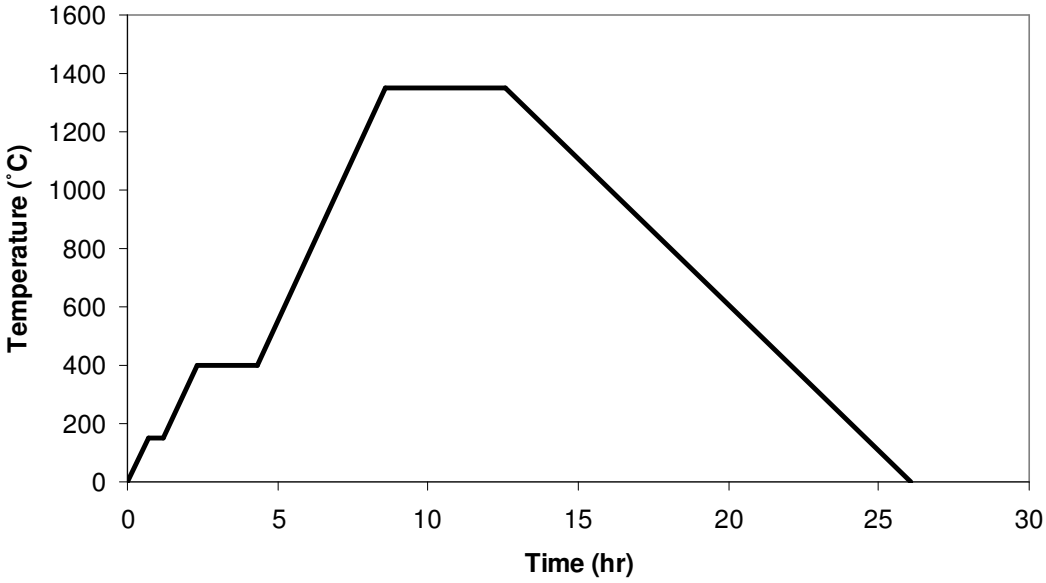

Figure 14: Furnace schedule used to pressureless sinter green compacts to final form.

2.4 Experimental Fabrication and Results

The die-based discrete layering technique has been used to produce a substantial number of gradient structure specimens. These specimens have been produced on a systematic basis by varying composition parameters. These

parameters include binder content, TiO_2 content, phase composition, and layer thickness. Due to the lack of sharp edges that concentrate stress, the cylindrical rod geometry is well suited for specimen characterization when geometrical effects are not to be considered. The emphasis of this section is to characterize role of the nanoparticle sintering aid on sintered composite properties and sintering behavior. For this reason, the square die is rarely used in this research.

2.4.1 Qualitative Results of TiO_2 Sintering Additive

The cylindrical rod die was used to process gradient structures with varying TiO_2 content to study the qualitative results of the sintered specimens. Eight-layer green compacts, approximately 20.5 mm in total green height, were studied. Powders were layered sequentially within the die with the following phase content: 0 (bimodal), 5, 10, 20, 40, 60, 80, and 100 vol.% Nickel. Figure 15 presents the results of several sintered structures with varying TiO_2 content location. The traditional non-TiO_2 rod specimen, presented as sample 1 in Figure 15, exhibits considerably more shrinkage on the MMC-side than the CMC-side of the specimen. The difference in gradient shrinkage has caused a large crack at the 40-60 vol.% Nickel interface. In this particular specimen, a small hairline crack also exists at the 10-20 vol.% Nickel interface. Adding TiO_2 to the 0 vol.% Nickel layer in sample 2 has caused the 40-60 vol.% Nickel interface crack to grow significantly larger. The gradient shrinkage slope of the CMC-side of the composite has also changed. The addition of TiO_2 to the top layer seems to have a shrinkage effect on the nearby Alumina-rich layers and ultimately pulls the 40 vol.% Nickel layer further away from the 60 vol.% Nickel layer. As seen in sample 3, adding TiO_2 to the 60 vol.% Nickel layer only causes an

even larger crack and "step-down" ridge effect between the 40 and 60 vol.% Nickel layers, whereby the edge of 40 vol.% layer is substantially raised above the 60 vol.% layer. The benefits of using TiO_2 begin to become apparent when the additive is included in the 40 and 60 vol.% Nickel layers in sample 4. A small ridge still exists, but the crack width has been reduced. Samples 5 and 6 further reduce this crack size by adding TiO2 to the 20-60 (i.e., 20, 40, 60) and 5-60 vol.% Nickel layers respectively. Sample 7 contains TiO_2 in the 0-60 vol.% Nickel layers. The width of the crack appears to have increased in sample 7, but the overall final shrinkage of the specimen is much more uniform. Finally, sample 8 continues this trend by adding TiO_2 to all appropriate layers: 0-80 vol.% Nickel. Crack width is similar to sample 7, but this sample appears very close to a perfect cylinder. The final shrinkage of each layer is very similar and no significant bulges in the gradient exist. The resulting sintered gradient profile is much different the profile exhibited by the traditional non-TiO_2 seen in sample 1.

No.	**TiO_2 Location**	
1	No TiO_2	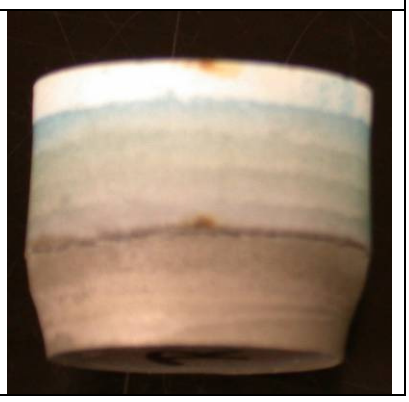

2	0 (Bi)	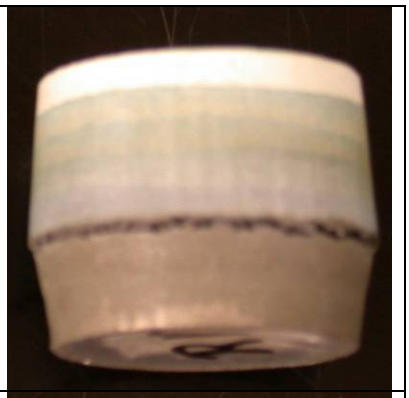
3	60	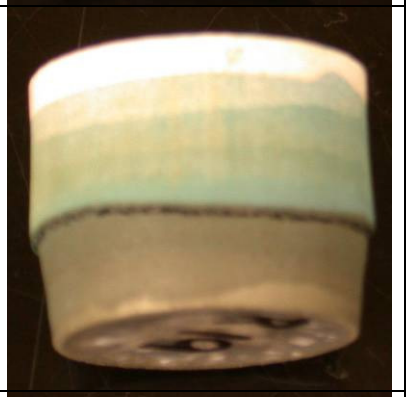
4	40, 60	
5	20, 40, 60	

6	5, 10, 20, 40, 60	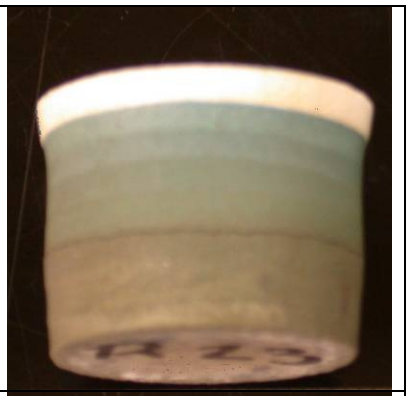
7	0(Bi), 5, 10, 20, 40, 60	
8	0(Bi), 5, 10, 20, 40, 60, 80	

Figure 15: Qualitative study of TiO_2 application to rod specimen gradients.

2.4.2 Layer Thickness and Composition Modifications

The role of layer thickness in specimen cracking was also studied qualitatively. By increasing layer thickness, residual stresses can be reduced at layer interfaces. Crack-free samples were eventually produced, the results of which will be discussed in detail in Chapter 3. These samples utilize substantially thicker layers than the samples studied in section 2.4.1 for TiO_2 content.

Composition modifications were made by adding 30 and 70 vol.% Nickel layers to the traditional eight-layer structures consisting of 0, 5, 10, 20, 40, 60, 80, and 100 vol.% Nickel. These new layers played a critical role in the production of crack-free samples in Chapter 3 by reducing residual stresses at the critical 40-60 vol.% interface. Along with the conventional compositions, the sintered properties of these new layers have been characterized for microstructure, porosity, and microhardness in the subsequent sections of this chapter.

2.5 Material Characterization

Material characterization is accomplished through green and sintered geometry measurements, microscopy, and microhardness measurements. These tools are used to document the effects of TiO_2 by taking measurements on samples that do and do not contain the nanoparticle sintering additive. Sintering behavior was also characterized by taking measurements on samples at progressive sintering temperatures.

To characterize each powder composition containing nanopowder TiO_2, single-layer homogeneous disks 5 mm in thickness were produced. A control disk set was created from powders lacking the TiO_2 additive. The initial height, diameter, and mass of the disks were recorded before pressureless sintering. Functionally graded specimens with multiple powder layers, in both circular and square cross-sectional geometries, were also created. Again, control samples were created for both the rod and rectangular geometries using powders without the TiO_2 additive. Following the sintering treatment in the furnace, the final height, diameter, and mass of the sintered

bodies were recorded to determine the final density and corresponding sintered porosity.

2.5.1 Composite Microstructure

Composite microstructure is characterized using microscopy techniques on sintered samples. Homogenous composite disks were grinded and polished to a final 0.05 μm diamond suspension polish on a Buehler Ecomet 3 variable speed grinder-polisher. The final five-step polishing procedure developed for the metal-ceramic composite specimens is given in Table 6.

Table 6: Final polishing schedule developed for sintered metal-ceramic composites.

Surface	Abrasive / Size	Base Speed (RPM) / Direction	Time (Min)
SiC Paper	1200 Grit (P-4000)	150 / Complementary	5
LECO Lecloth	6 μm MetaDi Polycrystalline Diamond Suspension	150 / Complementary	5
LECO Lecloth	3 μm MetaDi Polycrystalline Diamond Suspension	130 / Complementary	3
LECO Lecloth	1 μm MetaDi Polycrystalline Diamond Suspension	130 / Complementary	2
LECO Lecloth	.05 μm MetaDi Polycrystalline Diamond Suspension	100 / Contra (Opposite)	2

Following preparation of the homogenous disks, a Unitron Versamet optical microscope was used to image the specimens. As seen from the micrographs in Figure 16, the TiO_2 did not change the discrete particle reinforced microstructure or introduce any additional agglomerates. The white and black regions in the micrographs correspond to Alumina and Nickel particles respectively. The limitations of the laboratory ball-mixing apparatus previously described become apparent when viewing the micrographs, where large particle agglomerates are exhibited in all composite compositions. These agglomerates of the inclusion phase

typically inhibit the consolidation of the composite during sintering. The role of these agglomerates on sintering behavior will be discussed in detail in section 2.5.4. Improved ball-mixing on a more powerful mill would help eliminate some of these agglomerates.

Composition (vol.% Ni)	**Without TiO_2**	**With TiO_2**
5	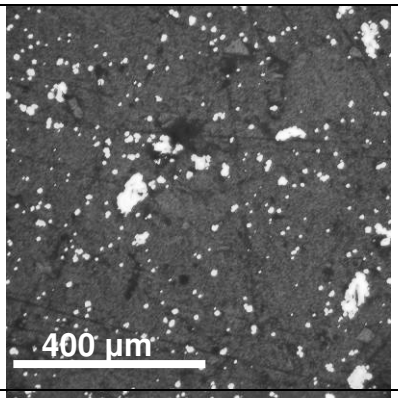	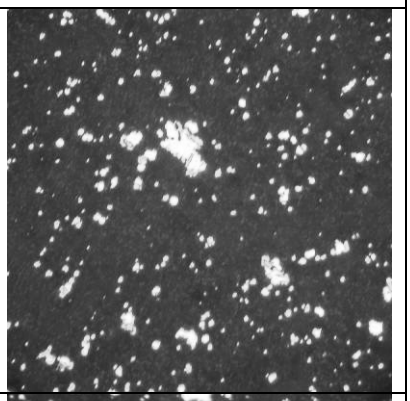
10	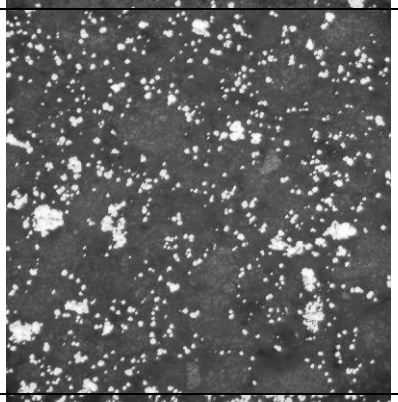	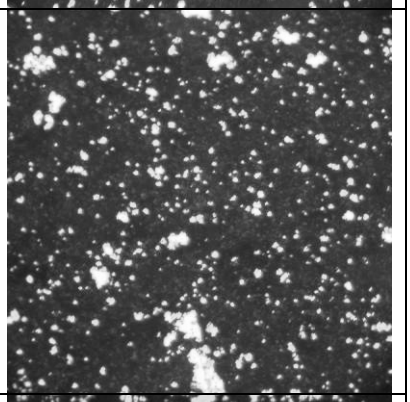
20	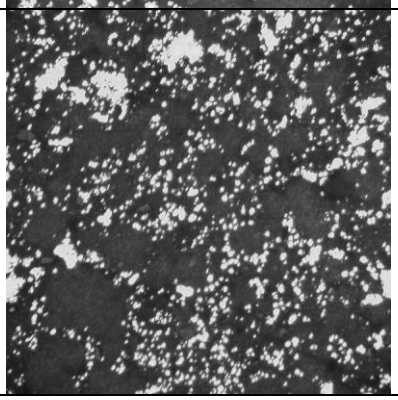	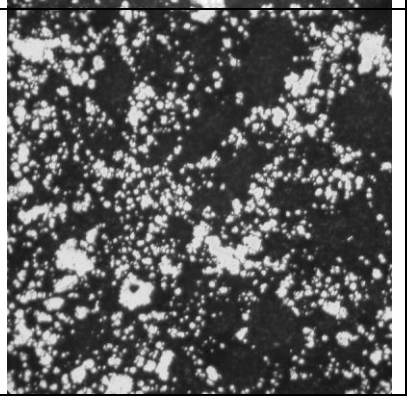

30	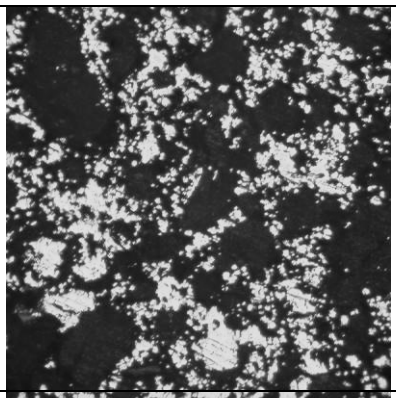	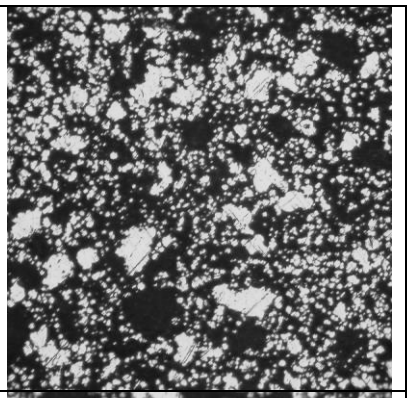
40	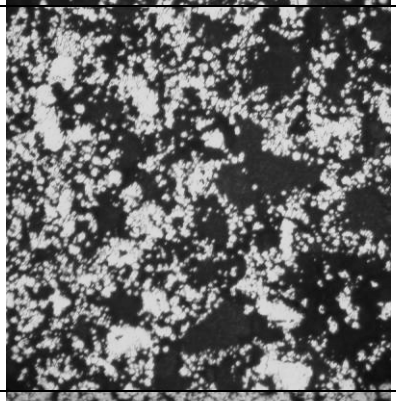	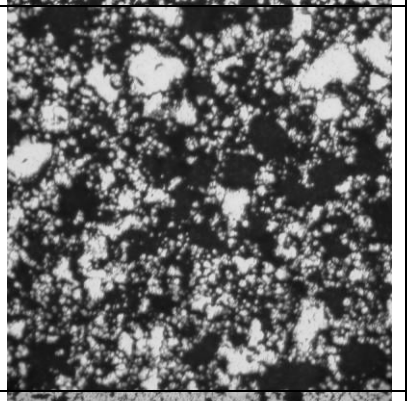
60	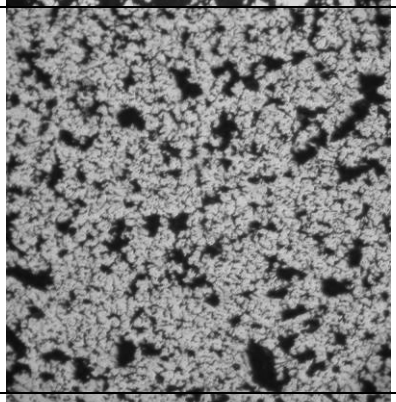	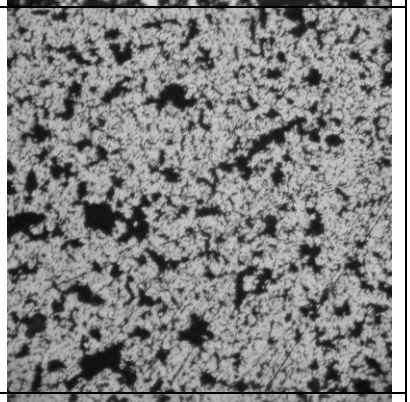
70	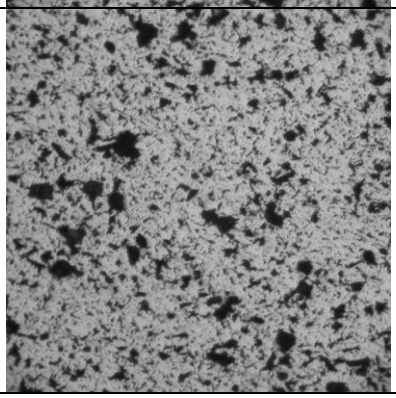	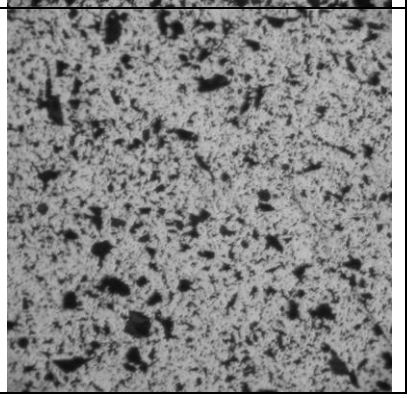

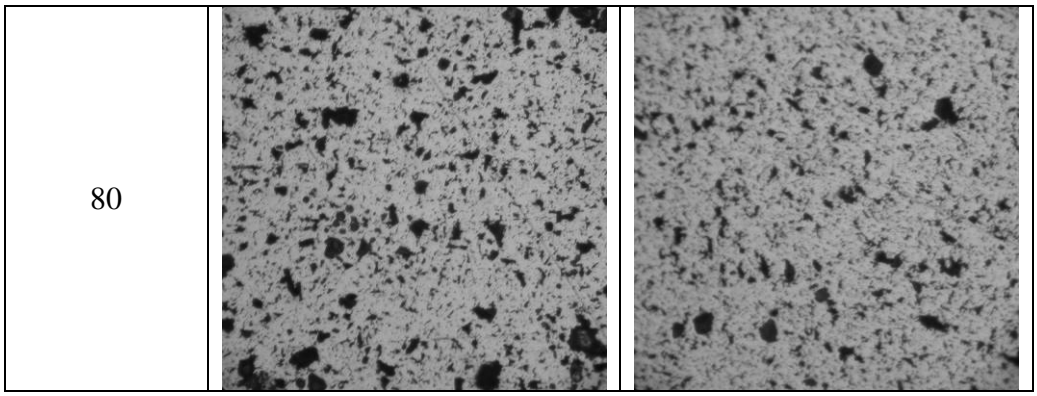

Figure 16: Micrographs of sintered homogeneous powder composites.

2.5.2 Porosity

Porosity is considered from a macroscopic approach, where predictions are made for the global response of the composite using volume fraction and properties of the individual phases [12]. Using geometry and mass measurements from the green and sintered homogeneous disks, the density and corresponding porosity of each disk sample can be calculated. To accomplish this, first the initial volume, V_i, of the green composite disk, a function of the initial height, h_i, and initial diameter, d_i, must be calculated as follows:

$$V_i = \frac{1}{4}\pi d_i^2 h_i \tag{3}$$

The disk diameter shrinkage, α, is based on the difference between the initial and final diameters of the specimen, as seen in (4). Assuming isotropic shrinkage of the composite, this can be used to correlate the initial volume to the final volume, V_f, in (5).

$$\alpha = \frac{d_i - d_f}{d_i} \tag{4}$$

$$V_f = V_i(1-\alpha)^3 \tag{5}$$

Measuring the sintered final mass, M_f, allows the final density, ρ_f, to be calculated in (6). The disk diameter shrinkage then can be used again to find the initial green density, ρ_i, in (7).

$$\rho_f = \frac{V_f}{M_f} \tag{6}$$

$$\rho_i = \rho_f (1-\alpha)^3 \tag{7}$$

The initial and final sintered porosity can then be calculated using the theoretical maximum-fired density, ρ_{th}. This theoretical fired density is based on a rule of mixtures formulation shown in (8) where v corresponds to phase volume fraction. The initial and final percent porosity, P_i and P_f respectively, are given by (9) and (10).

$$\rho_{\text{th}} = \rho_{\text{Ni}} v_{\text{Ni}} + \rho_{\text{Al}_2\text{O}_3} v_{\text{Al}_2\text{O}_3} \tag{8}$$

$$P_i = \left(\frac{\rho_{th} - \rho_i}{\rho_{\text{th}}} \right) \times 100 \tag{9}$$

$$P_f = \left(\frac{\rho_{th} - \rho_f}{\rho_{\text{th}}} \right) \times 100 \tag{10}$$

This final percent porosity of the sintered homogenous disks, as well as the corresponding initial percent porosity, is presented in Table 7. The final sintered porosity profile is shown in Figure 17.

The results show that the use of 3 wt.% TiO_2 as a sintering additive significantly increases the densification of each composite powder layer. Furthermore, the addition of the nanoparticle sintering aid has had little effect on the initial green density, which is an important factor in the thermal-behavior matching process. The biggest decrease in porosity due to TiO_2-influenced densification occurs

in the 10 and 20 vol.% Nickel compositions. The final porosity of the 10 vol.% Nickel layer decreases almost 80% as porosity is reduced from 20.6% to 4.2%. Similarly, the 20 vol.% Nickel layer experiences a 73% decrease in porosity from 22.2% to 6.0%.

With more apparent porosity than any other composite powder layer, the 60 vol.% Nickel layer presents an interesting case. Previous work has used the bulk modulus to determine the 60 vol.% Nickel layer exhibits a large amount of microstructural damage due to phase debonding [12]. This accounts for the poor sintering characteristics and high level of porosity in this layer. However, the TiO_2 still had a large impact, reducing porosity by 30% to 22.8%. Significant porosity is also observed in the large particle pure Gilox-63 Alumina. This powder composition has extremely poor sintering characteristics at the sintering temperature and the nanopowder TiO_2 has little effect on such a large particle size. Excluding large particle size powders, it is evident nanopowder TiO_2 can be applied as a sintering aid to reduce porosity not only in pure ceramics, but also metal-ceramic composites with great success at a pressureless sintering temperature of 1350˚C.

Table 7: Initial green and final sintered percent porosity of homogeneous composite disks. The percent decrease in final porosity due to the TiO_2 is shown.

	Initial P_i (%)		Final P_f (%)		
Composition (vol.% Ni)	Without TiO_2	With TiO_2	Without TiO_2	With TiO_2	Decrease (%)
0 (RC-HP)	42.0	44.1	18.8	7.0	62.7
0 (Gilox-63)	41.5	38.8	40.8	36.1	11.6
0 (Bimodal)	39.1	41.7	22.3	17.0	23.9
5	38.5	44.0	19.8	6.2	68.5
10	40.8	42.0	20.6	4.2	79.5
20	38.3	41.1	22.2	6.0	72.9
30	40.9	40.3	26.3	9.8	62.7
40	37.7	38.9	25.3	10.8	57.2
60	45.5	46.0	32.6	22.8	30.0
70	45.8	45.2	25.9	16.1	37.8
80	46.9	46.8	15.8	10.6	33.0
100	46.0	–	7.9	–	–

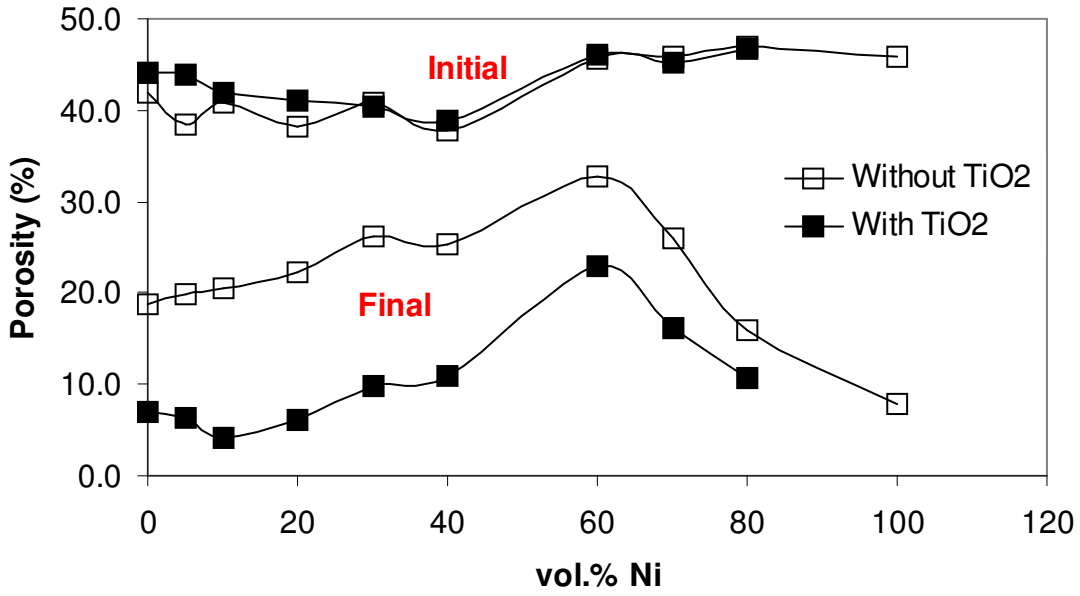

Figure 17: Initial and final porosity profiles of homogeneous composite disks.

2.5.3 Microhardness

Vickers microhardness is characterized using a Wilson Instruments MO Tukon Microhardness Tester. Loading is set at 500 g and held for 15 seconds on the surface of the sample using a standard 136˚ Vickers diamond pyramid indenter. The

TiO_2 has already demonstrated a significant role in reducing sintered porosity, which in turn has an effect on the hardness of the sintered composites.

Homogeneous composite disks were characterized first. Preparation followed the same grinding and polishing procedure presented earlier. A minimum of four microhardness measurements were taken on each homogeneous composite disk sample. The average measured Vickers microhardness and corresponding percent increase due to the inclusion of the TiO_2 sintering additive is given in Table 8. Reviewing the data, the TiO_2 sintering additive has increased microhardness in all applicable composite compositions. The largest gain is demonstrated in the 40 vol.% Nickel layer where microhardness has been increased approximately 85%. The variation of the Vickers microhardness profile, relative to the microhardness of pure RC-HP Alumina with TiO_2, for the entire composite disk range is show in Figure 18.

Table 8: Average Vickers microhardness (HV) of sintered homogeneous composite disks.

Composition (vol.% Ni)	Without TiO_2	With TiO_2	Increase (%)
0 (RC-HP)	911.8	1027.0	12.6
0 (Bimodal)	821.0	902.1	9.9
5	741.1	806.2	8.8
10	667.9	759.2	13.7
20	269.1	355.0	31.9
30	248.3	316.9	27.6
40	119.5	221.4	85.2
60	37.0	63.5	71.3
70	84.8	132.2	55.9
80	75.1	86.2	14.8
100 (Bimodal)	52.7	–	–

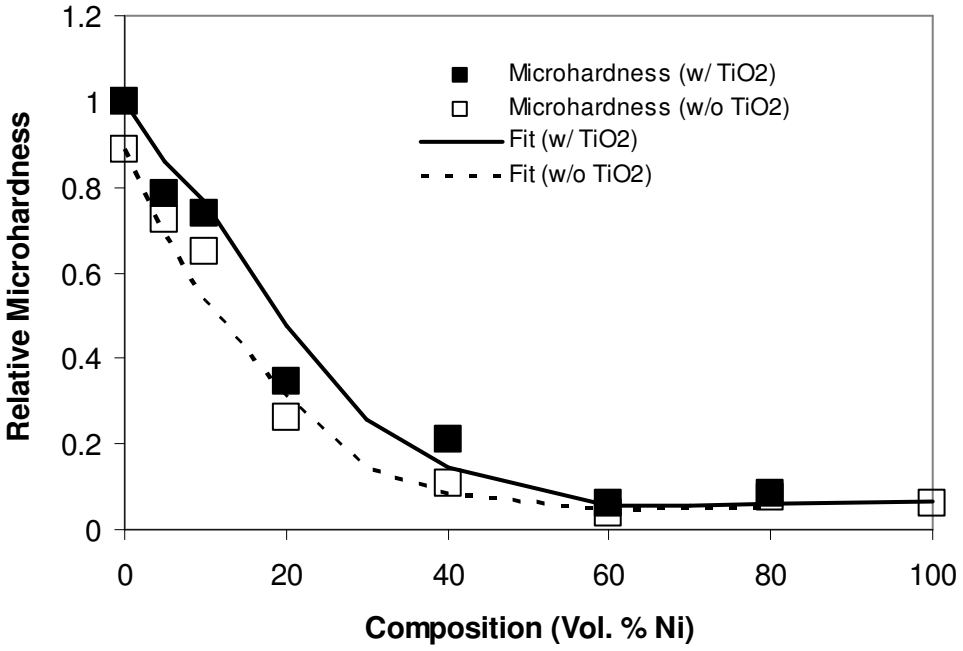

Figure 18: Variation of average Vickers microhardness for sintered homogeneous composite disks relative to the microhardness of pure RC-HP Alumina with TiO_2.

In order to understand the relationship between porosity in Table 7 and the Vickers microhardness measurements in Table 8, a power law formulation was used. In this formulation, the powder is assumed to be a three-phase material consisting of matrix volume fraction, v_{matrix}, particle volume fraction, $v_{particle}$, and porosity. Consequently, the final volume fraction of the matrix material in the composite is given in (11). Using this final volume fraction of the matrix, the power law formulation is given in (12).

$$(v_{matrix})_{final} = 1 - (v_{particle})_{final} - P_f \quad \textbf{(11)}$$

$$HV = \left((v_{matrix})_{final}\right)^n HV_m^{pure} \quad \textbf{(12)}$$

In (12), n is a power law exponent and HV_m^{pure} is the Vickers microhardness of the fully dense pure matrix material. The values of n are determined from fitting the

microhardness data. Using the microhardness measurements of the pure RC-HP Alumina with and without TiO_2, the values of HV_m^{pure} could be determined. The resulting values for Alumina and Nickel as the matrix material can be seen in Table 9.

Table 9: Components of the power law formulation for Vickers microhardness as determined from experimental data.

Matrix Material	HV_m^{pure}	n
Alumina	2100	4
Alumina (w/ TiO_2)	1325	3.5
Nickel	53	0.25

Reviewing these results, the microhardness for the fully dense pure Alumina without the nanoparticle sintering aid would be nearly 50% greater than what would be obtained using the sintering aid. However, the higher microhardness in the non-TiO_2 ceramic is attributed to the higher volume fraction of the matrix material concurrent with a lower porosity at higher sintering temperatures. Indeed, the addition of the nanopowder TiO_2 introduces impurities to the RC-HP Alumina, which are known to reduce strength and hardness. The addition of the nanopowder TiO_2 also results in a lower sensitivity, or a lower power law exponent, to the volume fraction of the matrix material. This can also be considered as less sensitivity to composite porosity. Thus, for pressureless sintering processes for graded metal-ceramic composites, where the control of porosity is limited by the melting point of the metal, there is a distinct benefit in reducing the porosity through the use of a nanoparticle sintering aid. However, for pressure-assisted thermal processes like Hot Isostatic Pressing, this benefit will most likely be lost. For the fully sintered pure Nickel, which does not use the nanoparticle sintering aid, the microhardness would be

less than the Alumina by over an order magnitude and would also be less sensitive to porosity by an order of magnitude.

Vickers microhardness measurements were also obtained from graded rod and square specimens. The evolution of hardness in a gradient structure is heavily influenced by the residual stresses and shrinkage constraints produced by the compositional gradient. Reducing shrinkage constraints by modifying the sintering kinetics of the gradient can boost the hardness of the entire specimen. While a thermal-behavior matching process has been adapted to all specimens from previous work [1,18], the use of the TiO_2 sintering additive further alters sintering kinetics. These changes in sintering behavior will be discussed in detail in the following section.

The first gradient structure studied was an eight-layer cylindrical rod specimen. The following powder compositions, in order of sequential layering within the die, were used: 0 (bimodal), 5, 10, 20, 40, 60, 80, and 100 vol.% Nickel. One rod was constructed using powders containing the TiO_2 sintering additive and one rod without the TiO_2. The green specimen containing TiO_2 was approximately 20.5 mm in height. A previously made rod specimen, approximately 23.5 mm in green specimen height, was used for the non-TiO_2 rod. As seen in Figure 19, both specimens experienced cracking at the 40-60 vol.% Nickel interface during the sintering process. To properly test the structures, the samples had to be grinded and polished to a flat surface at one point along the circumference of the cylinder. The final sintered layer thickness at this location is given in Table 10.

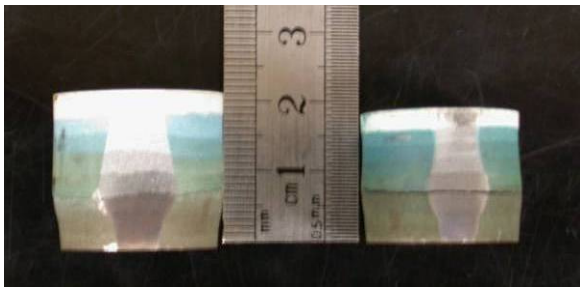

Figure 19: Non-TiO_2 rod (left) and TiO_2 rod (right) specimens.

Table 10: Sintered layer thickness (mm) of rod specimens used for microhardness profile evaluation.

Layer (vol.% Ni)	Rod Without TiO_2	Rod With TiO_2
0 (Bimodal)	2.7	2.2
5	2.9	2.1
10	2.0	2.1
20	2.5	2.1
40	2.5	2.5
60	3.6	2.8
80	2.8	2.1
100	2.3	2.1
Total Height:	21.3	18.0

Vickers microhardness measurements were taken sequentially down the length of the polished surface. The Vickers microhardness profile for both rod specimens is presented in Figure 20. Reviewing the results, the rod microhardness profile is similar to the homogeneous disk profile, except in the 0, 5, 10, and 20 vol.% Nickel regions. Residual sintering stresses appear to have a significant effect on hardness in these regions. Previous modeling efforts describing the stress evolution in a pressureless sintering process have indicated that the stresses are compressive in the 5, 10, and 20 vol.% Nickel region and tensile in the 0 vol.% Nickel region [28]. Compressive pressure aids porosity reduction, which increases hardness, while the tensile pressure in the 0 vol.% Nickel region has the opposite effect.

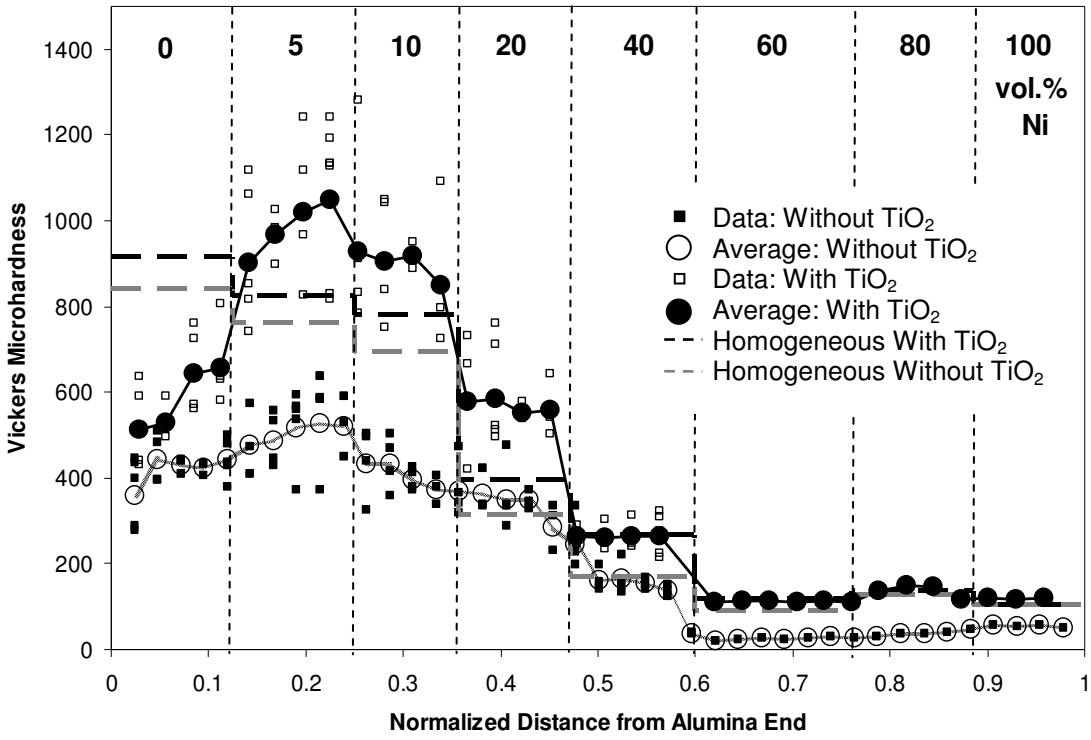

Figure 20: Vickers microhardness profile by distance along rod specimen gradient.

The second gradient structure studied was an eight-layer square specimen. Unlike the rod specimen, the gradient used in the square geometry did not contain a pure Nickel layer. Instead, a secondary 60 vol.% Nickel layer replaced the pure Nickel layer in an attempt to limit MMC-side shrinkage of the structure. In order of sequential layering, the following powder compositions were used: 0 (bimodal), 5, 10, 20, 40, 60, 80, and 60 vol.% Nickel. Again, one square sample was made with TiO_2 powders and one without. Green compacts were approximately 26.5 mm in height. The grinded and polished square specimens can be seen in Figure 21. The TiO_2 square experienced cracking at the 40-60 and 60-80 vol.% Nickel interfaces.

The non-TiO_2 square cracked at the 5-10 and 40-60 vol.% interfaces. The final sintered layer thickness on the polished side of the samples is given in Table 11.

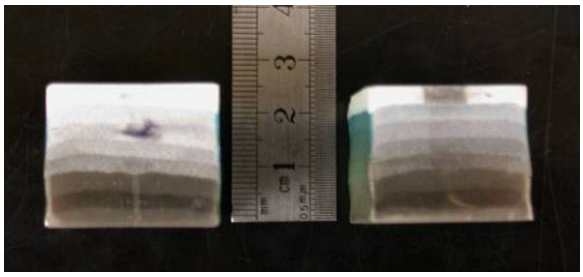

Figure 21: Non-TiO_2 square (left) and TiO_2 square (right) specimens.

Table 11: Sintered layer thickness (mm) of square specimens used for microhardness profile evaluation.

Layer (vol.% Ni)	Square Without TiO_2	Square With TiO_2
0 (Bimodal)	3.3	3.0
5	3.0	2.7
10	3.0	3.0
20	2.7	2.6
40	2.8	3.4
60	3.2	3.2
80	2.8	3.4
60	2.9	1.8
Total Height:	23.7	23.1

Vickers microhardness measurements were again taken sequentially down the length of the square specimens. The resulting microhardness profile can be seen in Figure 22.

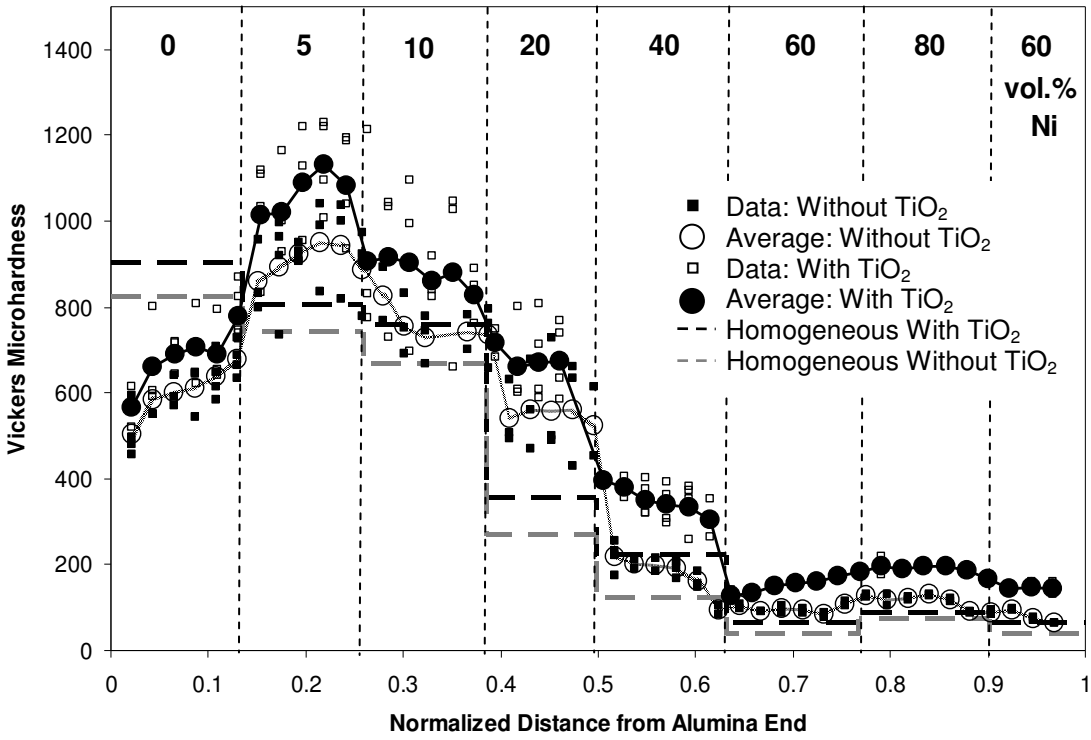

Figure 22: Vickers microhardness profile by distance along square specimen gradient.

The square sample with TiO_2 recorded the highest Vickers microhardness of all the gradient structures tested. Profile shape is very similar to the rod specimens previously tested, where peak microhardness is observed in the 5 vol.% Nickel layer. The same explanations for residual stress behavior can be made to explain the resulting evolution of the microhardness profile. Additionally, both the rod and square samples with TiO_2 showed large improvements over the non-TiO_2 counterparts. The 60 and 80 vol.% Nickel layers in the rod sample recorded the most significant Vickers gains, posting increases of over 100%. The gains in Vickers microhardness for both the rod and square samples are presented in Table 12.

Table 12: Average Vickers microhardness (HV) by layer in rod and square gradient structures.

	Rectangular Specimen			Cylindrical Specimen		
Layer (vol.% Ni)	**Without TiO_2**	**With TiO_2**	**Increase (%)**	**Without TiO_2**	**With TiO_2**	**Increase (%)**
0 (Bimodal)	589.9	679.8	15.2	439.5	582.2	32.5
5	867.2	981.5	13.2	509.4	936.4	83.8
10	725.0	875.9	20.8	458.3	822.9	79.5
20	513.9	668.2	30.0	348.5	540.9	55.2
40	202.0	288.4	42.8	172.1	207.2	20.4
60	104.3	113.0	8.4	27.4	59.0	115.2
80	125.8	146.3	16.4	36.4	91.0	150.1
60 / 100	84.6	93.8	10.9	54.4	59.0	8.5

2.5.4 Sintering Behavior

Constitutive models often consider metal-ceramic composite powders as a three-phase material consisting of voids, ductile metal particles, and brittle ceramic particles [28]. The behavior of each phase is distinct, in which the metal particles deform elastoplastically, ceramic particles deform elastically, and porosity, represented by void volume fraction, is directly related to the shrinkage. Considering these phases, the gradient structure is divided into three regions: (1) regions of pure metal or pure ceramic, (2) a metal matrix with large reinforcing ceramic particles, and (3) a ceramic matrix with large reinforcing metal particles. The sintering process is described in Figure 23 where diffusion between particles forms solid bonds that reduce surface energy by reducing interfacial area. As matrix particles sinter between themselves and around the reinforcement particles, porosity is reduced. Specifically, sharp increases in porosity reduction are observed as sintering begins due to the nucleation of loosely packed particles. As sintering continues, porosity consumption levels off due to the lack of small pores remaining to consume as well as the lack of energy to overcome the surface energy of the large pore sizes that remain [25].

Additional reductions in porosity can occur due to the formation of matrix shrinkage-induced microstresses that lead to plastic deformation of the ductile metal phase [28].

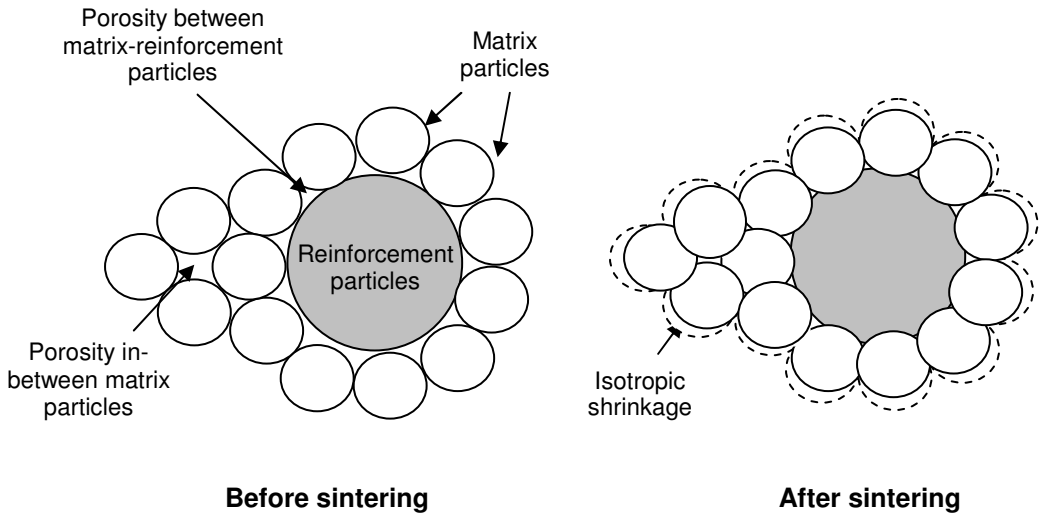

Figure 23: Densification behavior of matrix particles, reinforcement particles, and porosity during pressureless sintering [28].

The sintering behavior of the composite powder compositions was characterized by studying homogeneous disks sintered to progressive sintering temperatures. Temperatures of interest were 750˚C, 950˚C, 1150˚C, 1350˚C without hold, and 1350˚C with normal four hour hold time. The linear shrinkage of the disk diameter was recorded at each sintering temperature. Note that 30 and 70 vol.% Nickel compositions have not been characterized in non-TiO_2 form; therefore, for lack of comparison these powder compositions have been removed from the shrinkage characterization study.

The presence of the TiO_2 sintering additive significantly alters sintering kinetics. For powder compositions 60 vol.% and less, the sintering rate has been increased. On the other hand, the 80 vol.% layer exhibits a slower rate. As a consequence, the TiO_2 powder curves tend to converge more so than the original non-

TiO_2 curves. In support of thermal matching theory, the more the lines converge on a single sintering rate profile, the less differential shrinkage occurs. Figure 24 presents this convergence in a combined plot of all these sintering curves.

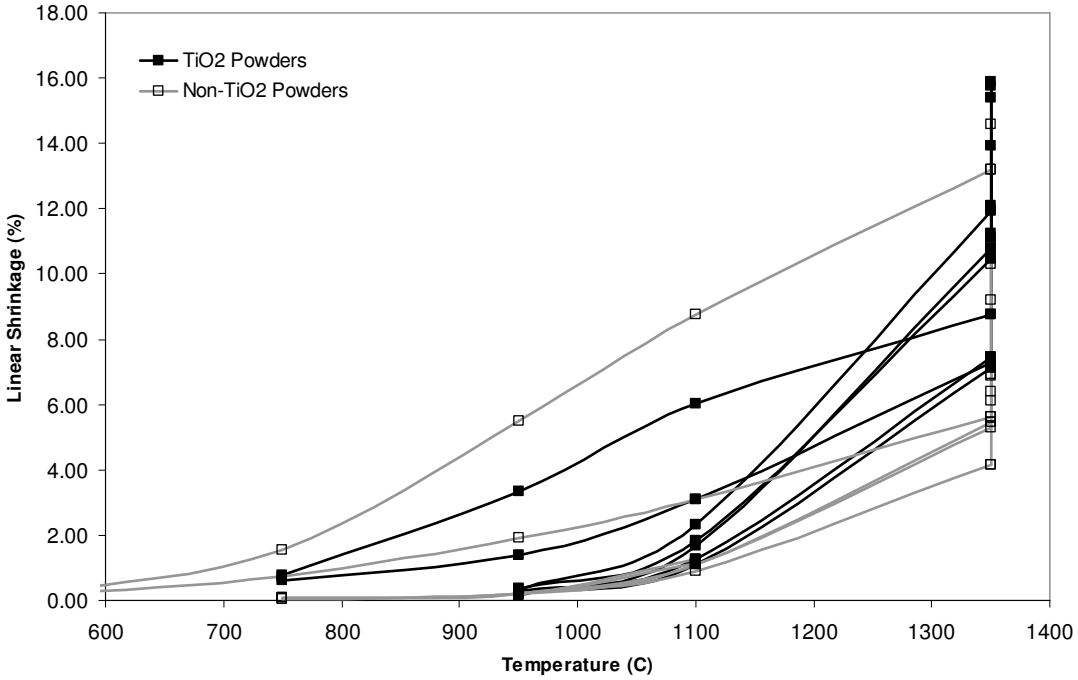

Figure 24: Convergence of shrinkage rates for TiO_2 powders versus non-TiO_2 powders. 100 vol.% Nickel is not included.

To understand the effects of the nanopowder TiO_2 sintering aid on shrinkage, previous research on the modeling of the shrinkage behavior of metal-ceramic composites was used [25]. A Weibull power law time-dependent exponential equation, consistent with the Kolmogorov-Johnson-Mehl-Avrami (KJMA) kinetic theory of nucleation and growth, was used as the basis for the model to fit the shrinkage data. The equations used in the sintering model are as follows:

$$\varepsilon(t) = c_0\left(1 - e^{-c_1 t^n}\right) \tag{13}$$

$$\frac{d\varepsilon}{dt} = c_0 c_1 n(t^{n-1}) e^{(-c_1 t^n)} \tag{14}$$

In (14), the power law exponent, n, also obeys a power law thermally-dependent exponential relationship as follows:

$$n(T) = c_2\left(1 - e^{-c_3 T^p}\right) \tag{15}$$

Fitting the shrinkage data from sintering experiments at progressive sintering temperatures, the unknown coefficients c_o, c_1, c_2, c_3, and exponent p can be determined.

Agglomerated particles can introduce additional porosity to the composite that can be characterized using a previously developed porosity reduction model [24]. This additional porosity associated with the agglomerated particles is not removed during sintering, thus it acts to retard the shrinkage of the particle-reinforced composite. To address this effect on sintering behavior, the sintering model must be modified using the data from the previously developed porosity reduction model and the fits of the KJMA sintering model to the pure Nickel and pure Alumina specimens. The additional porosity is assumed to reduce the effective volume fraction of matrix material that will actually sinter, $(v_{matrix})_{sintered}$. This additional porosity can be associated with the matrix material, which effectively changes the volume fraction of porosity in the matrix. Consequently, the volume fraction of the sintered matrix material can be determined from its impact on the final volume fraction of porosity in the matrix, $((v_{porosity})_{matrix})_{final}$, using the final volume fraction of the matrix, $(v_{matrix})_{final}$, and the initial and final porosity of the pure matrix material, P_{pure}, as follows:

$$\left(\left(v_{porosity}\right)_{matrix}\right)_{final} = \left(v_{matrix}\right)_{final}\left[\left(\frac{P_{pure}}{1-P_{pure}}\right)_{initial} + \left(v_{matrix}\right)_{sintered}\left(\left(\frac{P_{pure}}{1-P_{pure}}\right)_{final} - \left(\frac{P_{pure}}{1-P_{pure}}\right)_{initial}\right)\right] \tag{16}$$

The left hand side of Equation (16) can now be solved in terms of $(v_{matrix})_{final}$ using equations from the porosity reduction model. This allows the volume fraction of sintered matrix material to be determined using just the initial and final volume fraction of measured porosity in the composites, P_i and P_f respectively, which are found in Table 7. Assuming the volume fraction of porosity associated with the matrix, $(v_{porosity})_{matrix}$, does not change with volume fraction of the matrix (i.e., it is constant), it can be expressed as follows:

$$\frac{\left(v_{porosity}\right)_{matrix}}{v_{matrix}} = \frac{P_{pure}}{1 - P_{pure}} = constant \qquad \textbf{(17)}$$

In Equation (17), the volume fraction of porosity associated with the matrix material is computed using the known volume fraction of the matrix material, v_{matrix}, and the known ratio of porosity to matrix material. The value P_{pure} is the amount of porosity in the pure matrix material. Next, the porosity associated with the presence of the reinforcing inclusion phase, $(v_{porosity})_{particle}$, is simply the difference between the porosity in the composite material, P, and the partial volume fraction of the porosity due to the matrix phase:

$$(v_{porosity})_{particle} = P - (v_{porosity})_{matrix} \qquad \textbf{(18)}$$

As mentioned previously, the particle porosity is considered a fixed third phase of the matrix and particle system. Thus, its volume fraction relative to these two materials will always be the same. This third phase will have the following relationship to the volume fraction of the matrix:

$$\frac{\left(\left(v_{porosity}\right)_{particle}\right)_{final}}{(v_{matrix})_{final}} = \frac{\left(\left(v_{porosity}\right)_{particle}\right)_{initial}}{(v_{matrix})_{initial}} \qquad \textbf{(19)}$$

A summation of all of the constituents is the basis for determining the final volume fractions of the matrix and porosity, where the porosity is broken into two parts for the matrix and particle porosity:

$$v_{Ni} + v_{Al_2O_3} + (v_{porosity})_{particle} + (v_{porosity})_{matrix} = 1 \quad \textbf{(20)}$$

In terms of the volume fraction of the matrix material Equation (20) is:

$$(v_{matrix})_{final} + (v_{matrix})_{final} v^* + (v_{matrix})_{final} \frac{((v_{porosity})_{particle})_{initial}}{(v_{matrix})_{initial}} + (v_{matrix})_{final} \left(\frac{P_{pure}}{1 - P_{pure}} \right)_{final} = 1 \quad \textbf{(21)}$$

$$v^* = \begin{cases} \dfrac{1 - v_{\mathrm{Ni}}}{v_{\mathrm{Ni}}} & \text{for Ni matrix,} \\ \dfrac{v_{\mathrm{Ni}}}{1 - v_{\mathrm{Ni}}} & \text{for } Al_2O_3 \text{ matrix.} \end{cases} \quad \textbf{(22)}$$

The relation for the volume fraction of the matrix material that is sintered is now as follows:

$$(v_{matrix})_{sintered} = \frac{(1 + v^*) \left[\dfrac{P_f}{(1 - P_f)} - \dfrac{P_i}{(1 - P_i)} \right]}{\left(\left(\dfrac{P_{pure}}{1 - P_{pure}} \right)_{final} - \left(\dfrac{P_{pure}}{1 - P_{pure}} \right)_{initial} \right)} \quad \textbf{(23)}$$

Values for $(v_{matrix})_{final}$, $(v_{porosity})_{final}$, $(v_{porosity})_{initial}$, and $(v_{matrix})_{sintered}$ can be seen in Table 13 for composites without the nanopowder TiO_2 sintering aid and in Table 14 for composites with the sintering aid. Previous data [25] was used for the values of $(v_{porosity})_{initial}$.

Table 13: For powders without TiO_2, volume fractions of the sintered matrix, final matrix, and porosities when there is no porosity associated with particle agglomeration.

Composition (vol.% Ni)	$(v_{matrix})_{final}$	$(v_{porosity})_{final}$	$(v_{porosity})_{initial}$	$(v_{matrix})_{sintered}$
0 (RC-HP)	0.81	0.19	0.41	1.00
5	0.76	0.20	0.41	1.00
10	0.71	0.21	0.40	0.96
20	0.62	0.22	0.39	0.97
40	0.45	0.25	0.36	0.92
60	0.40	0.33	0.47	0.62
80	0.67	0.16	0.49	0.97
100	0.92	0.08	0.52	1.00

Table 14: For powders with TiO_2, volume fractions of the sintered matrix, final matrix, and porosities when there is no porosity associated with particle agglomeration.

Composition (vol.% Ni)	$(v_{matrix})_{final}$	$(v_{porosity})_{final}$	$(v_{porosity})_{initial}$	$(v_{matrix})_{sintered}$
0 (RC-HP)	0.93	0.07	0.41	1.00
5	0.89	0.06	0.41	1.24
10	0.86	0.04	0.40	1.21
20	0.75	0.06	0.39	1.20
40	0.53	0.11	0.36	1.11
60	0.46	0.23	0.47	1.06
80	0.71	0.11	0.49	1.06

The calculated values of the sintered matrix material from Equation (23) can be used to predict sintering behavior. The fits of the KJMA model sintering model for the pure Nickel and pure Alumina must be scaled using the values from Equation (23) and the final volume fraction of matrix, normalized by the final volume fraction for the pure matrix material. Reviewing the experimental data, there is a 200°C shift in the initial sintering temperature for the Nickel-rich compositions without the nanopowder TiO_2 sintering aid and a 100°C shift with TiO_2, indicating a retardation in the sintering behavior using the nanoparticle sintering aid. The model results, plotted on top of experimental data, can be seen in Figure 25 for the non-TiO_2 powders and Figure 26 for the powders containing TiO_2. Reviewing the figures,

results indicate that the model can not be used to predict the shrinkage behavior of the composites with the TiO_2 nanopowder sintering aid as well as it has done for powders without the sintering aid.

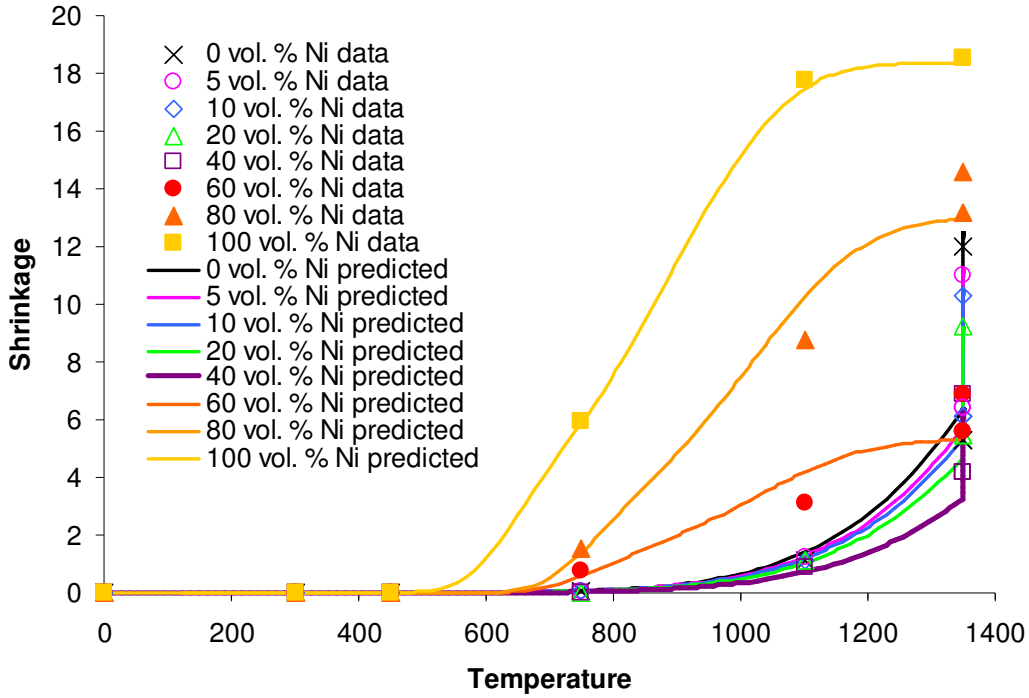

Figure 25: Shrinkage curves for non-TiO_2 composite powders.

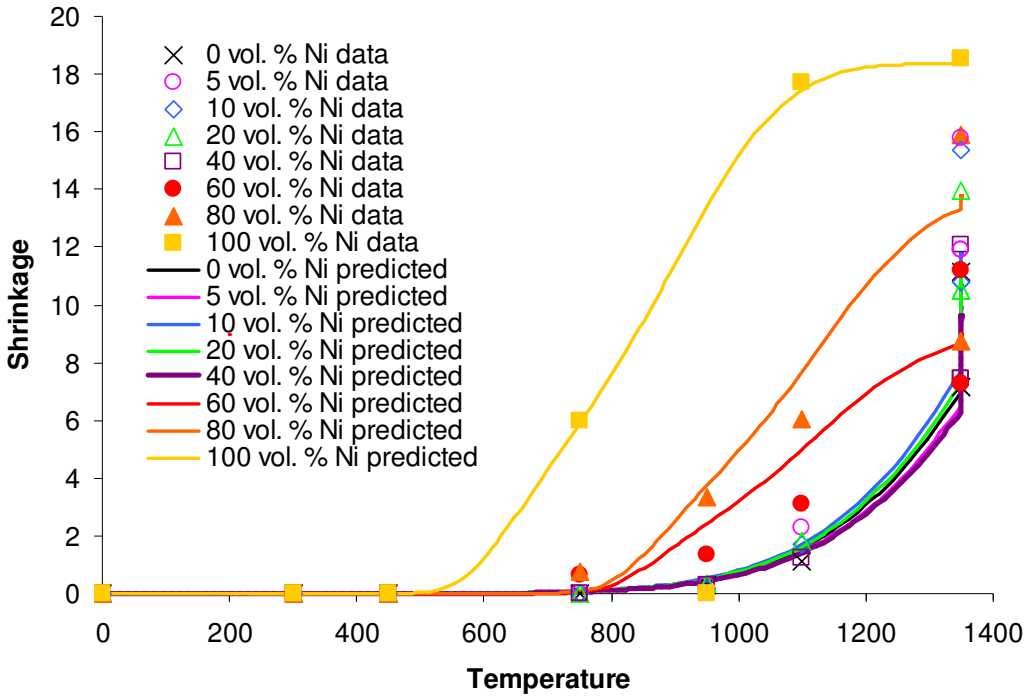

Figure 26: Shrinkage curves of TiO_2 composite powders. The 100 vol.% Nickel powder is plotted for reference purposes and does not contain the nanopowder TiO_2 sintering aid.

In order to understand the differences in the predicted sintering behavior of the composites with and without the nanopowder TiO_2 sintering aid, the sintering model was modified to permit sintering of the agglomerated reinforcing particles when the TiO_2 nanopowder sintering aid is employed. To accomplish this, the level of sintering for the agglomerated reinforcing particles must be determined from the initial and final porosities as follows:

$$P_{initial} = \frac{v^*_{matrix}\left(\frac{P_{pure}}{1-P_{pure}}\right)_{initialmatrix} + \left(v_{porosity}\right)_{unsintered} + v^*_{particle}\left(v_{particle}\right)_{sintered}\left(\frac{P_{pure}}{1-P_{pure}}\right)_{initialparticle}}{1+v^*_{matrix}\left(\frac{P_{pure}}{1-P_{pure}}\right)_{initialmatrix} + \left(v_{porosity}\right)_{unsintered} + v^*_{particle}\left(v_{particle}\right)_{sintered}\left(\frac{P_{pure}}{1-P_{pure}}\right)_{initialparticle}} \quad \textbf{(24)}$$

Where:

$$\left(v_{porosity}\right)_{unsintered} = \frac{P_{final} + v^*_{matrix}\left(\frac{P_{pure}}{1-P_{pure}}\right)_{finalmatrix} + v^*_{particle}\left(\frac{P_{pure}}{1-P_{pure}}\right)_{finalparticle}\left(1-P_f\right)}{\left(1-P_f\right)} \quad \textbf{(25)}$$

$$\left(v_{matrix}\right)_{sintered} = \frac{v^*_{matrix}\left[1+\left(\frac{P_{pure}}{1-P_{pure}}\right)_{matrix}\right] + v^*_{particle}\left(\frac{P_{pure}}{1-P_{pure}}\right)_{particle}\left(1-P_f\right)}{\left(1-P_f\right)} \quad \textbf{(26)}$$

In these equations, v^*_{matrix} and $v^*_{particle}$ are the volume fractions of the matrix and particle phases in the composite if there was no porosity. Additionally, $\left(v_{porosity}\right)_{unsintered}$ is now the volume fraction of the initial porosity that remains unsintered and $\left(v_{particle}\right)_{sintered}$ is the volume fraction of reinforcing particles that are sintered, which is similar to $\left(v_{matrix}\right)_{sintered}$ in the original model. In the modified model, the entire matrix is sintered and the remaining unsintered volume fraction of the initial porosity is still associated with agglomerated particles. However, there is a portion of the initial porosity associated with the agglomerated particles that is removed by sintering, which is similar to the portion of the initial porosity associated with the matrix in the original model.

Applying the modified model, the values for Equations (24)-(26) can be seen in Table 15. These values can now be used to calculate the shrinkage of the composites by using the final volume fraction of matrix and the volume fraction of the particles that sinter. The resulting shrinkage curves can be seen in Figure 27. Additionally, the predicted and actual shrinkage results are compared in Figure 28 for the final shrinkage and shrinkage at the four hour hold at 1350^{o}C. From these figures,

it can be concluded that the predictions using the modified model are not only more realistic, but more accurately describe the shrinkage behavior that is observed with the TiO_2 nanoparticles than the original model. The nanoparticles appear to be enhancing the sintering of agglomerated particles while more substantially retarding the sintering of the nickel.

Table 15: For powders with TiO_2, volume fractions of the final matrix, unsintered porosity, and sintered particle phase when there is porosity associated with particle agglomeration.

Composition (vol.% Ni)	$(\nu_{matrix})_{final}$	$(\nu_{porosity})_{unsintered}$	$(\nu_{particle})_{sintered}$
5	0.96	0.00	0.93
10	0.92	0.00	0.44
20	0.81	0.00	0.42
40	0.57	0.07	0.27
60	0.50	0.25	0.30
80	0.77	0.05	0.93

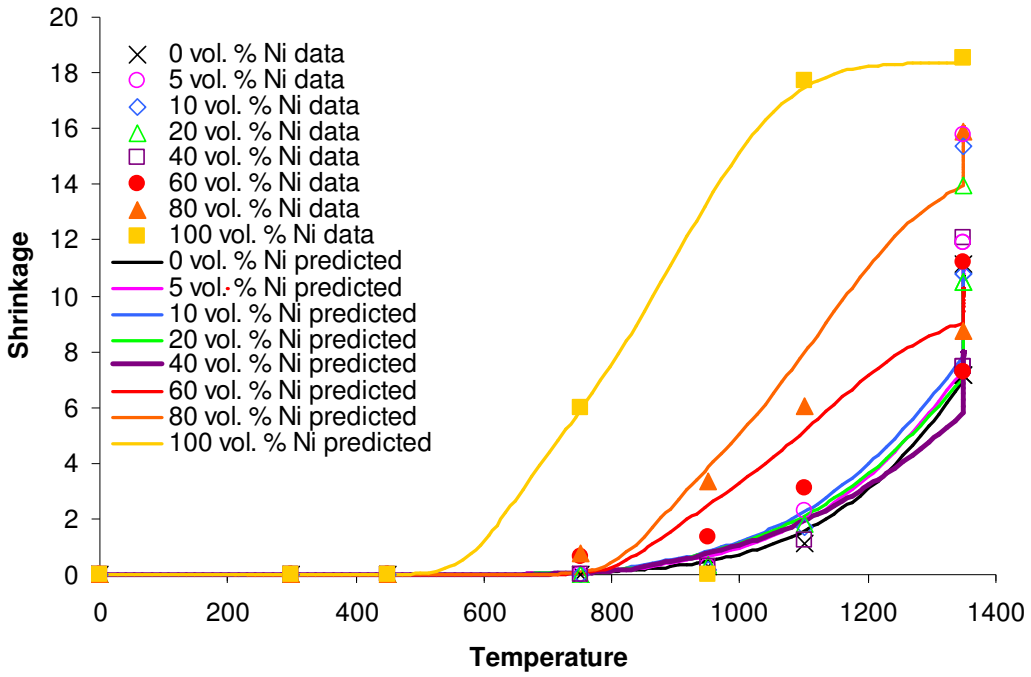

Figure 27: Shrinkage curves predicted using modified model for TiO_2 powders.

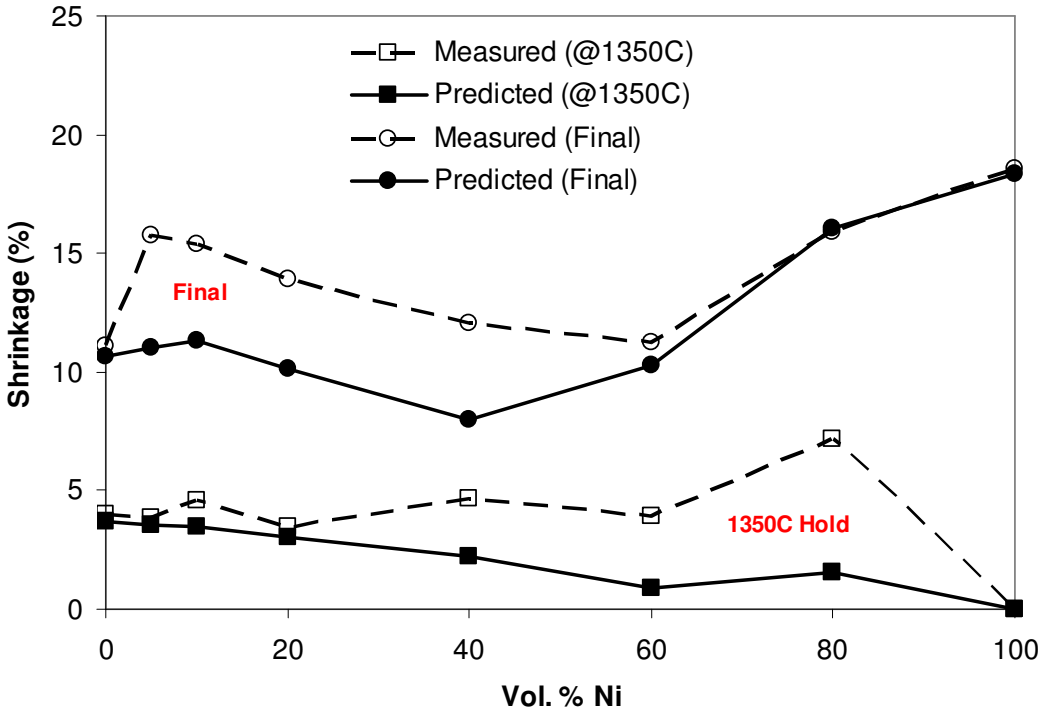

Figure 28: For TiO_2 powders, comparison of predicted and measured shrinkage at the final state and during the four hour hold at 1350˚C using the modified model.

The shrinkage curve for each composite layer will now be used to develop a model of the sintering process for graded metal-ceramic composites in the following section. This sintering model will enable the prediction of the effects of differential shrinkage on the evolution of stresses in gradient structures during the pressureless sintering process. Predicting the stress evolution is essential to understanding the benefits of using the TiO_2 nanopowder sintering aid. Additionally, these predictions will allow the design of appropriate gradient architectures for fabricating graded metal-ceramic composites with bulk molding technology.

CHAPTER 3: Modeling of Graded Metal-Ceramic Composites Including a Nanoparticle Sintering Aid

3.1 Model Description

Analyzing the sintering behavior of functionally graded metal-ceramic composites requires accurate prediction of the change in thermomechanical properties and shrinkage at varying temperature. Thermomechanical properties, including elastic modulus, Poisson's ratio, fatigue life, and fracture toughness, depend on the relative sintered density and microstructure [16]. Recently, a two-dimensional finite element analysis using a micromechanical thermal elastic-viscoplastic constitutive model has been developed to predict the stress distributions that arise from the evolution of differential shrinkage during the pressureless sintering process by Y.M. Shabana *et al.* [28]. This section describes the fundamental basis for this model.

3.1.1 Thermal Elastic-Viscoplastic Constitutive Model

As discussed in section 2.5.4, the shrinkage strain, $\varepsilon_s^T(t,T(t))$, is described by the Weibull power law time-dependent exponential equation in (13). For this thermal elastic-viscoplastic constitutive model, the diffusion-based shrinkage relation given in (13) is included with other diffusional processes, such as stress-dependent creep, into a total time-dependent thermoplastic strain vector, $\left[\varepsilon_p^T(t,\sigma_k(t),T(t))\right]_i$ for the matrix material, as follows:

$$\left[\varepsilon_p^T(t,\sigma_k(t),T(t))\right]_i = \varepsilon_s(t,T(t))\delta_i + \int_0^t \eta_{ik}^{-1}(T(\tau))\sigma_k(\tau)\,d\tau \qquad (i,\,k = 1,6) \qquad (27)$$

In (27), the stress vector $\sigma_k(t)$ = (σ_{11},σ_{22},σ_{33}, σ_{12},σ_{13},σ_{23}), δ_k=(1,1,1,0,0,0), and η_{ij} is the temperature- and porosity-dependent viscosity tensor determined from relations

described elsewhere [29-31]. Additionally, the time-dependent effects on η_{ij} are determined by the thermal profiles, *T(t)*, used for sintering.

If the metal undergoes elastoplastic deformation in the metal matrix composites, the equivalent shear modulus and Poisson's ratio, $\mu_0^{'}$ and $v_0^{'}$, must be introduced in the constitutive equation instead of μ_0 and v_0, as seen in (28). Similarly, when the metal particle undergoes elastic-viscoplastic deformation in the ceramic matrix composites, $\mu_1^{'}$ and $v_1^{'}$ must be introduced in the constitutive equation instead of μ_1 and v_1.

$$\mu_0^{'} = \frac{\mu_0}{1+3\dfrac{\mu_0}{H^{'}}}, \qquad v_0^{'} = \frac{v_0 + \dfrac{\mu_0}{H^{'}}(1+v_0)}{1+2\dfrac{\mu_0}{H^{'}}(1+v_0)} \tag{28}$$

In (28), $H^{'}$ is the work hardening ratio of the matrix. When the matrix undergoes elastic-viscoplastic deformation, the thermal elastic-viscoplastic constitutive equation can be written as [15,32]:

$$\begin{aligned} d\varepsilon_{kk} = & \\ & \frac{1}{3k_0(1-\bar{\nu})A_h}[\{(k_1-k_0)\bar{\nu}+k_0\}\{(1-\bar{\nu})(1-f_p-f_v)+f_v\}+(1-\bar{\nu})f_p k_0]d\sigma_{kk} \\ & \quad +\{\alpha_0 - \frac{k_1 f_p}{A_h}(\alpha_0-\alpha_1)\}3dT + d\left[\varepsilon_p^T\right]_{kk} \end{aligned} \tag{29}$$

$$\begin{aligned} d\varepsilon_{ij}^{'} = & \\ & \frac{1}{2\mu_0^{'}(1-\nu^*)A_d}[\{(\mu_1-\mu_0^{'})\nu^* + \mu_0^{'}\}\{(1-\nu^*)(1-f_p-f_v)+f_v\}+(1-\nu^*)f_p\mu_0^{'}]d\sigma_{ij}^{'} \\ & \quad + d\left[\varepsilon_p^T\right]_{ij} - \frac{\delta_{ij}}{3}d\left[\varepsilon_p^T\right]_{kk} \end{aligned} \tag{30}$$

Where:

$$A_h = (1 - f_p - f_v)\{k_0 + (k_1 - k_0)\bar{\nu}\} + f_p k_1$$
$$A_d = (1 - f_p - f_v)\{\mu_0' + (\mu_1 - \mu_0')\nu^*\} + f_p \mu_1 \quad \textbf{(31)}$$

In these equations, $d\varepsilon_{kk}$, $d\varepsilon_{ij}'$, $d\sigma_{kk}$ and $d\sigma_{ij}'$ are the hydrostatic and deviatoric components of incremental macroscopic strain and stress respectively. Also, $d\varepsilon_s$ is the incremental shrinkage, dT is the incremental temperature change, α_1 and α_0 are the coefficients of thermal expansion of the particle and the matrix, and f_p and f_v are the particle volume fraction and the void volume fraction in the incremental process. The bulk modulus and the shear modulus of the matrix and the particles, k_0, μ_0, k_1, and μ_1 respectively, are given by:

$$k_i = \frac{E_i}{3(1-2v_i)}, \quad \mu_i = \frac{E_i}{2(1+v_i)} \quad \text{(i=0,1)} \quad \textbf{(32)}$$

In (32), E_0, E_1, v_0 and v_1 are Young's modulus and Poisson's ratio of the matrix and the particles respectively. The Eshelby tensors for a spherical inclusion are as follows:

$$\bar{\nu} = \frac{1+v_0'}{3(1-v_0')} \quad \text{(Hydrostatic component)}$$
$$\nu^* = \frac{2(4-5v_0')}{15(1-v_0')} \quad \text{(Deviatoric component)} \quad \textbf{(33)}$$

The incremental stress of the matrix and the particle, $d\sigma^m = (d\sigma_{kk}^m, d\sigma_{ij}^{m'})$ and $d\sigma^p = (d\sigma_{kk}^p, d\sigma_{ij}^{p'})$ respectively, are given by:

$$d\sigma_{kk}^m = \frac{k_0 + (k_1 - k_0)\bar{\nu}}{A_h} d\sigma_{kk} + \frac{3k_0 k_1 f_p (1-\bar{\nu})(\alpha_1 - \alpha_0)}{A_h} 3dT + 3k_0 d\left[\varepsilon_p^T\right]_{kk} \quad \textbf{(34)}$$

$$d\sigma_{ij}^{m'} = \frac{\mu_0^{'} + (\mu_1 - \mu_0^{'})\nu^*}{A_d} d\sigma_{ij}^{'} + \mu_0^{'}\left\{ d\left[\varepsilon_p^T\right]_{ij} - \frac{\delta_{ij}}{3} d\left[\varepsilon_p^T\right]_{kk} \right\} \quad \textbf{(35)}$$

$$d\sigma_{kk}^{p} = \frac{k_1}{A_h} d\sigma_{kk} + \frac{3k_0 k_1 (1 - f_p - f_v)(\alpha_1 - \alpha_0)(1 - \bar{\nu})}{A_h} 3dT \quad \textbf{(36)}$$

$$d\sigma_{ij}^{p'} = \frac{\mu_1}{A_d} d\sigma_{ij}^{'} \quad \textbf{(37)}$$

If the matrix is in the elastic state, $\mu_0^{'}$ and $v_0^{'}$ in all these equations reduce to their elastic counterparts μ_0 and v_0 respectively. The finite element formulations for these constitutive equations have been described previously [32]. However, the model has been modified to include: (1) thermal strain and shrinkage in the initial strain vector and (2) porosity effects by treating the porosity as a third phase interacting with the fully dense composite.

3.1.2 Two-Dimensional Finite Element Analysis

Stresses caused by differential shrinkage during pressureless sintering are predicted by a two-dimensional finite element analysis based on the change in porosity and the corresponding evolution of thermal elastic-viscoplastic constitutive model. Cracking in gradient structures occur when the normal stress in the thickness direction, normalized by an ultimate strength power law function of the porosity, is greater than unity.

In the model, the Nickel undergoes elastic-viscoplastic deformation governed by the von Mises yield condition and the isotropic hardening, while the Alumina deformations are predominantly elastic. Considering half of the specimen due to symmetry, 2800 8-node isoparametric elements are used in the finite element analysis. The element size is refined near the interfaces between the layers, where the

smallest element size used is 75×10^{-6} m. Isothermal conditions (i.e., no thermal gradients) are assumed.

Necessary to predict the evolution of shrinkage stresses during sintering, this model accounts for the effects of evolving cohesive strength on the behavior of matrix phases. To accomplish this, the evolution of matrix thermomechanical properties in the constitutive model must be related to the total shrinkage or porosity. Mechanical properties, such as the modulus of elasticity and strength of the composite, evolve during sintering and typically vary with porosity according to a power law formulation [16]. Previous work determined this formulation for the evolution of mechanical properties could be refined by multiplying the power law by an exponential description for the evolution of interparticular cohesion. This cohesion of the matrix phase due to sintering, χ, is described as follows [33]:

$$\chi = \left(1 - e^{c(\bar{\rho}_i - \bar{\rho}_s)}\right) \tag{38}$$

In (38), $\bar{\rho}_i$ is the initial relative density, $\bar{\rho}_s$ is the sintered relative density, and c is a constant previously determined to be 12 for Nickel and Alumina.

3.2 Application of Model

The main reason for developing a model to predict shrinkage-induced residual stresses in gradient architectures is to determine geometries that can be used for the eventual fabrication of crack-free gradient structures. This section will describe the initial model verification accomplished by evaluating a crack-free rod produced experimentally and efforts to predict gradients for additional crack-free rod samples.

3.2.1 Initial Model Verification of a Crack-Free Rod Specimen

The first crack-free rod sample produced was the result of systematically varying layer thickness and qualitatively evaluating the sintered specimens. As layer thickness increased, the crack width diminished. Previous work has demonstrated that increasing the gradient thickness significantly reduces the peak residual stresses and plastic strains [15]. This crack-free ten-layer sample was fabricated with the following layer compositions: 0 (RC-HP), 5, 10, 20, 30, 40, 60, 70, 80, 100 vol.% Nickel. Approximately 61.5 mm tall in green compact form, all layers were of relatively equal thickness and contained the nanopowder TiO_2 sintering aid. The final sintered height was approximately 54 mm, as seen in Figure 29. The sintered layer thickness is presented in Table 16.

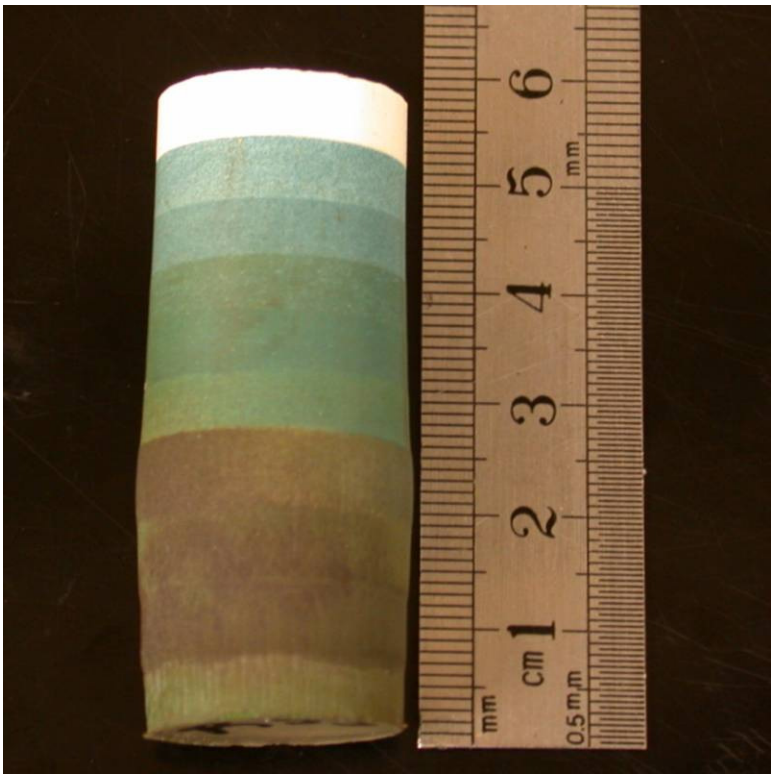

Figure 29: Crack-free rod sample (0,5,10,20,30,40,60,70,80,100 vol.% Ni layers) with substantial layer thickness and nanopowder TiO_2 in all appropriate layers.

Table 16: Sintered layer thickness (mm) of experimental crack-free rod sample with TiO_2.

Layer (vol.% Ni)	Sintered Layer Thickness (mm)
0 (RC-HP)	5.8
5	5.1
10	5.2
20	5.0
30	4.7
40	4.7
60	6.1
70	5.8
80	6.3
100	5.2
Total Height:	53.9

The successful fabrication of a crack-free rod enabled initial verification of model stress predictions. Since the rod geometry did not crack experimentally, the model should predict that all local stress levels fall below the critical failure stress. As seen in Figure 30, the normalized stress ratio does not exceed unity at any point and therefore the sample is not expected to crack. Peak stresses are observed at the 0-5 vol.% Nickel interface under tensile stress and the 80-100 vol.% Nickel interface under compressive stress. The normalized stress at the 40-60 vol.% Nickel interface, typically the failure location for most cracked samples, is relatively low at a normalized stress of approximately 0.4.

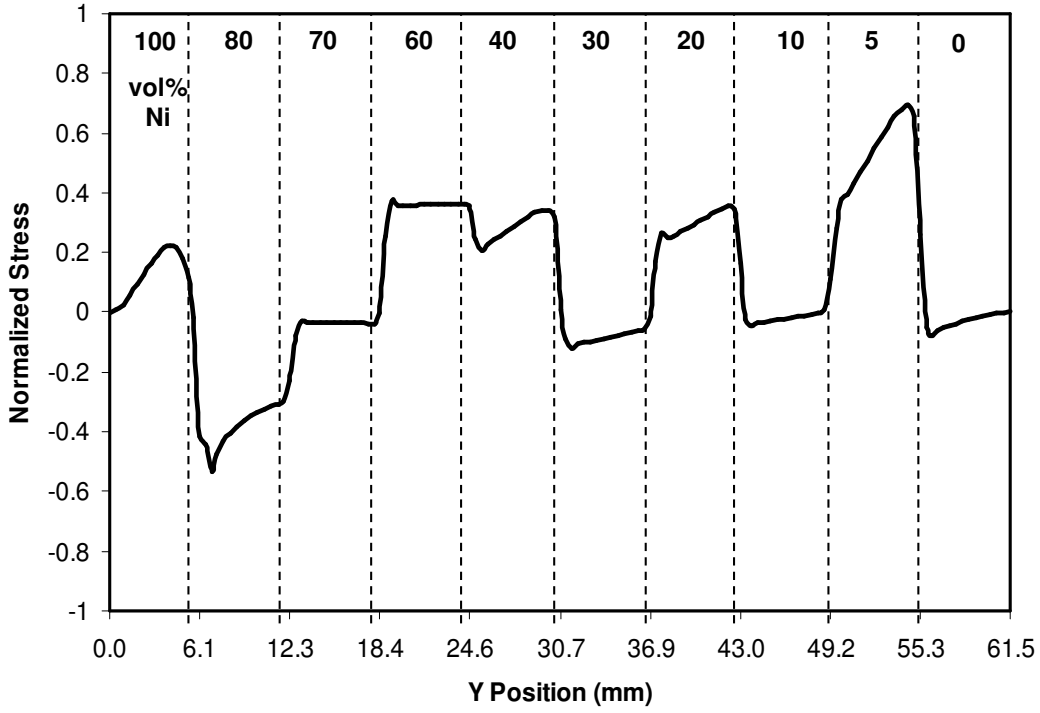

Figure 30: Predicted stress distribution at 1350˚C for the experimental crack-free rod. The stress does not exceed unity; therefore, the specimen is expected not to crack.

3.2.2 Gradient Architecture Prediction

Using the model, additional crack-free geometries can be predicted. The model can be used to optimally reduce layer thickness to predict specimens that require less material than the original crack-free specimen shown in Figure 29. By reducing layer thickness, powders will be conserved and specimen weight and thickness will be reduced. Considering a cylindrical rod specimen with the nanoparticle sintering aid, the model prediction for minimum green layer thickness is shown in Table 17. This green layer thickness is the layer thickness measured after cold pressing in the traditional die-based discrete layering process.

Table 17: Predicted minimum green layer thickness for crack-free rod sample fabrication.

Layer (vol.% Ni)	Green Thickness (mm)
0 (RC-HP)	2.8
5	2.8
10	2.8
20	2.8
30	2.8
40	6.2
60	6.2
70	6.2
80	6.2
100	2.8
Total Height:	41.6

For the model rod geometry in Table 17, the axial stresses predicted on the outer surface of the specimen, normalized by the predicted ultimate strength, with and without the nanopowder TiO_2 sintering aid can be seen in Figure 31. When the nanopowder TiO_2 is not used, cracking is predicted at the interface between the 60 and 70 vol.% Nickel layers. When the nanopowder TiO_2 is used, the stress ratio never exceeds unity and the specimen is not expected to crack. In fact, the maximum stress actually shifts to the interface between the 0 and 5 vol. % Nickel layers.

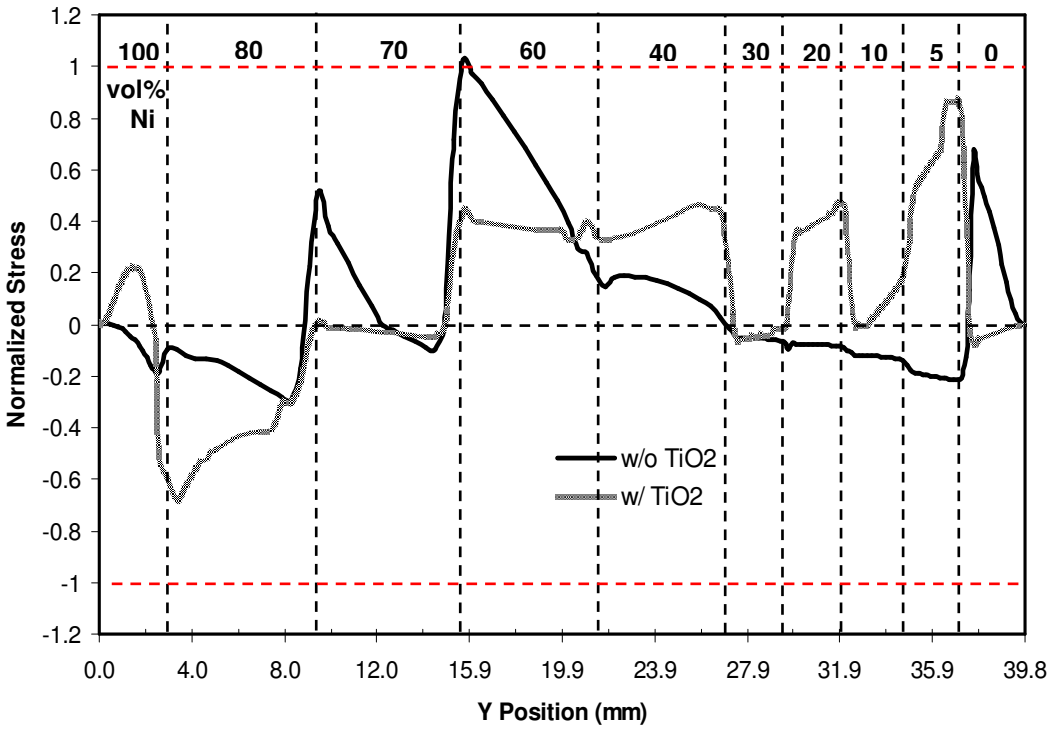

Figure 31: Predicted stress distributions at 1350˚C for the model rod geometry with and without TiO_2. The non-TiO_2 rod is expected to crack, while the TiO_2 rod is not.

3.3 Fabrication of Model Crack-Free Rod Samples

Using the minimum green layer thickness predicted by the model in Table 17, a cylindrical rod specimen was made from powders containing TiO_2 and a second rod sample was made from traditional powders lacking the TiO_2 sintering aid. Careful consideration of green layer thickness had to be made due to the poor tolerances experienced when layering powders within the die by hand. After experimenting with the various powder mass quantities, the minimum powder masses required to achieve the desired layer thickness were determined, as presented in Table 18. These masses ensured that with careful and deliberate fabrication techniques, layer thickness would not drop below the required minimum at any point around the circumference of the specimen. In addition, after substantial fabrication trial and error it was determined that the 100 vol.% Nickel layer was not required to meet the 2.8 mm layer

thickness minimum. This fact is reflected in the eventual fabrication of a crack-free specimen. For this reason, the powder mass reported in Table 18 for 100 vol.% Nickel was the mass quantity used in fabrication, not the mass quantity required for 2.8 mm green layer thickness.

Table 18: Powder mass quantities used to fabricate model rod specimens.

Layer (vol.% Ni)	**Required Powder Mass (g)**
0 (RC-HP)	3.2
5	3.9
10	4.1
20	4.7
30	5.2
40	12.3
60	12.3
70	12.9
80	14.7
100	3.5
Total Mass:	76.8

With required powder mass quantities determined, the two cylindrical rod specimens were fabricated as normal. The resultant specimens are seen in Figure 32. The rod containing the TiO_2 sintering aid displays no outer signs of cracking. The layer transitions are relatively smooth and there are no unexpected bulges or ridges. However, the rod made from powders without the TiO_2 sintering aid cracked at the 40-60 vol.% Nickel interface, which is near the predicted failure interface at 60-70 vol.% Nickel. While the crack width is extremely small at approximately 140 μm, there is a "step-down" ridge effect at the interface, whereby the edge of the 40 vol.% Nickel layer is noticeably raised above the 60 vol.% Nickel layer. A micrograph of the crack has been produced in Figure 33. The green and sintered layer thickness

measured down a similar line along the circumference for both specimens is presented in Table 19.

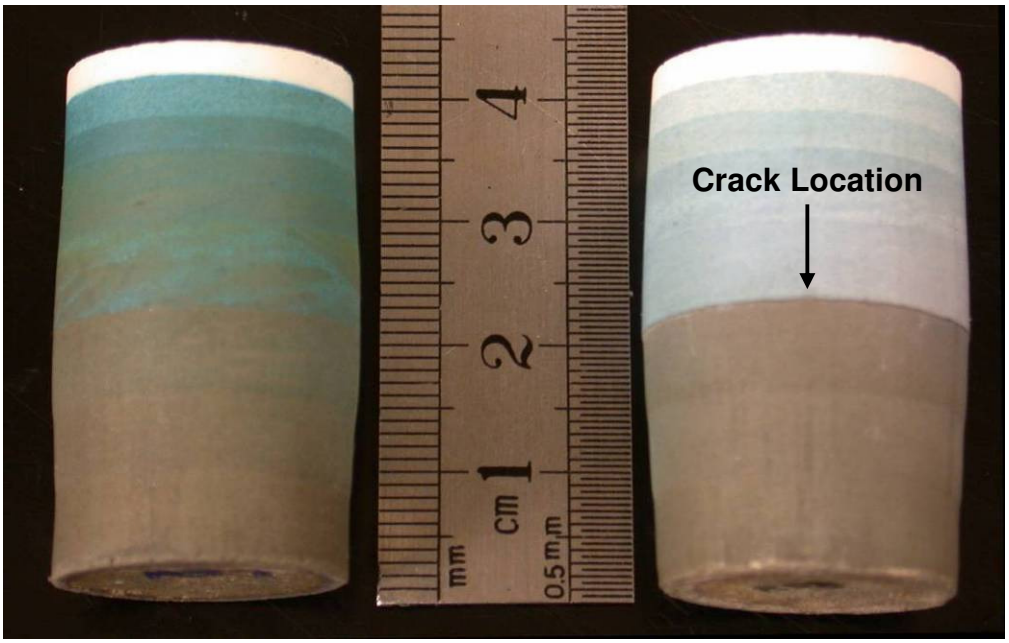

Figure 32: Model rod specimens: crack-free rod (left) with TiO_2, cracked rod (right) without TiO_2.

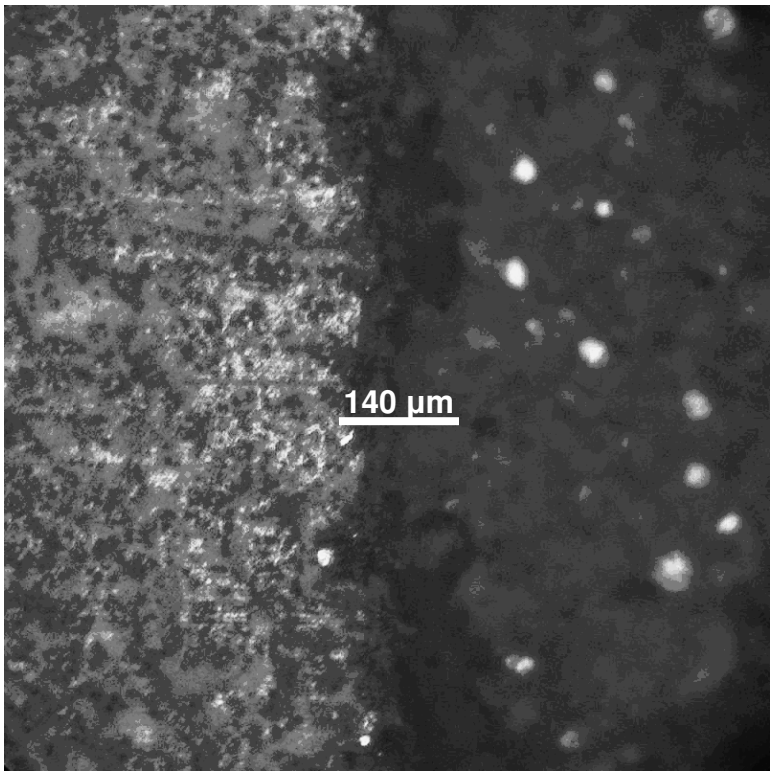

Figure 33: Crack at the 40-60 vol.% Nickel interface of the non-TiO_2 model rod specimen.

Table 19: Green and sintered layer thickness of model-based rod specimens.

	Non-TiO_2 Rod		TiO_2 Rod	
Layer (vol.% Ni)	**Green Thickness (mm)**	**Sintered Thickness (mm)**	**Green Thickness (mm)**	**Sintered Thickness (mm)**
0 (RC-HP)	3.1	2.9	3.3	2.8
5	3.2	2.8	2.8	2.4
10	3.2	2.9	3.0	2.6
20	3.1	2.8	3.4	2.8
30	2.8	2.4	2.9	2.5
40	6.2	5.6	7.0	6.4
60	7.2	6.7	6.5	6.3
70	6.7	5.7	6.6	6.2
80	6.6	5.6	6.2	5.1
100	1.0	0.6	1.0	0.7
Total Height:	43.1	38.0	42.7	37.8

3.3.1 Microhardness of a Crack-Free Rod Sample

Following the fabrication of a model crack-free cylindrical rod specimen using the nanoparticle sintering aid, the microhardness profile was characterized using the Vickers microhardness tester described previously. Unlike the cracked TiO_2 rod previously tested in section 2.5.3, the new structure featured pure RC-HP Alumina instead of bimodal Alumina and a non-constant layer thickness distribution. The new structure also included previously unused 30 and 70 vol.% Nickel layers. Despite these differences, the crack-free rod displays a very similar microhardness profile to the cracked rod. The microhardness profile for the crack-free rod is shown in Figure 34.

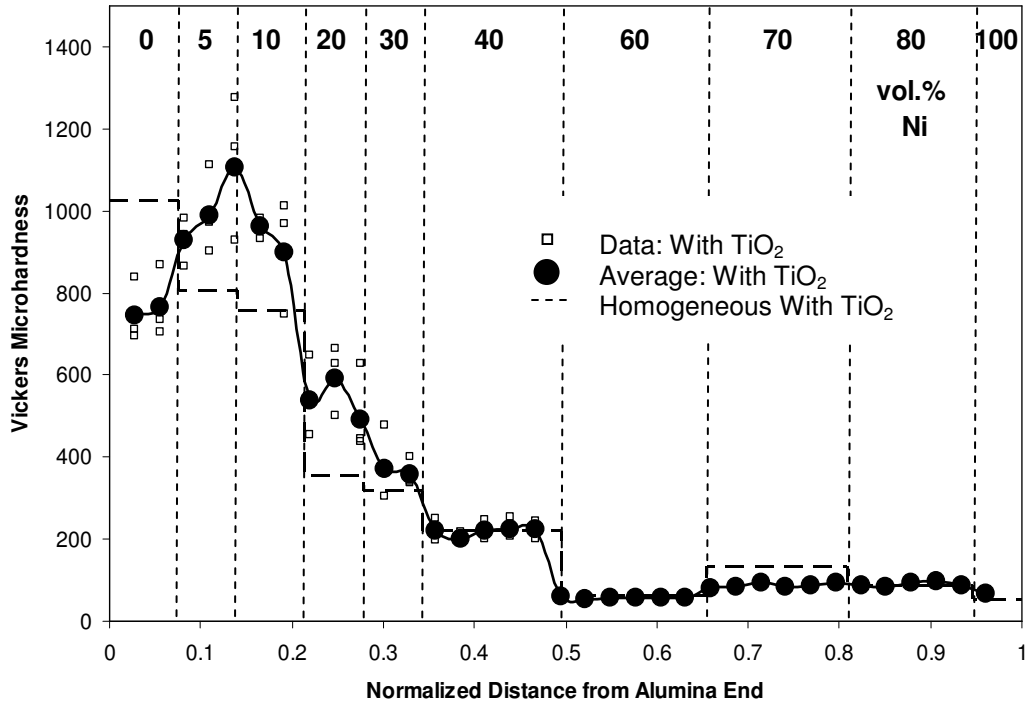

Figure 34: Vickers microhardness profile by distance along crack-free rod specimen gradient.

Reviewing the results, the pure Alumina layer is still under tensile stress and therefore the microhardness is still lower than the stress-free homogeneous disk results. However, the microhardness of the pure RC-HP Alumina is higher than the bimodal Alumina used previously. The only other difference from the cracked TiO_2 rod is the inclusion of the 30 and 70 vol.% layers, which appear to be in agreement with the homogeneous measurements. The crack-free and cracked TiO_2 rods display nearly identical profile trends in the remaining 5, 10, 20, 40, 60, and 100 vol.% Nickel layers. Averages by layer composition are presented in Table 20. Considering microstructural variation due to the presence of particle agglomerates, measured microhardness for matching compositions are almost identical. From these results, it is concluded that the inclusion of the new 30 and 70 vol.% Nickel layers

have little effect on the surrounding microhardness profile. The crack in the 40-60 vol.% Nickel interface of the rod tested in section 2.5.3 does not seem to alter surrounding microhardness either.

Table 20: Average Vickers microhardness (HV) by layer for a cracked rod versus a crack-free rod, both containing TiO_2.

	TiO_2 Cylindrical Rods		
Layer (vol.% Ni)	**Cracked**	**Crack-Free**	**Increase (%)**
0 (Bimodal / Unimodal)	582.23	754.54	29.6
5	936.41	1008.06	7.7
10	822.88	930.48	13.1
20	540.87	540.65	0.0
30	–	364.40	–
40	207.19	217.85	5.1
60	58.98	56.48	-4.2
70	–	87.01	–
80	90.96	90.22	-0.8
100	54.43	59.04	8.5

3.4 Model Verification by Profile Evaluation

The fabrication of a crack-free rod sample with the TiO_2 sintering aid using the predicted minimum green layer thicknesses has demonstrated the ability of the model to predict crack-free geometries. The success of the model in this aspect is evaluated qualitatively by comparing predicted peak stresses with careful inspection of sintered experimental specimens. However, also of interest is the ability of the model to predict accurate sintered gradient shrinkage results. This is characterized by comparing the predicted sintered profile with measurements taken from experimental specimens. As a result, this profile characterization enables quantitative verification of the model.

The first crack-free rod, shown in Figure 29, was established experimentally and provided the initial basis for model stress verification. This sample was again used to verify model profile predictions. To compare the predicted results with experimental measurements, the true sintered profile was digitized and overlaid on the theoretical profile generated by the model in Figure 35. The theoretical and experimental profiles tend to correlate well in general shape, but shrinkage is over predicted for the 40, 60, 70, 80, and 100 vol.% Nickel layers by the model. According to previous work [28], the reduced distortion measured experimentally is possibly due to gradient imperfections that altered the stress distribution or the material may be yielding or creeping more than had been predicted by the thermal elastic-viscoplastic constitutive model relations.

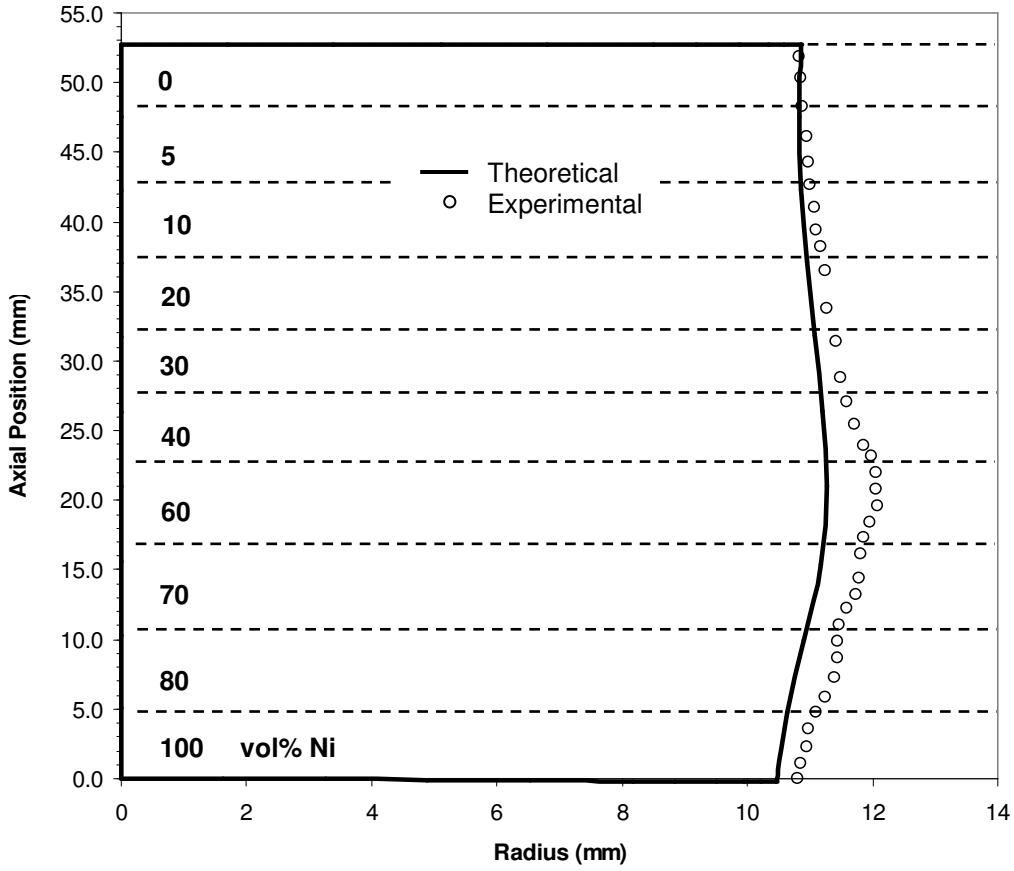

Figure 35: Theoretical and measured sintered shape profiles of experimental crack-free rod sample containing TiO_2.

CHAPTER 4: Fabrication of Graded Metal-Ceramic Composites Using Bulk Molding Technology

4.1 Bulk Manufacturing Methods

The die-based discrete layering approach used elsewhere in this research provides a simple means for creating graded metal-ceramic composites with two-dimensional geometric complexity using powder processing techniques. In review, this method consists of the following basic steps:

1. Prepare distinct composite powder compositions by ball-mixing
2. Layer required powders in steel compaction die
3. Press powders in die into a green compact
4. Pressureless sinter green compact into final composite structure

In the laboratory environment, the majority of fabrication time is spent on the first and last steps of this procedure. This is due to long powder mixing times, binder drying times, and the furnace sintering schedule. Alternatively, the processing of graded metal-ceramic composites in bulk quantities can be accomplished by: (1) scaling up similar processes and (2) employing more conventional bulk manufacturing methods to decrease fabrication time.

For the bulk manufacturing of powder-processed components, the fabrication procedure can be scaled up by generating large quantities of powders in commercial-scale mixers and sintering large quantities of powder-processed components in commercial-scale furnaces. Adapting bulk molding technology to the process, large molds with many cavities can be used in place of individual compaction dies. Bulk molding techniques can quickly produce green compacts in tens to hundreds of units.

This section will describe the initial application of these bulk molding techniques for graded metal-ceramic composite structures.

4.1.1 Bulk Molding Technology

Bulk molding technology often utilizes two-dimensional molds that are machined or cast with the desired component geometry. Molds are usually machined from steel or aluminum, but can also be cast from polymers or reinforced concrete when the molding operation is under low pressure [34]. Mold size depends on the component dimensions and the number of desired components.

In the case of powder, slurry, or other mixture processing, the mold cavities are filled with material and then shaken by a vibrator to settle the constituents. The challenge with this method is to design the molds so that the vibration provides a single primary frequency response that rapidly but gently settles the material constituents. Desired frequencies often range from tens to hundreds of Hertz and vary greatly depending on the number and size of the cavities as well as the mold material. For this research, bulk molding techniques employed by the concrete products industry have inspired the development of a laboratory-scale processing assembly to investigate the bulk manufacturing of graded metal-ceramic composite structures. Decorative concrete blocks fabricated using similar bulk molding technology can be seen in Figure 36. For these concrete blocks, mold processing time on a vibrating press typically ranges between 10 and 15 seconds [35].

Figure 36: Precast decorative concrete paving stones [36].

4.1.2 Setup of Laboratory-Scale Fabrication Assembly

A steel 1/10 scale mold, of similar design to molds employed by the concrete products industry, was machined for use in the experimental setup and eventual fabrication of graded structures. As seen in Figure 37, the mold consists of nine hexagonal mold cavities. Each cavity presents a cross-sectional molding area of approximately 10.13 cm^2. To allow the mold to be fixed in place, two small clamping rails extend out the ends of the mold.

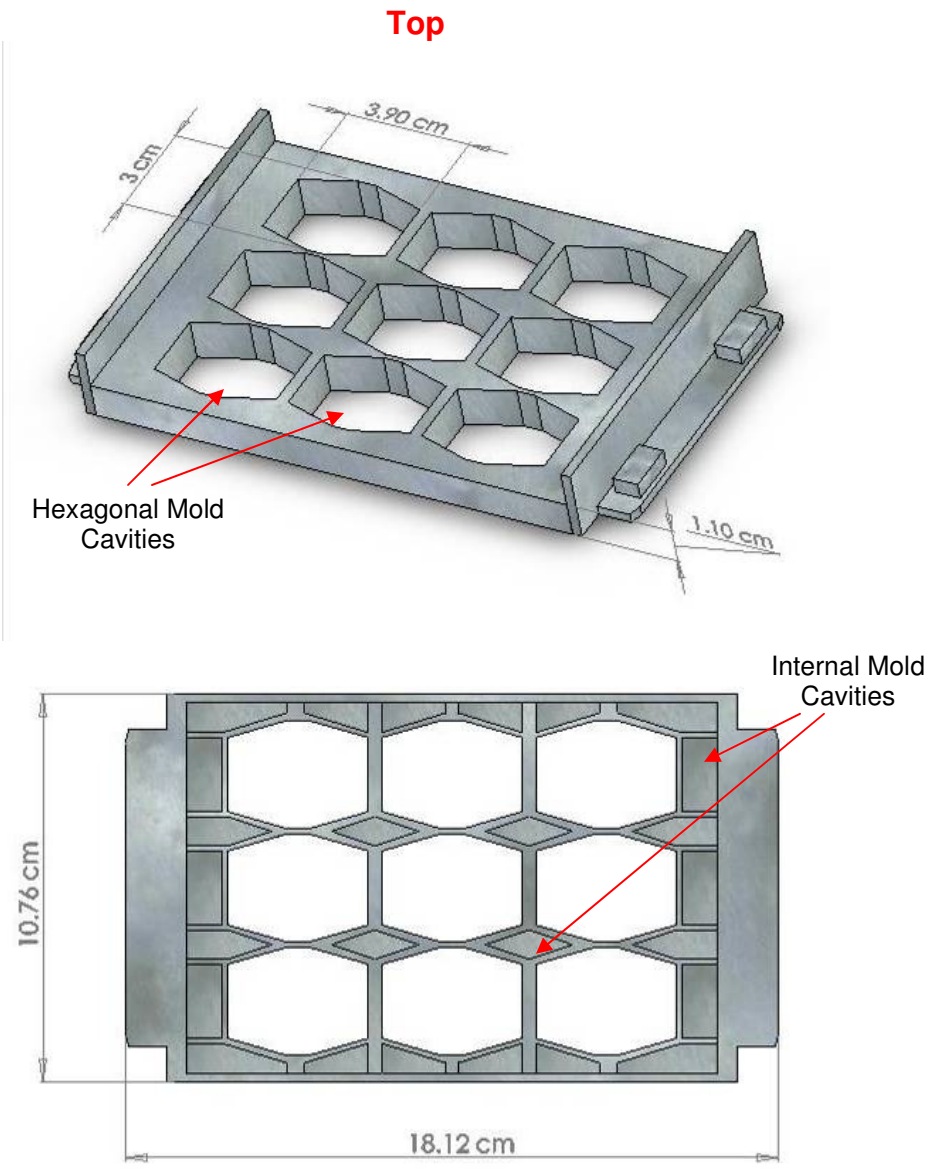

Figure 37: 1/10 scale steel mold with nine hexagonal mold cavities. The internal mold cavities machined into the bottom of the mold are not intended for materials processing.

The fabrication assembly can be broken down into four additional components: (1) bottom plate, (2) tamper plate, (3) slapper plate, and (4) vibration plate. The bottom plate anchors to the bottom of the mold and keeps the material from falling through the empty mold cavities. The tamper plate, as seen in Figure 38,

consists of nine machined hexagonal reliefs that fit into the mold cavities to keep material from flying out the top. The slapper plate, free to translate up and down, bounces between the bottom plate and vibration plate. Finally, a portable electric paint shaker was modified to provide the vibration plate response. This experimental testing configuration can be seen in Figure 39 and Figure 40.

Figure 38: Tamper plate with nine machined hexagonal reliefs. The reliefs insert into the top of the mold cavities to prevent material from flying out during processing.

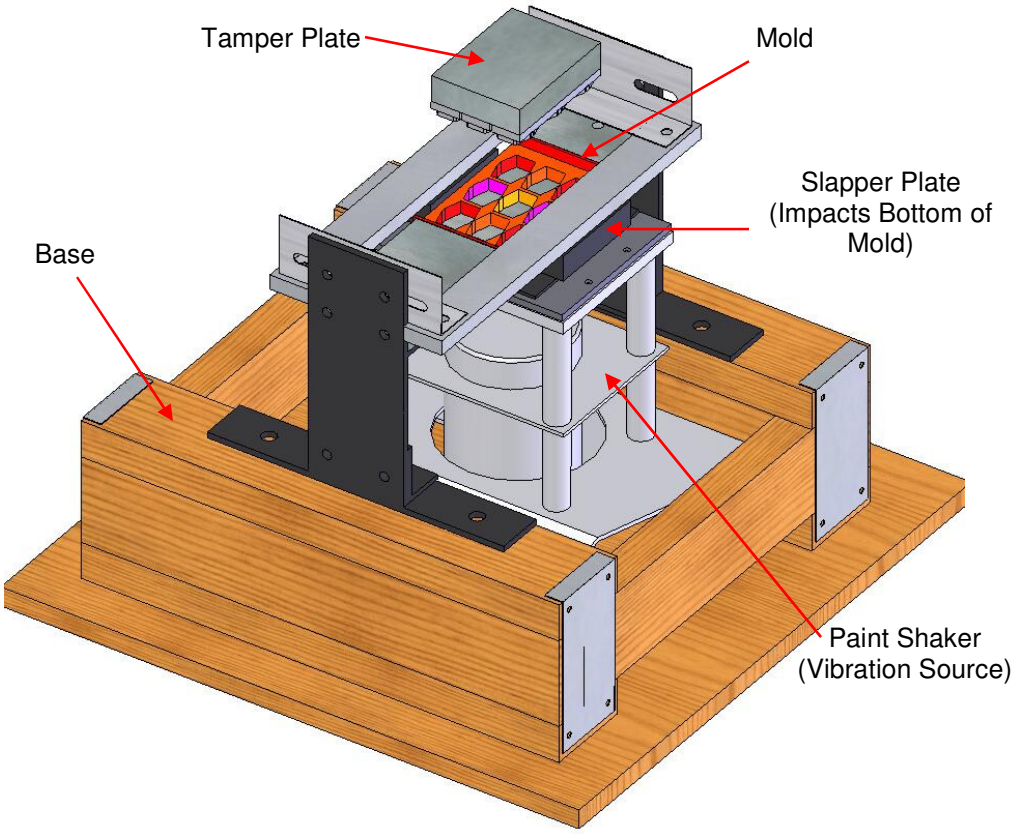

Figure 39: Entire laboratory-scale molding assembly with tamper plate held out of position to show mold location.

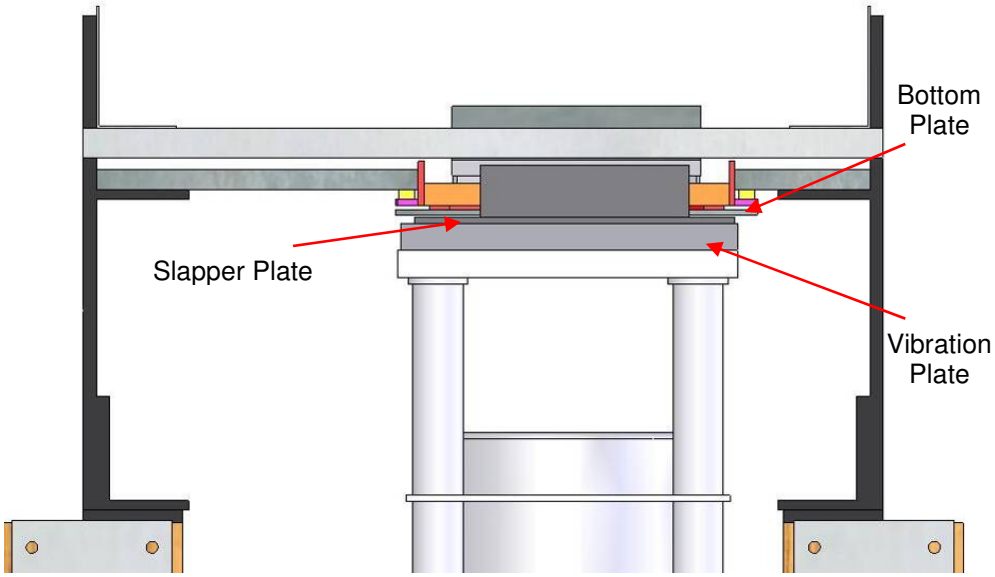

Figure 40: Side-view of laboratory-scale molding assembly with tamper plate in position.

4.2 Vibrational Analysis of Mold Performance

Vibrational response was characterized by mounting strain gages to the top surface of the mold using strain gage adhesive. Each gage was wired to a portable strain indicator quarter bridge then channeled to an oscilloscope. Computational finite element analysis identified the critical locations on the mold. As seen in Figure 41, three strain gages were attached and aligned according to these computational results. The complete laboratory-scale processing system with instrumentation can be seen in Figure 42.

Signal processing techniques were used to analyze the resultant strain data. Under various testing conditions, the strains from all three gages were recorded over a short interval. The discrete Fourier transform (DFT) is often used to analyze frequencies in sampled signals, which can be computed efficiently using a fast Fourier transform (FFT) algorithm. This FFT was used to quantify the dynamic modal response of the mold.

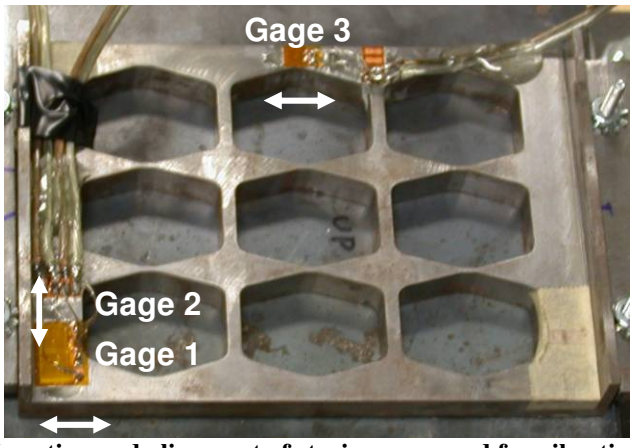

Figure 41: Location and alignment of strain gages used for vibrational analysis.

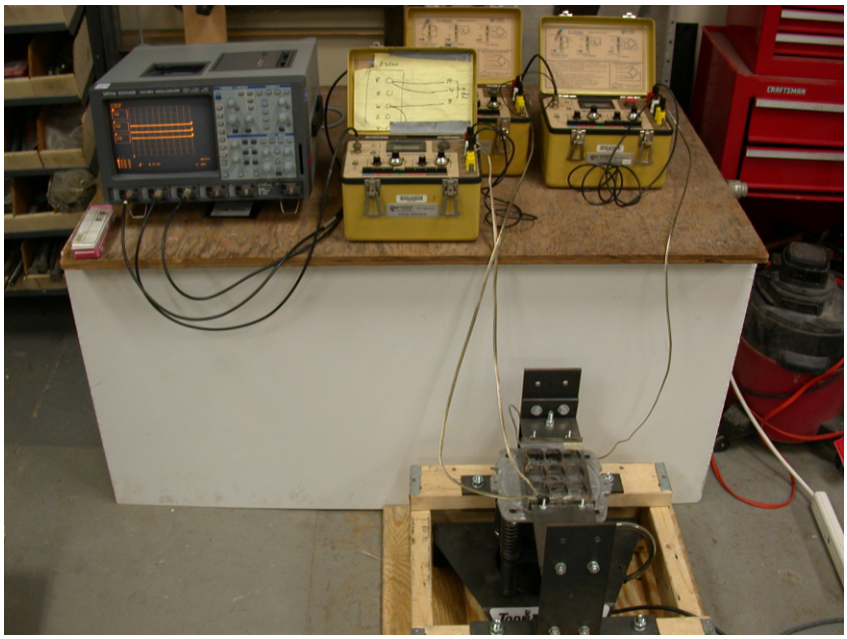

Figure 42: Complete laboratory-scale processing system with instrumentation.

4.2.1 Empty Mold Performance

To identify the vibrational characteristics of the laboratory-scale steel mold, tests were conducted on the empty mold under three different conditions:

1. Free Vibration (modal response)
    a. Mold secured to the frame (constrained)
    b. Mold unsecured (unconstrained)
2. Gap Test (simulation of actual impact loading conditions)
    a. Fixed gap between the slapper plate and the bottom of the mold
3. Preload Test (low frequency response)
    a. Fixed initial compression of the spring-loaded vibrator generates a preload on the bottom of the mold

The mold was bolted to the steel frame in one of two positions: above the frame mounts for the gap test or below the mounts to compress the vibrator springs for the

preload test. Tightening the mold to the frame generates the following strain in each position:

Gap Test (Mold secured to top of frame mounts)

- Gage 1: +6.312 με
- Gage 2: -14.353 με
- Gage 3: -31.728 με

Preload Test (Mold secured to bottom of frame mounts)

- Gage 1: +6.546 με
- Gage 2: -17.665 με
- Gage 3: -39.282 με

In the preload test, the mounted mold is brought in contact with the spring-loaded vibrator. The upward spring force generated on the bottom of the mold counteracts the initial clamping force, resulting in the following final state of initial strain before testing:

Preload Test (Mold secured with vibrator spring compression)

- Gage 1: +3.740 με
- Gage 2: -14.132 με
- Gage 3: -24.390 με

For the testing of the empty mold, the mold was isolated from the fabrication components by removing the tamper plate and bottom plate from the assembly. The vibration plate and slapper plate remain in place to allow characterization of the vibrational response. Before testing results could be obtained, baseline noise was identified in Figure 43a for removal from the test data. Data was exponentially smoothed using a factor of 0.01, which was applied once before removal and twice after. The 60 Hz sinusoidal response is plotted for comparison. Baseline removal from the signal obtained after testing can be seen in Figure 43b. These results indicate that the baseline noise data can be removed to improve the quality of the signal.

The first testing condition was the free vibration response of the mold. To characterize performance, the mold was subjected to a single impact when secured to the frame and another single impact when unsecured. For the unsecured test, the mold was allowed to rest on the frame mounts. Test results for changing the constraint condition on the free vibration response of the mold can be seen in Figure 44. As expected, securing the mold to the frame significantly dampens the free vibration response to the single impact.

After securing the mold to the frame in the appropriate position, experimental data was obtained for the preload and gap tests after the strain gages had been re-zeroed. Results from the gap test can be seen in Figure 45 and results from the preload test can be seen in Figure 46. The initial strain generated by securing the mold is on the same order of magnitude as the strains generated during both of these tests. The gap tests have a 134 Hz signal and contributions from multiples of 10 Hz, similar to frequencies seen in the preload tests. The signal increases as the gap magnitude decreases. For the preload tests, there is a strong signal at a frequency of 20 Hz, which is the frequency of the vibrator during steady-state operation. At the end of the test, the vibrator becomes unbalanced as it settles to a stop. For this unique case, the signal increases strongly and shifts towards 15 Hz.

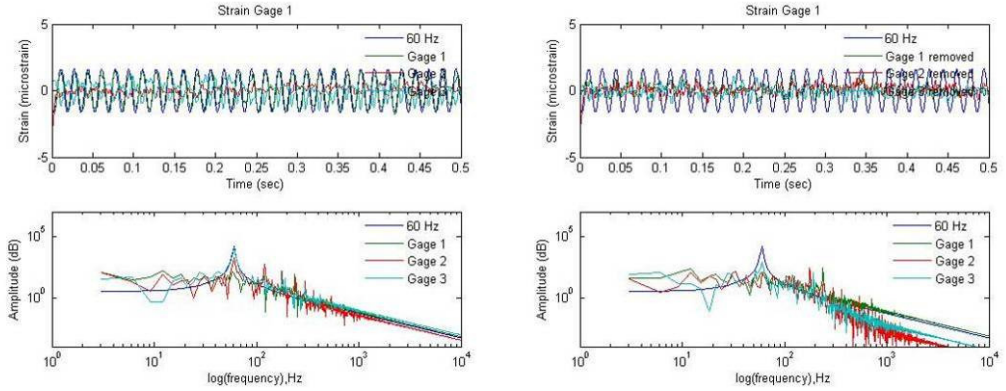

(a) (b)

Figure 43: Baseline noise (a) before removal and (b) after removal.

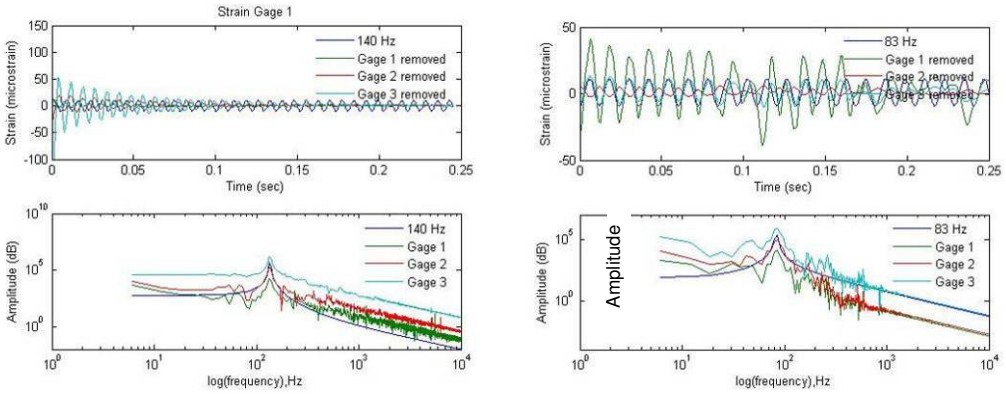

(a) (b)

Figure 44: Free vibration (a) with clamping and (b) without clamping.

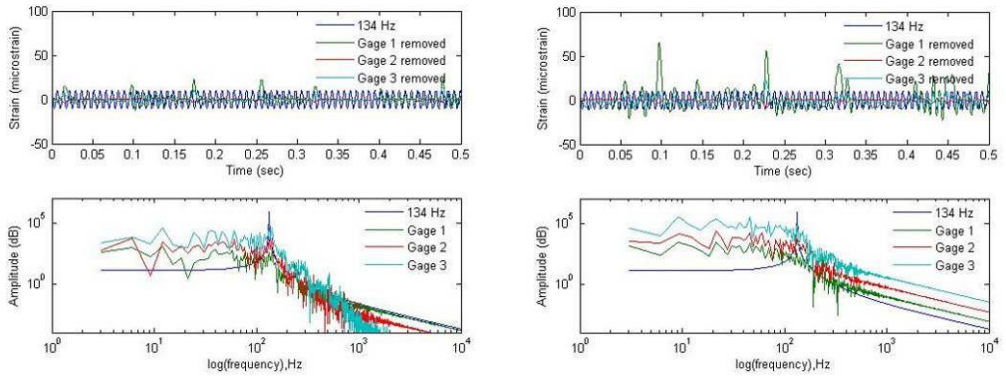

(a) (b)

Figure 45: Gap test at (a) 70 mil and (b) 15 mil gap.

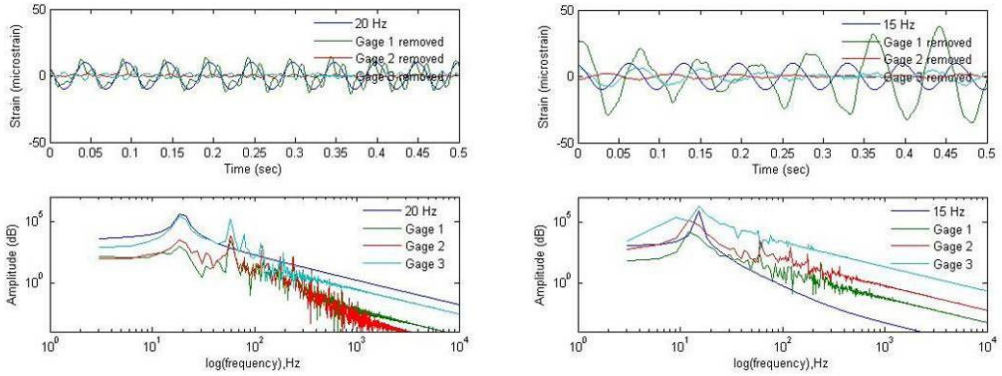

(a) (b)

Figure 46: Preload test at (a) steady-state and (b) unbalanced end of test.

4.2.2 Carbon Nanotube Reinforcement of Internal Mold Cavities

While conventional steel is desirable to control the primary vibrational response of the mold, it is possible to incorporate advanced composite materials into the mold to fine tune the response. Recent advances made in polymer nanocomposite technology have been successfully integrated into molds using inexpensive commercial carbon nanofibers (CNF).

Of particular importance in engineering, the integration of composite materials into the molds must be done in a manner that ensures reliability under the tremendous inertial forces that these molds will be subjected to. Polymer nanocomposites present unique integration technologies, including the use of complex surface geometries and tailoring of the nanocomposite microstructure to increase the interfacial strength between the polymer nanocomposite and the mold. In order to determine design criteria, the integration of these materials will also require the development of the relationships between properties that satisfy the functional needs and cost concerns of the molds.

For this research, a standard 15 wt.% CNF-reinforced epoxy was injected into the as-machined surface of the internal mold cavities, as seen in Figure 47.

Comparing test results between filled and unfilled internal cavities, results confirm the ability to fine tune the dampening and frequency response of the mold through the engineering of a nanostructured material [37]. A theoretical response for a 20 Hz impact is also included in Figure 47 for comparison. The strong peak associated with the impact near 20 Hz is present in both cases; however, the presence of the polymer nanocomposite dampens the response of the mold and reduces the frequency from 133 Hz to 113 Hz, which is consistent with a change in the natural frequency of the mold. Thus, it was concluded from these results that the adhesion and CNF loading of the polymer nanocomposite was adequate for altering the performance of the steel mold.

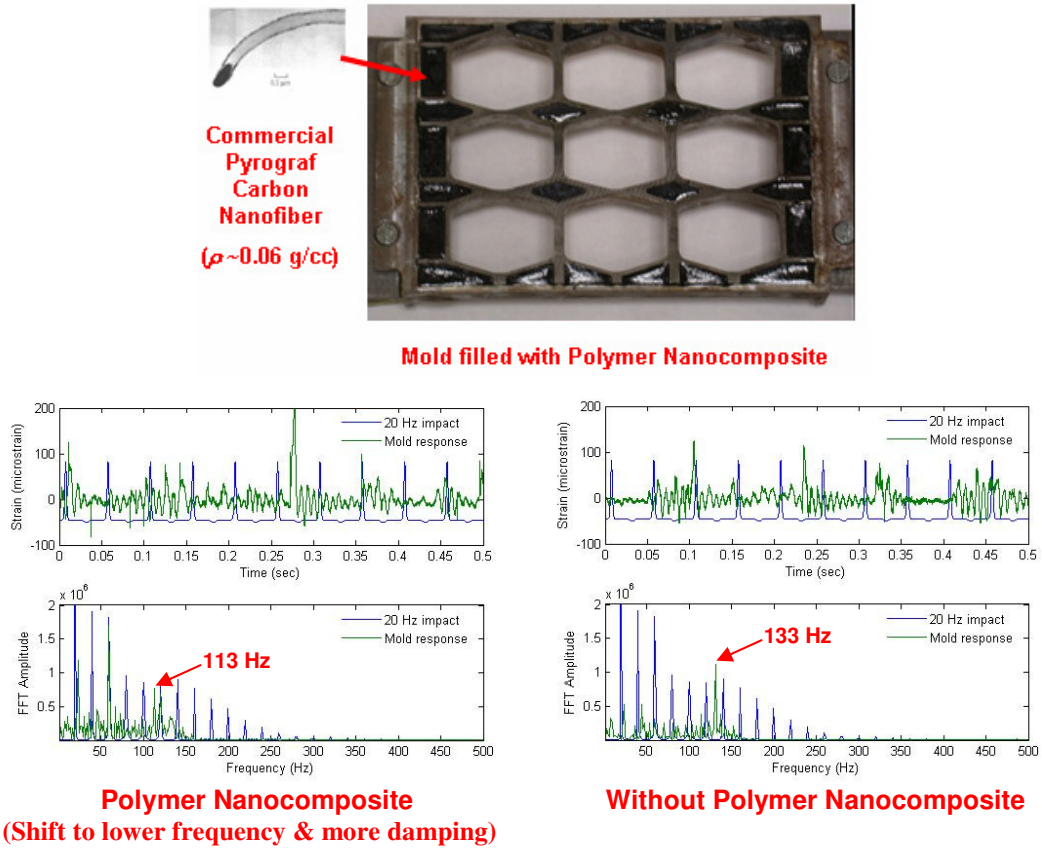

Figure 47: Polymer nanocomposites integrated into mold with corresponding test results indicating a lower frequency response above 100 Hz with more damping.

4.2.3 Filled Cavity Mold Performance

With the basic vibrational response of the mold characterized, it was possible to proceed with a study of the mold performance when the hexagonal mold cavities were filled with powdered material. Unlike the previous empty mold tests, the full molding assembly was used, including the bottom plate and tamper plate described previously. These additional components were required to prevent material from escaping the mold during vibrational processing. The assembly configuration and test data for the mold can be seen in Figure 48 and Figure 49 respectively. In Figure 49, the theoretical response for a 20 Hz impact is also included. For the theoretical impact, peaks are noted in the FFT spectrum for every multiple of 20 Hz, which decay with increasing frequency. The mold response has a similar profile, except that there is an absence of peaks at certain multiples and an additional strong peak at 28 Hz. In particular, strong peaks are present at 60 Hz, 180 Hz, 300 Hz and 480 Hz.

Comparing these results with the previous analysis of unfilled cavities, it appears that there is a strong lower frequency response from the presence of the attached bottom plate. Bolted to the bottom of the mold, the bottom plate transmits the impact from the slapper plate to the mold. Additionally, the strong response above 100 Hz, due to the natural frequency response of the mold, was not present when the cavities were filled. The presence of powdered material in the mold cavities also substantially dampens the response. Thus, it can be concluded that the effects on mold response due to filled hexagonal cavities are similar to those observed when the internal mold cavities were filled with polymer nanocomposite. However, the

frequency shift and the damping effects experienced by the filled hexagonal cavities are substantially greater.

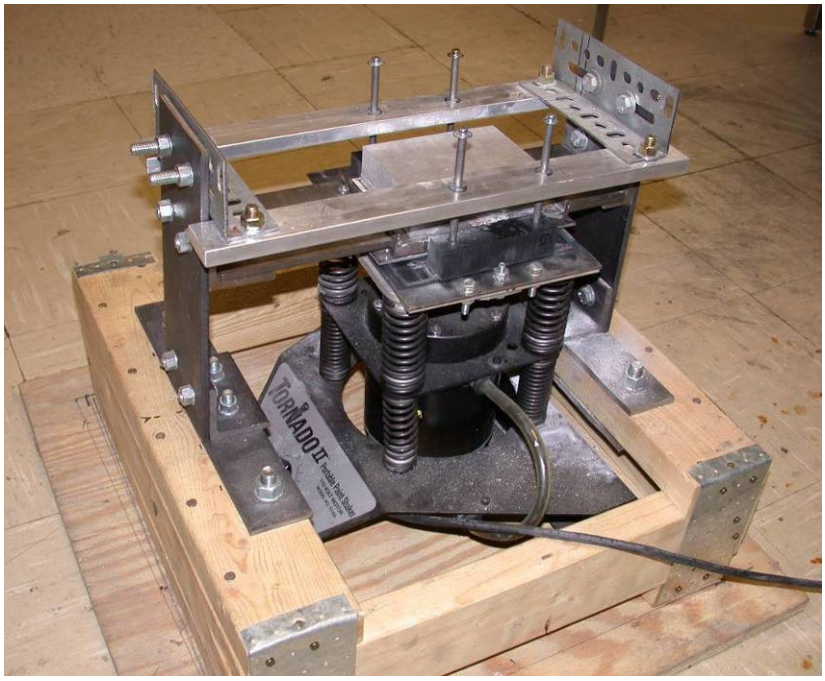

Figure 48: Full laboratory-scale mold processing assembly with all components in place.

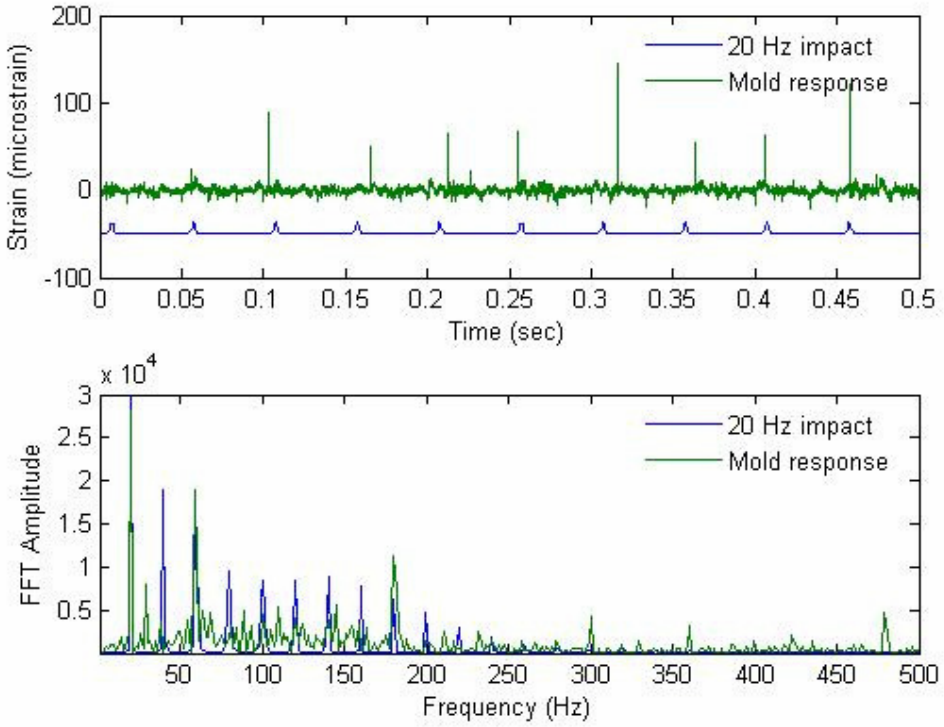

Figure 49: Mold response with mold cavities filled with powdered material.

4.3 Bulk Processing of Graded Metal-Ceramic Composites

The discrete layering powder processing technique was adapted to process multiple graded specimens in the steel mold. First, the bottom plate is bolted to the mold and the entire mold is sprayed with zinc stearate dry powder mold release. The appropriate composite powder is then poured into an empty mold cavity. Lowering a hexagonal mold plug into the cavity levels the loose powder within the cavity. The plug is allowed to rest on the powder surface, but no additional pressure is applied. The plug is then removed. Another powder composition can then be poured into the cavity and leveled with the plug. This process repeats until all required compositions are layered within the cavity. This procedure applies to all nine hexagonal cavities of the steel mold.

Following the addition of powders to the mold, the mold is ready for processing on the vibration plate. The mold is fixed to the steel supports that place the mold over top of the vibration plate. With the slapper plate in position between the vibration plate and bottom plate, the processing is ready to begin. The paint shaker is then turned on, which provides the oscillatory motion that causes the slapper plate to impact the bottom plate. As the slapper plate impacts the bottom plate, the powders within the cavity are shifted and nominally mixed. The paint shaker is typically run for one minute, the results of which can be seen in Figure 50.

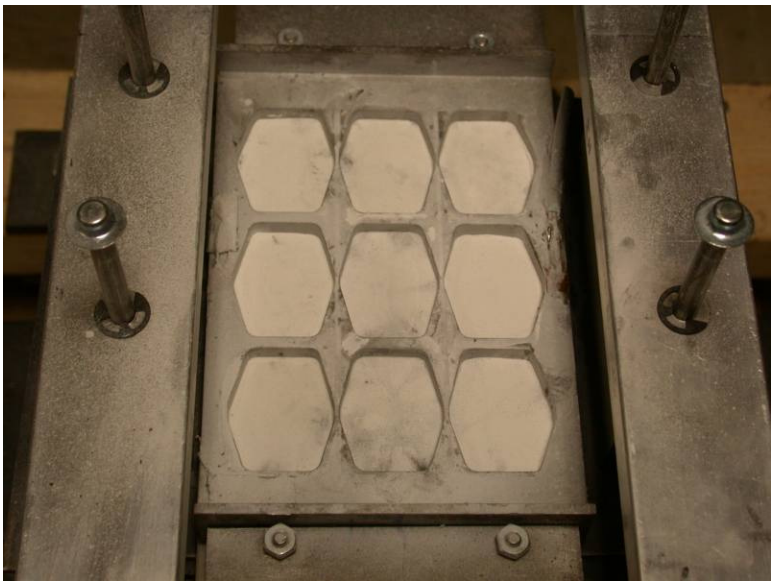

Figure 50: Powder samples after one-minute of vibrational processing.

When processing is deemed complete, the mold is removed from the steel supports and transferred to a cold press. Using the hexagonal plug, the loose powder is compacted to 88 MPa one cavity at a time, as seen in Figure 51. To complete the process, the bottom plate is removed and the green compacts are pressed out of the mold. As seen in Figure 52, these green compacts are then ready for sintering in the furnace using the standard sintering schedule described previously.

Figure 51: Cold pressing of hexagonal powder samples.

Figure 52: Processed and pressed green compacts ready for sintering.

The quality of the sintered specimens depends on the level of mixing. A high degree of vibrator-induced mixing will remove any discrete layer boundaries. This will restrict shrinkage because the interface is now a chaotically mixed interface. Figure 53 displays a four layer modular hexagonal sample (0, 40, 60, 100 vol.% Nickel) that displays minimal cracking due to heavy mixing.

Figure 53: Four-layer sintered hexagonal sample

4.3.1 Related Work

Similar work was conducted using the cylindrical rod die. Powders were traditionally layered one-by-one within the die. However, before application of the cold press, the powders within the die were shaken. This was done by raising the die ram approximately one inch above the top surface of the powders to allow room for mixing, then rotating the entire die and ram assembly end-over-end several times. This provided some degree of chaotic mixing within the die chamber. The cold press was then applied and the sample sintered as normal.

The result of the chaotic mixing was that the final shrinkage was severally restricted. In some cases, depending on the randomness of mixing, cracking was not observed in the specimens. Control samples, of the same mass constituents, that were

not shaken were also sintered. These samples experienced severe cracking that resulted in complete debonding. Figure 54 shows equivalent composition samples where one specimen is shaken and one is not. The traditionally layered sample has completely debonded at several interfaces while the mixed sample is crack-free. The composition for these particular samples, in order of application, was pure small Alumina (RC-HP), pure large Alumina (Gilox-63), pure large Nickel (HDNP), and pure small Nickel (123). Figure presents the micrograph cross section of the shaken rod sample.

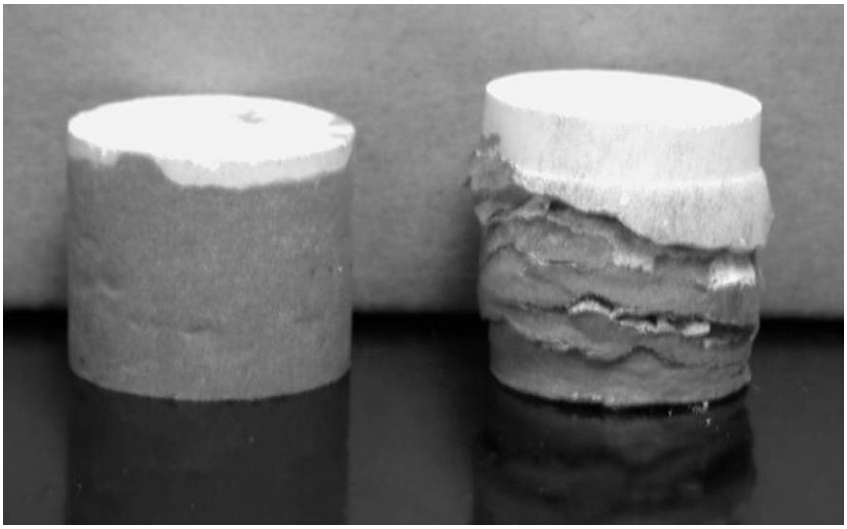

Figure 54: Cylindrical rod specimens with chaotic mixing (left) and traditional layering (right).

4.3.2 Fabrication Strategy

The lab-scale molding assembly allowed for the processing of nine hexagonal structures at once. The isolated nature of the mold cavities provided that these processed structures could be as similar or dissimilar in composition as desired. Multiple sample structures of the compositional configurations presented in Table 21 were produced using the molding assembly. All constituent powders contained

standard quantities of binder and TiO_2 where appropriate, unless otherwise stated. Constituents are listed in order of sequential layering within the mold cavity, where the abbreviations Sm., Lg., and Bi. correspond to small particle size powder, large particle size powder, and bimodal powder respectively. Samples 7, 8, and 9 present non-traditional fabrication cases. For sample number 7, the hexagonal plug was not used to level the layer between powder applications. Instead, a small mixing rod was used to gently spread powder around the cavity. This left the interface surface somewhat imperfect, although a concerted effort was made to make sure there were no gaps in the layer surface. Sample 8 was made from control powders lacking the TiO_2 sintering additive. Finally, sample number 9 was added to the mold after the vibrational processing was finished to create an unshaken control sample. This sample was then pressed and sintered with the rest of the samples as normal.

Table 21: Hexagonal specimen composition fabrication strategy.

No.	Layers	Composition (vol.% Nickel)	Notes
1	2	0(Sm.), 100(Bi.)	
2	4	0(Sm.), 0(Lg.), 100(Lg.), 100(Sm.)	
3	4	0(Lg.), 0(Sm.), 100(Sm.), 100(Lg.)	
4	4	0(Bi.), 40, 60, 100(Bi.)	
5	6	0(Bi.), 20, 40, 60, 80, 100(Bi.)	
6	8	0(Bi.), 5, 10, 20, 40, 60, 80, 100(Bi.)	
7	8	0(Bi.), 5, 10, 20, 40, 60, 80, 100(Bi.)	No leveling
8	8	0(Bi.), 5, 10, 20, 40, 60, 80, 100(Bi.)	No TiO_2
9	8	0(Bi.), 5, 10, 20, 40, 60, 80, 100(Bi.)	No shaking

4.3.3 Fabrication Results

Qualitatively reviewing the sintering specimens, the samples constructed exclusively from the pure base materials experienced the most significant warping and cracking from the sintering process. Sample 2, of identical composition to the shaken rod sample in Figure 54, completely debonded as the Nickel and Alumina

layers pulled away in opposite directions. Sample 3, which reversed the particle size ordering of sample 2, faired somewhat better but still debonded in an upward-arching manner. The sintered results of all sample structures are shown in Figure 55.

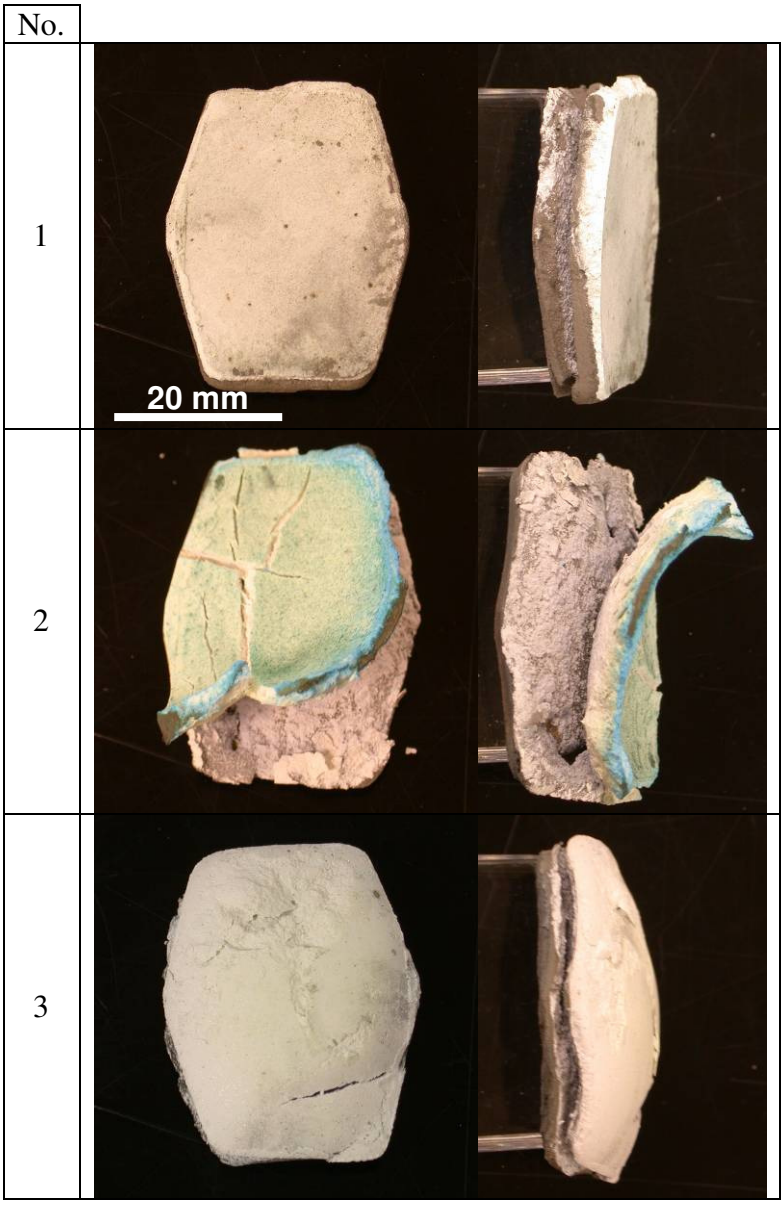

4	
5	
6	
7	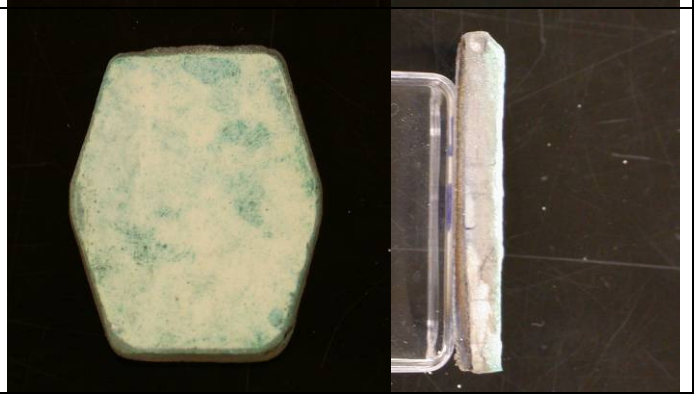

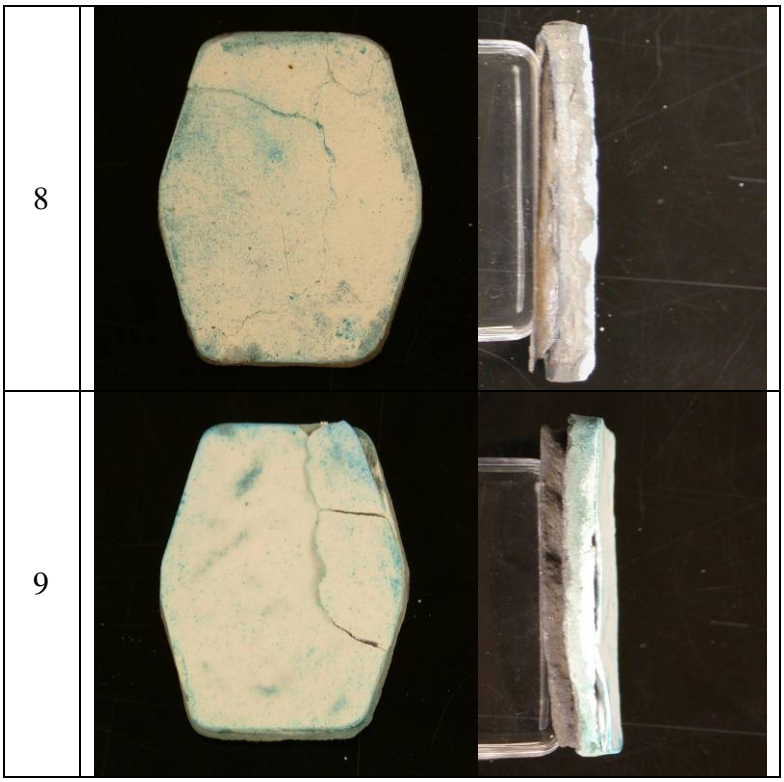

Figure 55: Top and side profile of sintered hexagonal gradient structures.

The most common failure of the composite gradient layer structures (i.e., gradient compositions other than pure), represented by samples 4-9, occurs at the 100 vol.% Nickel interface. This interface in particular seems to regularly debond from the rest of the sample. Often, this cracking and debonding only occurs on one side of the sample, while the other side remains intact. Sample 6 and sample 7 displayed the least amount of damage, where relatively minor cracking and debonding occurred on only one side of the sample. Sample 7 is used to show this one-sided crack feature of the 100 vol.% Nickel interface in Figure 56. This feature is somewhat unique to the bulk processed hexagonal structures, as cracks typically propagate around the entire outer edge or circumference of the square and cylindrical specimens respectively.

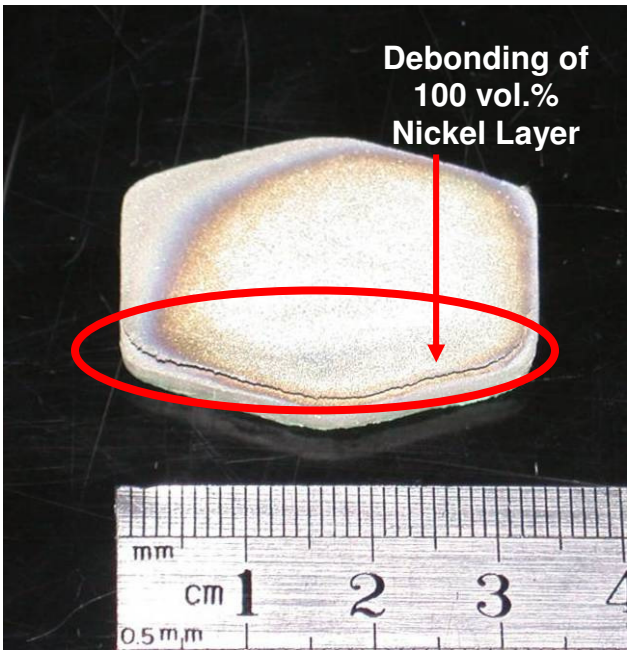

Figure 56: Debonding of the 100 vol.% Nickel layer along one side of the structure (sample 7).

Sample 7, processed without traditional interface leveling, was qualitatively the best specimen produced. Identical to sample 6 in composition, sample 7 displayed fewer cracks and the magnitude of the debonded 100 vol.% interface gap was smaller than the traditionally-layered sample 6 counterpart. Sample 8, as seen in Figure 57, presents a case where the nanopowder TiO_2 sintering aid was not applied. This sample has cracked significantly on the Alumina surface, which has not been observed in similar compositions containing the nanoparticle sintering aid. Additionally, the debonded 100 vol.% Nickel interface gap is significantly larger. From these results, it is concluded the nanopowder TiO_2 sintering aid also offers beneficial gradient densification properties when applied to the hexagonal structures.

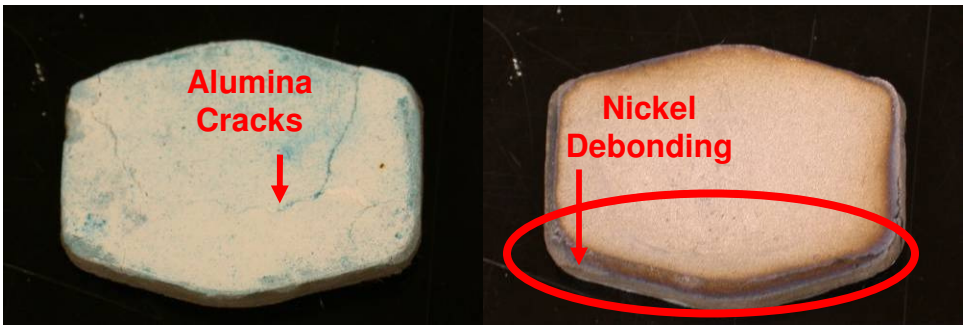

Figure 57: Hexagonal gradient structure processed without TiO_2 powder (sample 8).

The final sample case evaluates the role of vibrational processing, as seen in Figure 58. Unshaken sample 9 exhibits significant cracking in the pure Alumina, where one corner of the surface is almost completely debonded. The 100 vol.% Nickel interface is once again debonded in this sample and exhibits a significant interfacial gap. According to these results, vibrational processing does indeed seem to reduce the amount of damage present in sintered specimens.

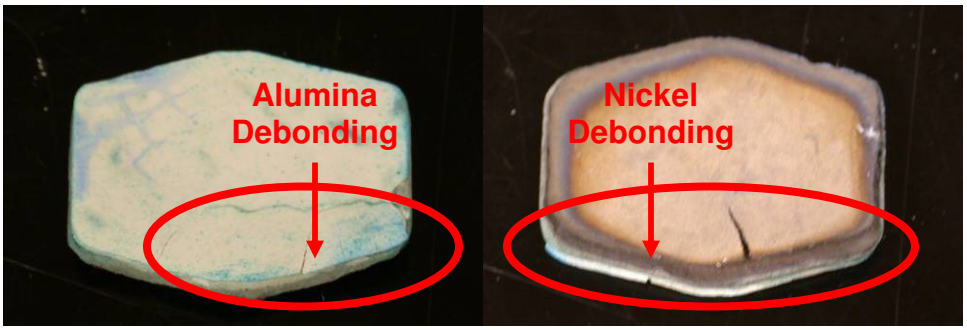

Figure 58: Hexagonal gradient structure processed without vibrational shaking (sample 9).

The final quality of the sintered structures seems to increase with the number of constituent layers. This result is evident from the qualitative evaluation of the sintered samples and is similar to the discrete layering work previously done in compaction dies. However, the role of the vibrational processing is in part to destroy the highly distinct layer interfaces that exist in traditional discrete layering operations.

Figure 59 demonstrates the difference in microstructural variation due to vibrational processing. By vibrating the mold with the slapper plate mechanism, an attempt is made at the chaotic blending of the distinct layer interfaces. As a result, residual stresses should be reduced as the discrete step-wise compositional gradient transitions to a quasi-continuous gradient. The successful creation of this quasi-continuous gradient is accomplished by either adding more constituent layers, as demonstrated by sample number 6, or by modifying the vibrational characteristics of the molding assembly. Increasing the amplitude of the slapper plate impact would shift the powders more within the mold cavity and increase blending between layers. However, significantly modifying the impaction characteristics of the molding assembly is not a viable alternative at this time. Dependent on the motion of the paint shaker, the molding assembly is somewhat limited to a fixed impact amplitude and frequency. For this reason, research has been limited to compositional changes in the bulk processed specimens rather than major molding assembly modifications (i.e., other than mold response).

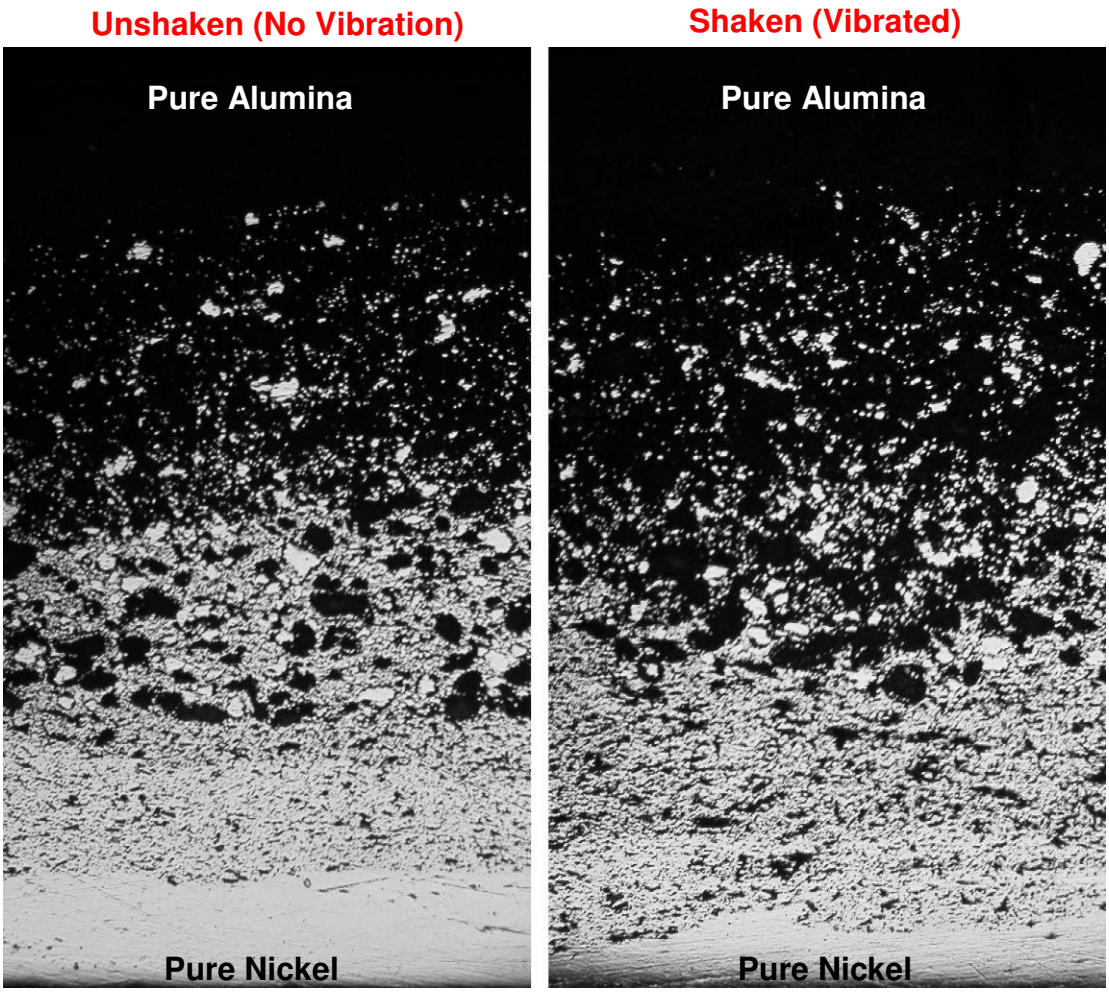

Figure 59: Cross section of (a) unshaken (sample 9) and (b) shaken (sample 6) hexagons.

4.3.4 Microstructure and Microhardness

Two eight-layer hexagonal structures were chosen to characterize with microscopy and microhardness tests. The first sample, referenced by sample number 6 in the previous section, was traditionally processed with layers consisting of 0 (bimodal), 5, 10, 20, 40, 60, 80, and 100 vol.% Nickel. The second sample, referenced by sample number 7, was of identical composition but interface layers were not deliberately leveled. To evaluate the microstructure and microhardness, significant grinding was required to plane the samples on the top surface. In

particular, sample number 7 required almost the entire top Alumina layer to be removed to reach a plane surface state. Following final polishing, six unique locations on each sample were chosen to image for microscopy analysis. The Vickers microhardness tester described previously was used to take microhardness measurements at these same six locations. The microscopy and microhardness evolution across the planed top surface of sample numbers 6 and 7 are presented in Figure 60 and Figure 61 respectively.

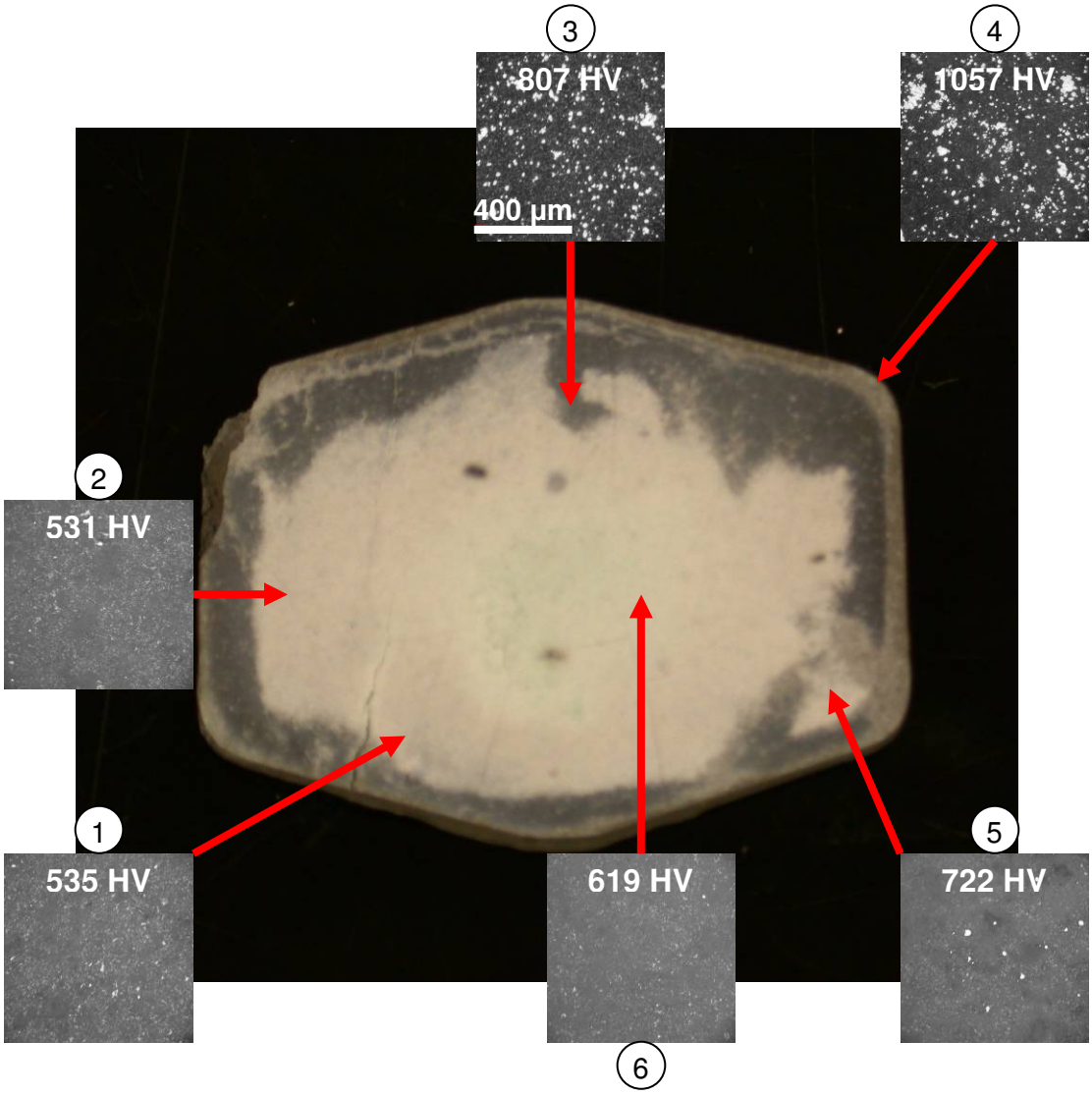

Figure 60: Microstructure and microhardness distribution for conventional eight-layer hexagonal structure (sample 6).

When related to the corresponding microstructure images, the measured microhardness tends to agree with characterization work previously done in Chapter 2. As seen by sample 6 in Figure 60, the pure Alumina tends to exhibit lower microhardness than microstructural compositions with a low volume percent reinforcing Nickel phase. For example, locations 3 and 4 appear similar to microscopy images of homogeneous 5 and 10 vol.% Nickel samples in Figure 16.

Additionally, the microstructure of image location 5 appears to demonstrate a very low Nickel composition, possibly between 0 and 5 vol.%. These image locations demonstrate higher microhardness than image locations 1, 2, and 6, which appear to be pure Alumina. The microhardness measurements tend to agree with these assessments of image location microstructure. Table 22 compares previous measurements from Table 8 and Table 12 to measurements taken from hexagonal sample 6.

Table 22: Average Vickers microhardness (HV) compared to test locations on sample 6.

Layer (vol.% Ni)	TiO_2 Disk	TiO_2 Square	TiO_2 Rod	Sample 6 Image Location (Microhardness)
0 (Bimodal)	902	680	582	2 (531), 1 (535), 6 (619)
5	806	982	936	5 (722), 3 (807), 4 (1057)
10	759	876	823	

The mixing effect introduced by vibrational processing causes varying residual stresses to develop across the sample as traditional interfaces are dissolved by interfacial blending. Microhardness is decreased from its homogeneous equivalent sample in the pure Alumina layer and increased in others, particularly the locations with approximately 5 vol.% Nickel content. The relative high in microhardness at image location 4 and relative lows of locations 1 and 2 are evidence of this effect.

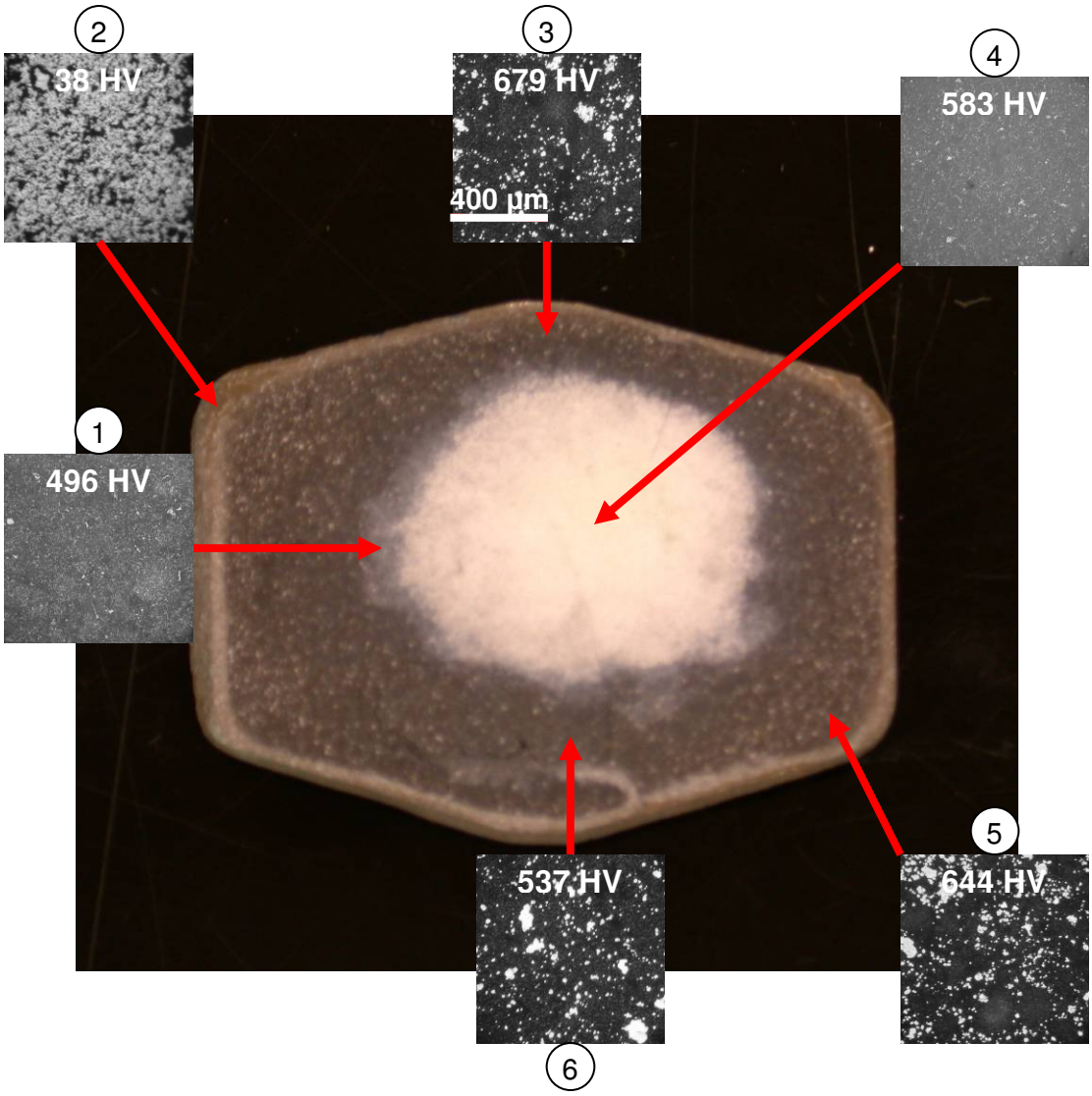

Figure 61: Microstructure and microhardness distribution for non-leveled eight-layer hexagonal structure (sample 7).

Sample 7, which was produced without interface leveling during fabrication, exhibits even more interfacial mixing. This sample also required significant grinding to reach a plane state across the top surface. As a result, Figure 61 is an image of a plane much deeper within the sample than Figure 60. Microhardness values tend to be lower in sample 7 to every equivalent location in sample 6. This trend of lower microhardness values is thought to be due to the variation in hardness by depth within

the sample. From these results, it is theorized that hardness will drop as distance is traveled within the sample. Unique to sample 7 is the existence of a high level of Nickel content around the edge of the specimen, evident in location 2. The microstructure of this location is similar to 80 vol.% Nickel in Figure 16. Locations 3, 5, and 6 exhibit microstructure between 5 and 10 vol.% Nickel and continue to tend to be of higher microhardness than the pure Alumina seen in locations 1 and 4. Table 23 compares previous measurements from Table 8 and Table 12 to measurements taken from hexagonal sample 7.

Table 23: Average Vickers microhardness (HV) compared to test locations on sample 7.

Layer (vol.% Ni)	TiO2 Disk	TiO2 Square	TiO2 Rod	Sample 7 Image Location (Microhardness)
0 (Bimodal)	902	680	582	1 (496), 4 (583)
5	806	982	936	6 (537), 5 (644), 3 (679)
10	759	876	823	
80	86	146	91	2 (38)

CHAPTER 5: Conclusions and Future Work

The research presented in this thesis focused on the development of powder processing techniques and bulk molding technology to facilitate the pressureless sintering of metal-ceramic gradient structures in commercially-viable quantities. A new nanoparticle sintering aid was introduced to Nickel-Alumina composites to control the evolution of shrinkage strain and mechanical properties during fabrication in a pressureless sintering consolidation process. Homogeneous composites were characterized for changes in microstructure, porosity, and microhardness. Previously developed porosity and sintering models were then used to characterize the evolution of shrinkage strains. To determine the effects of the nanoparticle sintering aid on shrinkage-induced stresses in gradient structures, the evolution of shrinkage strain and mechanical properties were used in a recently developed two-dimensional microthermomechanical finite element analysis. This FEA model enabled the prediction of crack-free gradient architectures, leading to the fabrication of a crack-free cylindrical rod sample using the nanoparticle sintering aid. Finally, a bulk molding technology was used to develop a prototype processing assembly for the fabrication of graded modular hexagonal specimens. The processing assembly was instrumented with strain gages to investigate the dynamic response and characteristics of the mold under different processing conditions.

5.1 Contributions

This research ultimately advances the understanding of the processing of pressureless sintered graded metal-ceramic composites. The main scientific and technical contributions of this research are as follows:

1. For the first time, a nanoparticle sintering aid has been applied to a wide range of pressureless sintered metal-ceramic homogeneous composites and metal-ceramic gradient structures. The resulting evolution in shrinkage strain and mechanical properties has been characterized and modeled.

2. For the first time, a two-dimensional finite element analysis has been developed to predict a gradient architecture for the successful experimental fabrication of a crack-free pressureless sintered Nickel-Alumina cylindrical rod specimen with a nanoparticle sintering aid. The use of the nanoparticle sintering aid has proven critical to the success of the predicted architecture.

3. For the first time, concrete molding technology has been adapted for the bulk processing of graded metal-ceramic composites in geometrically complex structures. The dynamic response of the mold has been characterized under various bulk processing conditions. Additionally, the effects of a nanofiber-reinforced polymer mold insert on mold response have also been characterized.

4. For the first time, the bulk processing of graded metal-ceramic composites in geometrically-complex structures has been investigated. Using bulk molding technology from the concrete molding industry and powder processing techniques, a laboratory-scale processing assembly has been developed for the bulk processing of graded hexagonal plate specimens.

5.1.1 Application of a Nanoparticle Sintering Aid

Anatase nanopowder TiO_2 was investigated as a sintering aid in Nickel-Alumina composites. Using a powder blending method via ball-mixing, 3 wt.% TiO_2 was added to pure Alumina. This Alumina-TiO_2 powder was then added to varying amounts of Nickel powder to form distinct Nickel-Alumina composite compositions. Nickel and Alumina particle sizes were adjusted to maintain a discrete particle reinforced microstructure within all compositions. Binder was added to the composite powders based on a thermal-behavior matching process. These composite powders were used in three applications: (1) homogeneous composite disks to characterize composite sintering behavior and material properties, (2) discrete layered

gradient structures using compaction dies, and (3) vibrated hexagonal gradient structures processed using a bulk molding assembly.

Stress-free homogenous composite disks were pressureless sintered to characterize resultant material properties. Comparing samples with and without the TiO_2 sintering aid, microstructural images of polished samples revealed little to no change in composite microstructure. Next, the initial and final porosity of each disk was calculated using geometry and mass measurements based on a ROM theoretical density formulation. Including 3 wt.% TiO_2 in the Alumina had little effect on the initial green density but significantly reduced the final sintered porosity in every composite composition. From the results, it is clear nanopowder TiO_2 can be used to increase the densification over a wide range of metal-ceramic composite volume fractions in the pressureless sintering process. Vickers microhardness tests on the same homogeneous composite disk samples found that the increased densification also resulted in increased microhardness. As with the densification, significant gains were measured in all appropriate powder compositions due to the TiO_2 sintering aid. To fully understand the relationship between porosity and microhardness, a power law function was fit to the microhardness data. From this fit, the theoretical microhardness for the fully dense matrix phase could be found. The results for the composites with the TiO_2 sintering aid indicate a lower microhardness for fully dense pure Alumina than the non-TiO_2 composites. This is attributed to the fact that at full densification, the TiO_2 acts as an impurity that actually reduces strength and hardness. However, for pressureless sintering the Alumina composites do not approach full

densification and the TiO_2 sintering aid provides significant densification and hardness benefits at attainable densities.

Discrete layering was used to fabricate die-based graded rod and square specimens with the nanoparticle sintering aid. Vickers microhardness was used to characterize the evolution of microhardness within the gradient. By comparing measurements along the gradient to the measurements previously made on stress-free homogeneous samples, a preliminary evaluation of the evolution of residual sintering stresses was determined. Related to the sintered porosity, tensile stresses that evolve in the sample will typically lower hardness and compressive stresses will typically raise hardness. Since the TiO_2 sintering aid significantly improves densification and reduces porosity, microhardness measurements recorded from samples containing TiO_2 are much higher than the non-TiO_2 counterpart samples. However, of note is the fact that samples of similar geometry tend to follow the same trends in microhardness profile shape, regardless of TiO_2 content or not. Similarly, cracked and crack-free rods containing TiO_2 displayed almost identical profile trends.

The role of the nanoparticle sintering aid on sintering behavior has been characterized using previously developed porosity and sintering models for pressureless sintered Nickel-Alumina composites. Sintering experiments were required to sinter batches of homogeneous disks at progressive sintering temperatures. The resulting shrinkage data was used to fit a Kolmogorov-Johnson-Mehl-Avrami (KJMA) sintering model. For the Alumina-rich regions, the TiO_2 sintering aid has increased the sintering rate. Conversely, a retardation effect in the

sintering rate of the Nickel-rich regions is observed due to TiO_2. This convergence of the sintering rates is the basis for developing a thermal-behavior matching process.

The nanoparticle sintering aid was also applied to bulk processed hexagonal specimens. Qualitatively, processed specimens with the TiO_2 sintering aid produced better results than specimens without the TiO_2 sintering aid. The non-TiO_2 specimens exhibited significant cracking in the pure Alumina layer, which was not observed on similar composition samples that contained TiO_2. The non-TiO_2 specimen also exhibited a larger gap at the debonded 100 vol.% Nickel interface than most other processed samples.

5.1.2 Prediction and Fabrication of Crack-Free Gradient Architectures

Using the KJMA shrinkage curves, a recently developed two-dimensional finite element analysis based on a micromechanical thermal elastic-viscoplastic constitutive model has been modified to predict the stress evolution due to differential shrinkage in metal-ceramic composites containing the TiO_2 sintering aid. The model has successfully predicted a crack-free cylindrical rod gradient architecture that was verified experimentally using powders with the TiO_2 sintering aid. In particular, the predicted gradient architecture was only successful when the nanoparticle sintering aid was used, which was verified by the cracking of identical samples made with powders lacking the sintering aid. The model, modified by this research to include the effects of the TiO_2 sintering aid, can now be used to predict other crack-free gradient architectures. These architectures can be designed to optimally reduce gradient thickness, effectively reducing structure thickness and weight. Ultimately,

gradients can be minimized and tailored to the bulk processing of geometrically-complex shapes.

5.1.3 Bulk Molding Technology and Mold Response

Trends in the concrete molding industry have inspired the investigation of bulk molding technology for graded metal-ceramic composites. A scale steel mold was machined for the experimental bulk processing of hexagonal graded structures. A processing assembly was constructed to fit this mold. To simulate the vibration platform used by the concrete molding industry, a portable paint shaker was modified to provide the vibratory motion required.

The performance of the steel mold for bulk processing was characterized for dynamic response during various processing conditions. First, the free vibration response to a single impact was found to be strongly dependent on whether the mold was secured to the frame or not. The response was found to die out very quickly when clamped to the support structure. Second, when the mold is preloaded under spring compression of the vibrator, there is a very strong signal at the frequency of the vibrator of 20 Hz. Third, when a gap exists between the slapper plate and bottom of the mold, the signal decreases as the gap increases. To study the effects of an advanced dampening material, 15 wt.% carbon nanofiber-reinforced epoxy was added to the internal cavities of the mold. The nanocomposite reduced the frequency response of the mold from 133 Hz to 113 Hz. Response could be further tailored by changing the wt.% loading of the nanofiber. Finally, the mold response was studied with the mold cavities filled with powdered material. The presence of material in the

cavities severely dampens the response and the strong signal above 100 Hz observed in previous tests was eliminated.

5.1.4 Bulk Processing of Geometrically-Complex Graded Structures

Using bulk molding technology from the concrete molding industry, powder processing techniques with a nanoparticle sintering aid, and pressureless sintering, graded hexagonal plate specimens were bulk fabricated at the laboratory-scale. The graded hexagonal specimens were prepared in the mold cavities by modifying the discrete layering technique. These samples were vibrated and shaken within the mold cavities for approximately one minute. From this point, fabrication procedure was identical to the die-based approach. A wide range of sample compositions were processed and evaluated qualitatively following sintering. While cracking was not eliminated, two eight-layer samples were produced that displayed promising results. These samples were further characterized by examining the microstructure and microhardness. The hexagonal samples, fabricated using the laboratory-scale processing assembly, are the first bulk-produced geometrically-complex graded metal-ceramic composites by pressureless sintering.

5.2 Recommendations for Future Work

5.2.1 Improved Matching of Sintering Behavior

The processing of pressureless sintered metal-ceramic composites continues to present unresolved fabrication issues. The modified thermal-behavior matching process developed by this research, using particle size distributions, binder additives, and nanoparticle sintering aids, should be further refined to better match the convergence of shrinkage curves. Indeed, the poor sintering characteristics of certain

compositions due to particle agglomerates, particularly in the 60 vol.% Nickel layer, must be improved. An attempt must also be made to better match the sintering of pure Nickel, which sinters faster and more completely than any other composition. One solution may be to introduce porosity in the pure Nickel that is not consumed during the sintering process and retards the evolution of shrinkage.

5.2.2 Performance-Mass Tradeoffs of Gradient Microstructures

For commercial and military applications of pressureless sintered metal-ceramic composites, the performance-related benefits of a nanoparticle sintering aid should be characterized. The practical applications of increased densification and hardness in the metal-ceramic composites should be investigated. For example, impact testing should be conducted on metal-ceramic plates with and without the nanoparticle sintering aid to study the propagation of resulting stress waves and damage evolution. Furthermore, the tradeoffs in tailoring the gradient microstructure to meet specific performance objectives, such as energy-absorption in an armor application, while minimizing mass should be determined through use of the experimentally-verified microthermomechanical FEA model.

5.2.3 Refinement of Microthermomechanical FEA Model for Bulk Processing of Geometrically-Complex Graded Structures

To further develop the scientific foundation for the bulk processing of pressureless sintered metal-ceramic composites, the microthermomechanical FEA model should be refined to identify crack-free gradients for geometrically-complex molded structures. With these refinements, the modeling efforts should be able to identify an optimal gradient thickness which minimizes material waste as well as structural weight and thickness. The role of vibrational processing on the blending of

discrete layer boundaries should be further characterized and subsequently modeled in order to predict the evolution of gradient microstructures and associated material properties.

References

[1] M. Pines, "Pressureless Sintering of Powder Processed Functionally Graded Metal-Ceramic Plates", *M.S. Thesis*, Department of Mechanical Engineering, University of Maryland, College Park, MD (2004).

[2] A.J. Markworth, K.S. Ramesh, W.P. Parks Jr., "Review: Modeling studies applied to functionally graded materials", *Journal of Materials Science*, 30, 2183-2193 (1995).

[3] S. Amada, T. Munekata, Y. Nagase, Y. Ichikawa, A. Kirigai, and Y. Zhifei, "The Mechanical Structures of Bamboos in Viewpoint of Functionally Gradient and Composite Materials", *Journal of Composite Materials*, Vol. 30, 800-819 (1996).

[4] B.H. Rabin, R.L. Williamson, and S. Suresh, "Fundamentals of Residual Stresses in Joints Between Dissimilar Materials", *MRS Bulletin*, 20, 37-39 (1995).

[5] A. Mortensen and S. Suresh, "Functionally graded metals and metal-ceramic composites: Part 1 Processing", *International Materials Reviews*, Vol 40 No. 6, 239-265 (1995).

[6] S. Suresh and A. Mortensen, "Functionally graded metals and metal-ceramic composites: Part 2 Thermomechanical behaviour", *International Materials Reviews*, Vol. 42 No. 3, 85-116 (1997).

[7] C.L. Hsieh and W.H. Tuan, "Elastic properties of ceramic-metal particulate composites", *Materials Science and Engineering*, A393, 133-139 (2005).

[8] E.S.C. Chin, "Army focused research team on functionally graded armor composites", *Materials Science and Engineering*, A259, 155-161 (1999).

[9] H.A. Bruck, "A one-dimensional model for designing functionally graded materials to manage stress waves", *International Journal of Solids and Structures*, 37, 6383-6395 (2000).

[10] R.N. Katz, L.A. Bracamonte, J.C. Withers, and S. Chaudhury, "Hybrid Ceramic Matrix/Metal Matrix Composite Gun Barrels", *Materials and Manufacturing Processes*, 21, 579-583 (2006).

[11] K. Tohgo and T. Kawaguchi, "Influence of Material Composition on Mechanical Properties and Fracture Behavior of Ceramic-Metal Composites", *Key Engineering Materials*, Vols. 297-300, 1516-1521 (2005).

[12] H.A. Bruck and B.H. Rabin, “Evaluating microstructural and damage effects in rule-of-mixtures predictions of the mechanical properties of Ni-Al2O3 composites”, *Journal of Materials Science*, 34, 2241-2251 (1999).

[13] B.H. Rabin and R.L. Williamson, “Design and Fabrication of Ceramic-Metal Gradient Materials”, *Processing and Fabrication of Advanced Materials III, Materials Week ’93*, Pittsburgh, PA (1993).

[14] R. Watanabe, “Powder Processing of Functionally Gradient Materials”, *MRS Bulletin*, 20, 32-34 (1995).

[15] J.T. Drake, R.L. Williamson, and B.H. Rabin, “Finite element analysis of thermal residual stresses at graded ceramic-metal interfaces. Part II. Interface optimization for residual stress reduction”, *Journal of Applied Physics*, 74, 1321-1326 (1993).

[16] R.M. German, *Sintering Theory and Practice*, John Wiley & Sons, New York (1996).

[17] C.Z. Han, I.W.M. Brown, and D.L. Zhang, “Effect of Powder Characteristics on Microstructural Development in Bodies Produced by Pressureless Sintering of Al/TiO2 Composite Powder”, *Materials Science Forum*, 437-438, 173-176 (2003).

[18] A.N. Winter, B.A. Corff, I.E. Reimanis, and B.H. Rabin, “Fabrication of Graded Nickel-Alumina Composites with a Thermal-Behavior-Matching Process”, *Journal of the American Ceramic Society*, Vol. 83 No. 9, 2147-2154 (2000).

[19] S.M. Olhero and J.M.F. Ferreira, “Effect of Different Oxide Additives on Colloidal Processing and Sintering of Alumina”, *Materials Science Forum*, 455-456, 216-220 (2004).

[20] H. Erkalfa, Z. Misirli, and T. Baykara, “Densification of Alumina at 1250C with MnO2 and TiO2 Additives”, *Ceramics International*, 21, 345-348 (1995).

[21] L.K. Zang, Y.F. Chen, Z.J. Wu, J.H. Gong, and Y.S. Xie, “Pressureless Sintering of Nickel-Alumina Composite Ceramics”, *High Performance Ceramics*, 321-324 (2001).

[22] W. Acchar and J.L. Fonseca, “Sintering behavior of alumina reinforced with (Ti,W)carbides”, *Materials Science and Engineering*, A371, 382-387 (2004).

[23] B.H. Rabin and R.J. Heaps, “Powder Processing of Ni-Al2O3 FGM”, *Ceramic Transactions*, 34, 173-180 (1993).

[24] M.L. Pines and H.A. Bruck, “Pressureless sintering of particle-reinforced metal-ceramic composites for functionally graded materials: Part I. Porosity reduction models”, *Acta Materialia*, 54, 1457-1465 (2006).

[25] M.L. Pines and H.A. Bruck, “Pressureless sintering of particle-reinforced metal-ceramic composites for functionally graded materials: Part II. Sintering model”, *Acta Materialia*, 54, 1467-1474 (2006).

[26] H.A. Bruck and A.L. Gershon, “Three-dimensional effects near the interface in a functionally graded Ni-Al2O3 plate specimen”, *International Journal of Solids and Structures*, 39, 547-557 (2002).

[27] J.R. Cho and D.Y. Ha, “Volume fraction optimization for minimizing thermal stress in Ni-Al2O3 functionally graded materials”, *Materials Science and Engineering,* A334, 147-155 (2002).

[28] Y.M. Shabana, H.A. Bruck, M.L. Pines, J.G. Kruft, “Modeling the evolution of stress due to differential shrinkage in powder-processed functionally graded metal-ceramic composites during pressureless sintering”, *International Journal of Solids and Structures*, 43, 7852-7868 (2006).

[29] M. Gasik and B. Zhang, “A constitutive model and FE simulation for the sintering process of powder compacts”, *Computational Materials Science*, 18, 93-101 (2000).

[30] B. Zhang and M. Gasik, “Stress evolution in graded materials during densification by sintering processes”, *Computational Materials Science*, 25, 264-271 (2002).

[31] K. Shinagawa, “Internal stress diagrams of sintering stress versus viscosity for graded multilayers”, *JSME International Journal Series A*, 46, 378-383 (2003).

[32] Y.M. Shabana and N. Noda, “Thermo-elasto-plastic stresses in functionally graded materials subjected to thermal loading taking residual stresses of the fabrication process into consideration”, *Composites Part B*, 32, 111-121 (2001).

[33] H.A. Bruck, Y.M. Shabana, B. Xu, and J.P. Laskis, “Evolution of elastic mechanical properties during pressureless sintering of powder-processed metals and ceramics”, submitted to *Journal of Materials Science* (2006).

[34] A. Attar, A. Bendada, R. Connolly, Y. Denomme, E. Dallaire, and P.C. Aitcin, “Novel Ultra-High-Performance Concrete as Mold Material for the Blow Molding Process”, *SAMPE Journal*, Vol. 36, No. 3, 45-49 (2000).

[35] J.G.G. Sousa, E. Bauer, R.M. Sposto, “Recycled construction debris as an aggregates. Production of concrete blocks”, *Materiales de Construccion*, Vol. 53, 59-70 (2003).

[36] Rampf Formen GmbH, “Decorative paver d_0019”, *d_19gr.jpg*, (2007). <http://www.rampf.com/site/index_1_e.htm>

[37] A. Kota, B.H. Cipriano, M. Duesterberg, D. Powell, D.I. Bigio, S.R. Raghavan, and H.A. Bruck, "Electrical and Rheological Approaches to Characterize Percolation in Polystyrene/Multi-Walled Carbon Nanotube (MWCNT) Composites", submitted to *Macromolecules* (2006).